RICE UNIVERSITY

Strain-Sensing Smart Skin for Structural Health Monitoring

by

Peng "Patrick" Sun

A Thesis Submitted
in Partial Fulfillment of the
Requirements for the Degree

Doctor of Philosophy

Approved, Thesis Committee:

Satish Nagarajaiah, Chair
Professor of Civil and Environmental Engineering and Mechanical Engineering and Materials Science and NanoEngineering

R. Bruce Weisman
Professor of Chemistry and Materials Science and NanoEngineering

Rouzbeh Shahsavari
Assistant Professor of Civil and Environmental Engineering and Materials Science and NanoEngineering

Houston, Texas

April, 2017

ABSTRACT

Strain-Sensing Smart Skin for Structural Health Monitoring

by

Peng "Patrick" Sun

Over years, many structural health monitoring (SHM) strategies and damage detection techniques/methods have been proposed. Traditional strain sensing, such as resistance strain gages, can only monitor strain at discrete locations and along specific directions, and have limited ability to measure strains on small length scales. Some emerging full-filed non-contact strain sensing techniques, such as interferometric techniques, non-interferometric techniques and Raman spectroscopy techniques, have many other limitations. A new strain sensing technique is needed to perform fast SHM on structures. In this thesis, three generations of a novel non-contact strain measurement technology, strain-sensing smart skin (S^4), are developed using the characteristic short-wave infrared (SWIR) fluorescence signatures of semiconducting SWCNTs and the systematic shifts of their fluorescence peaks when the nanotubes are axially strained. In practice, the S^4 sensor is coated the structural surface with a thin polymeric film containing well dispersed SWCNTs. Strain in the substrate is transmitted through the polymer to the nanotubes, causing systematic and predictable shifts of the SWIR fluorescence peaks. A small diode laser excites a spot on the coated surface, and the resulting emission is captured and spectrally analyzed to deduce local strain along any direction of interest.

Stress fields around structural discontinuities, such as cracks, usually cause com-

plex but distinct strain contours when structures are subjected to load. Hence mechanical strain on structural surfaces can provide useful information on the condition of the material, such as the damage location and severity. The developed S^4 film sensors are used to study the strain distribution near different structural discontinuities. Metallic bars in tension have been studied in two cases: (1) with a central hole, and (2) with an edge notch. S^4 film sensors measured the residual strain contours near structural discontinuities under axial loading. Linear elastic fracture mechanics was used to compute the closed-form solution of strain fields. Finite element (FE) elasto-plastic nonlinear models were constructed and validated by using strain gage data from the experiments. The FE analysis results are found to match the strain distribution obtained from S^4 measurements. S^4 technology can be widely applied in the realms of non-destructive evaluation, experimental mechanics, and SHM.

Acknowledgments

I owe forever my sincerest gratitude to my advisor, Professor Satish Nagarajaiah, for his guidance in research and his belief in my potential, for the continuous support of my Ph.D study and research, for his patience, motivation, and immense knowledge. His guidance helped me all the time in research and writing of this thesis. I could not have imagined having a better advisor and mentor for my Ph.D. study.

I would also give many thanks Professor R. Bruce Weisman for his insightful ideas and his patience and support in overcoming the numerous obstacles that I have been facing through my research, but also for his demonstration and encouragement for becoming a better and respectable researcher.

I thank Prof. Rouzbeh Shahsavari, Prof. Jun Lou and Prof. Ilinca Stanciulescu for their courses and their insightful comments and encouragement on the research.

My sincere thanks also goes to Dr. Sergei Bachilo and Mr. Ching-Wei Lin who provided me the technical support for building the automation system for strain sensing. Without their precious support it would not be possible to finish this research.

I thank my fellow mates from Prof. Nagarajaiah's group and Prof. Weisman's group for the stimulating discussions, for days and nights we were working together, and for all the fun we have had in the last five years.

I thank all my friends that gave me support in the past five years. Being with friends is my most valuable experience of my life.

Last but not the least, I would like to thank my parents Mr. Jianhua Sun and Ms. Fenglei Dai, my wife Judy Song and my parents-in-law Mr. Jack Song and Ms. Ann Lee for supporting me financially and spiritually throughout my Ph.D. study.

Contents

Illustrations

Tables

Chapter 1

Introduction

1.1 Current State of Structural Health Monitoring

Structures, such as bridges, buildings, oil platforms, pipelines, aircraft and so on, ensure society's economic prosperity. In service and daily use, structures are often subjected to harsh loading scenarios and severe environmental conditions, which cause long-term structural deterioration [4]. Hence, there is a need to monitor the health conditions of those structures while they are still in service to ensure public safety.

Structural health monitoring (SHM) is a paradigm that offers an automated method for tracking the health of a structure by combining damage detection algorithms with structural monitoring systems. [4] Damage detection methods can provide efficient tools to analyze and diagnose structural responses (measured data) for patterns of structural damage. Over the past twenty years, many structural health monitoring strategies and damage detection techniques/methods have been proposed, as reviewed in literature by Doebling et al. [5], Sohn et al. [6] and Diamanti et al. [7].

The process of damage detection, as known as SHM, for aerospace, civil and mechanical engineering infrastructure/structures is also regarded as one of statistical pattern recognition [6]. This paradigm consists of four parts: (1) operational evaluation, (2) data acquisition, fusion and cleansing, (3) feature extraction and information condensation and (4) statistical model development for feature discrimination. [6]

In the operational evaluation part within SHM aforementioned, many non-destructive

evaluation (NDE) techniques have been proposed and researched, including: visual inspection; optical methods (photoelasticity, holography and Moire methods); eddy-current (electro-magnetic testing); ultrasonic inspection; laser ultrasonics; acoustic emission; vibration analysis; radiography; thermography and Lamb waves. [7] Although many techniques have been developed for NDE, these damage detection methods can generally be classified as one of two types: local or global NDE. [4] Unlike global damage detection methods, local-based damage detection methods attempt to identify damage based on screening structures at their component or subcomponent length-scales. Local NDE is suitable to detect the structural damage phenomena (e.g. cracks, corrosion), while global damage detection was initially proposed to monitor a whole structure by collecting structural response time histories (e.g. structural vibrations including acceleration, displacement, dynamic strain) at many different locations.

1.2 Existing Strain Sensing Technologies for Structural Health Monitoring

Among the variety of sensing transducers used for structural health monitoring (SHM), strain sensors rank among the most important for determining long-term structural resilience and health [8]. Researchers widely employ strain sensors to measure mechanical strain in both laboratory and field environments, because the strain measured on the surface of any structure, compared to other structural responses (such as acceleration and displacement), provides direct first-hand information about its condition. Hence, strain sensing provides more structural information corresponding directly to the induced localized stress/strain field, which is commonly used for

damage detection.

Traditional technologies used for measuring strain, such as resistance strain gages, can only monitor strain at discrete locations and along specific directions, and have limited ability to measure strains on small length scales [9]. Optical fiber sensors and more specifically fiber Bragg grating (FBG) sensors are also widely used in health monitoring of structures, offering strain and temperature readings [10, 11]. However, practical issues, such as deployment of the optical fiber to the structure and connectors and the high cost of the FBGs, need to be addressed.

By exploiting the dependence of the electronic properties of carbon nanotubes (CNTs) on their atomic structure, Peng et al. [12] discovered that surface strain can modulate the conductance of CNTs quantitatively and predictably. Dharp et al. [13] pioneered a nanotube-based film sensor to measure strain-induced changes in electrical transport properties. For many years, piezoelectric strain sensors have been successfully used as vibration sensors in smart structures, providing the benefits of simple interface circuitry and high sensitivity [14]. Recently, MEMS double-ended tuning fork (DETF) strain gauges [15] have been investigated as sensors, based on the dependence of their resonant frequency on strain. In 2007, Loh et al. [8] used carbon nanotube and polyelectrolyte composite to fabricate a multilayer thin film for measuring strain and corrosion processes through strain-induced resistance change. In 2014, Ryu et al. [16] designed photoactive thin film that could selectively sense strain or pH depending on the wavelengths of light used for sensor interrogation, by collecting and analyzing strain-sensitive photocurrent. Although these newer strain sensing approaches can achieve high spatial resolution or/and strain sensitivity, they still require electrical connections to the sensor elements in order to obtain strain readings.

Aside from the aforementioned point-wise strain gauge techniques, various full-field non-contact optical methods have also been developed. The existing non-contact optical methods can be classified into two types [17]: (1) Interferometric techniques, such as holography interferometry, speckle interferometry, Moire interferometry, and photoelasticity; (2) non-interferometric techniques, such as the grid method [18], digital image correlation (DIC) [19,20], and digital volume correlation (DVC) with X-ray micro-computed tomography [21]. The interferometric techniques have been proposed and developed over the past few decades. They identify material changes based on variations in transmission intensities, phase changes, diffraction properties, or interference fringe patterns [22]. Although they can provide full-field strain measurements without physical contact, they usually require a model of actual structure, tedious calculations to separate the values of principal stresses, and expensive equipment. The non-interferometric techniques have been extensively investigated and improved for reducing computation complexity, achieving high accuracy measurements of deformations. However, the DIC or DVC methods suffer some disadvantages, such as the requirements for a random gray intensity distribution or speckle pattern distribution, heavy dependence on the quality of the imaging system, relatively low strain measurement accuracy in small deformation measurements, and the inability to measure strains induced when the object is in service and not under direct observation by the imaging system. [17]

1.3 Nanotechnology in Existing Wireless Strain Sensing Methods

Over the past two decades, Raman spectroscopy has been used as a standard characterization tool for carbon nanostructures. Tensile or compressive stress applied to single-walled carbon nanotubes (SWCNTs) induces strains and measurably perturbs the nanotube Raman spectrum. Probing such shifts in phonon frequencies is an effective way to assess the degree of load transfer to the nanoparticle when the surrounding material is under an applied stress. In this way, Raman spectroscopy has been explored by several researchers as a method to monitor nanotube films in strain sensing applications [23–27]. Raman spectroscopy has also been used to detect the strain on graphene flakes embedded in graphene-polymer composite coatings [28]. However, the main drawback of Raman-based strain measurement approaches is the weakness of the Raman scattering signals. As a result, the acquisition times needed to achieve adequate signal-to-noise ratios are impractically long for real field applications.

1.4 Single-Walled Carbon Nanotubes and Photoluminescence

Single-walled carbon nanotubes are a family of highly elongated tubular structures composed of carbon atoms covalently bonded into specific ordered forms. Each form has a well-defined diameter and roll-up angle, and is uniquely labeled by a pair of integers, (n, m). [29] Among the remarkable properties of SWCNTs are their well-defined spectral transitions that vary systematically with physical structure [30], reflecting the quantum confinement of π-electrons perpendicular to the tube axis. As shown in Figure 1.1, most SWCNT structural species are semiconducting and show robust photoluminescence (fluorescence emission) at distinct near-IR wavelengths corresponding

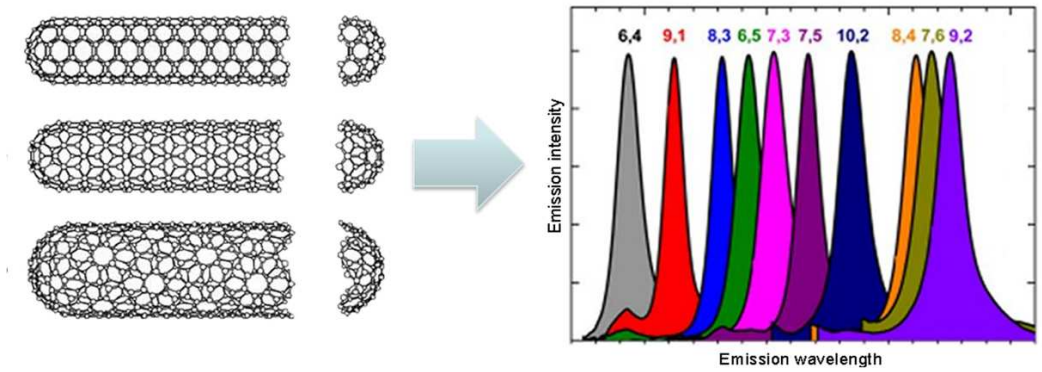

Figure 1.1 : Different nanotube species correspond to different characteristic emission peaks

to their semiconducting band gaps. [30–32]

It is known from theory and experiment that axial stretching or compression of SWCNTs causes predictable changes in electronic structure that systematically shift their spectral transitions. [1,24,32–36] Previous studies on individual nanotubes have confirmed that these shifts occur in opposite directions for "mod 1" and "mod 2" nanotubes (for which $mod(n-m,3) = 1$ *or* 2), as shown in Figure 1.2, and that the magnitudes of the spectral shifts are proportional to $\cos(3\theta)$ (where θ is the nanotube roll-up angle), as shown in Figure 1.3. These shifts in SWCNT fluorescence spectra are large enough to reveal axial strains below 0.1%, suggesting the possibility of a practical non-contact optical method to measure strains in large-scale objects using embedded SWCNTs as the sensors. This approach represents an attractive alternative to carbon nanotube-based sensors based on strain-induced changes in electrical transport properties or Raman spectra [13, 24, 27, 37, 38] because fluorescence spectroscopy requires no electrical connections and provides stronger signals and faster data acquisition than Raman.

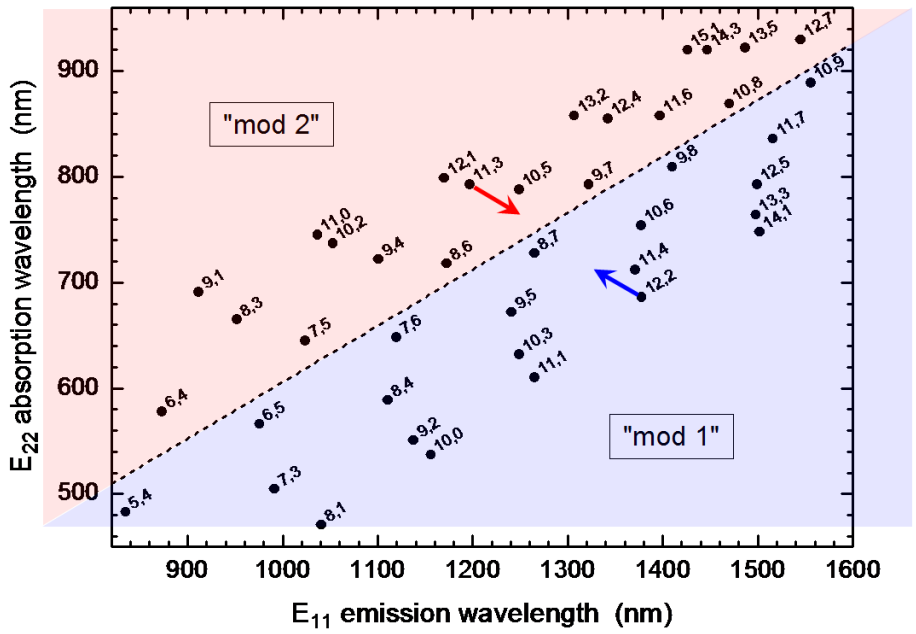

Figure 1.2 : Absorption and emission peak wavelengths for various (n, m) SWCNT structural species. Nanotubes with mod 1 character are in the blue (lower) shaded region; those with mod 2 character are in the pink (upper) shaded region. The red and blue arrows show the directions of mod-dependent shifts in spectral peak positions caused by axial stretching.

1.5 Research Objectives

This thesis mainly focuses on the development and application of a novel, non-contact, full-field strain sensing technique, which can serve as a local damage identification method for SHM and operational evaluation.

The thesis is structured as follows. An introduction of Structural Health Monitoring and Strain sensing based damage identification are described in the abstract and Chapter 1. Chapter 2 shows the fabrication of Generation-I "Strain-Sensing Smart Skin" or S^4 films and some corresponding preliminary experimental results.

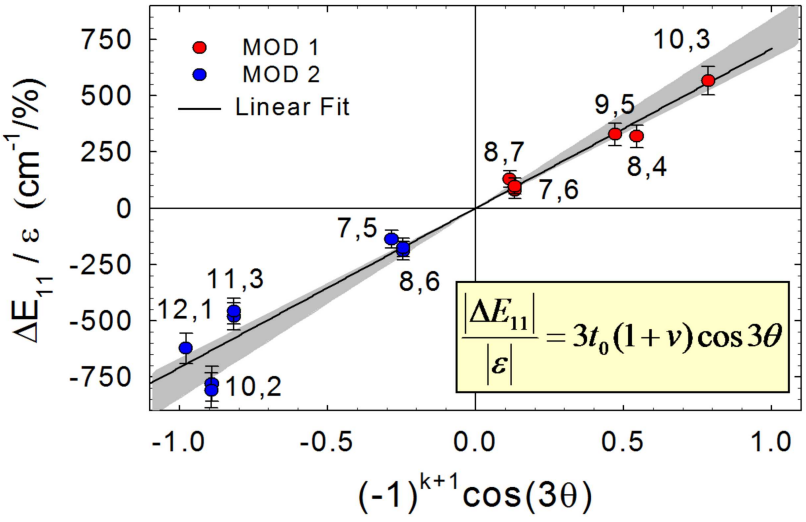

Figure 1.3 : Strain-induced spectral shifts of near-IR fluorescence peaks of different (n, m) species of SWCNTs. [1].

Chapter 3 presents the development of Generation-II S^4 films with the adoption of Poly(9,9-di-n-octylfluorenyl-2,7-diyl) (PFO) to purify Single-Walled Carbon Nanotubes (SWCNTs). Chapter 4 illustrates the efforts to enhance photoluminescence of the diluted SWCNTs within smart skin and proposes a "sandwich" film structure of newly fabricated S^4 sensors. Chapter 5 demonstrates the application of S^4 films in mapping the residual strain field around structural discontinuities. Final conclusions are summarized in Chapter 6.

Chapter 2

Design and Fabrication of Prototype S^4 Films

2.1 Introduction

As mentioned in Chapter 1, the operational safety of structural components, such as aeroplane fuselages and bridge girders, requires periodic structural health monitoring. While existing traditional contact strain sensing methods are only capable of monitoring strains at fixed positions and along fixed directions through physical connections to external readout devices. And the existing non-contact full-field strain sensing techniques have other drawbacks. For example, Raman spectra method (described in Section 1.3) provides relatively weaker signals and therefore requires longer time for data acquisition; photoelasticity method usually requires a plastic replica of actual structure or a thick plastic film (usually 2-3 mm) on structure and tedious calculations to separate the values of principal stresses; digital image correlation (DIC) method lies in the requirements for a random gray intensity distribution or speckle pattern distribution and heavy dependence on the quality of the imaging system.

A novel non-contact method for strain monitoring using the spectral properties of single-walled carbon nanotubes (SWCNTs) as mentioned in Section 1.4 will be described in detail in this chapter. In Generation-I S^4 films, SWCNTs are unobtrusively embedded in a polymeric coating applied to the substrate of interest. Strain in the substrate is transferred through the coating, deforming the embedded nanotubes and causing predictable changes in their electronic structure. These changes are measured

optically, without physical contact, as strain-induced spectral shifts of the characteristic SWCNT near-IR fluorescence peaks. Substrate strains can be quantitatively deduced at any location and along any direction by positioning the excitation laser beam and orienting its polarization plane.

In this chapter, the prototype (Generation-I) S^4 film sensor is studied for point-wise strain sensing with multiple directions. This chapter begins with a theoretical overview and a numerical simulation of a randomized SWCNTs system in polymer with perfect strain transfer from polymeric matrix to SWCNTs. This chapter later follows with a detailed description of the fabrication of the Generation-I S^4 film and the experimental setup for the Generation-I S^4 sensing device. The experimental results and discussions are presented in the end.

2.2 Numerical Model of S^4 film

2.2.1 Orientation of a Single SWCNT

Unlike the microscopic study of individual SWCNTs in a strained polymer by Weisman group at Rice University [1], each spectral measurement on the S^4 films probes an ensemble of embedded SWCNTs that have randomly oriented distributions. For example, a S^4 film containing perfectly distributed SWCNTs (both in orientational and position distribution) is uniformly stretched in one direction. A 3D Cartesian coordinate is built on the S^4 film with the z-axis is perpendicular to the surface of the film. The laser propagation is also along the z-axis and the applied strain ϵ is along the y-axis. As shown in Figure 2.1, one end of a SWCNT is at the origin of the coordinate system, the angle between the SWCNT and the z-axis is defined as θ, the angle between the projection of the SWCNT in x-y plane with the y-axis is defined

as ϕ and the angle between the laser-polarization plane intersecting the $x-y$ plane with the y-axis is defined as α.

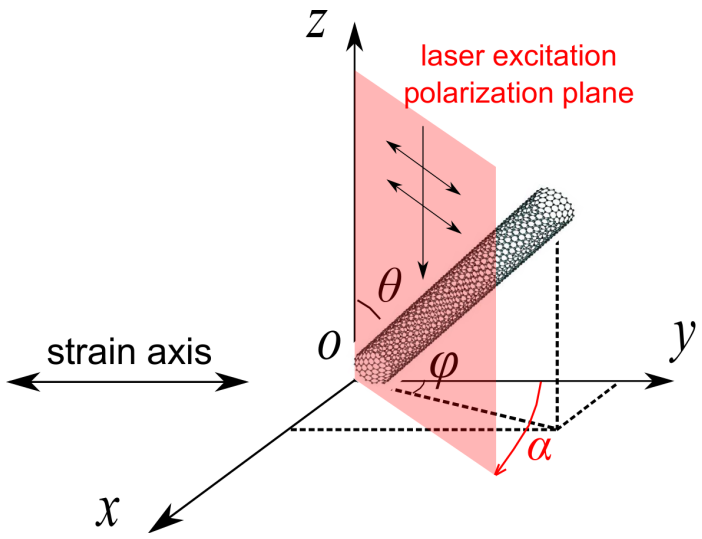

Figure 2.1 : Orientations of a single nanotube, laser-polarization and strain.

The angle between the nanotube axis and the strain axis can be calculated as $\beta = \arccos(\sin\theta\cos\phi\cos\alpha + \sin\theta\sin\phi\sin\alpha)$. The relative probability that an individual SWCNT in the film will absorb light from the laser is $\sin^2(\theta)\cos^2(\phi-\alpha)$. The emission intensity of one single SWCNT excited by a laser with its polarization direction along the SWCNT's axis is set as I_0. Theoretically the emission intensity of a SWCNT i with an arbitrary orientation excited by the same laser is obtained as follows:

$$I_{nti} = I_0 \sin^2(\theta)\cos^2(\phi-\alpha) \tag{2.1}$$

Assuming no bending or torsional deformation in SWCNTs, the only strain acting on the single SWCNT i, ϵ_{nti}, is along the SWCNT axis. With the original length of the SWCNT set as L_{nti}, the deformed length of the nanotube is L'_{nti}, calculated by Equation 2.2. The strain on the tube ϵ_{nti} can be approximated in Equation 2.3,

considering the Poisson's effect when polymeric matrix deforms due to the applied strain ϵ.

$$L'_{nti} = \sqrt{1 + 2\epsilon(\cos^2\beta - \nu\sin^2\beta) + \epsilon^2(\cos^2\beta + \nu^2\sin^2\beta)} \tag{2.2}$$

$$\epsilon_{nti} \approx \epsilon(\cos^2\beta - \nu\sin^2\beta) \tag{2.3}$$

The spectral shift of nanotube fluorescence, Δ_{nti}, due to the applied strain is a function of the angles θ, ϕ, α and the applied strain ϵ:

$$\Delta_{nti} \approx \Delta_{max}(\cos^2\beta - \nu\sin^2\beta) \tag{2.4}$$

where Δ_{max} is the shift for the single SWCNT when the strain is applied parallel to the tube axis, and ν is Poisson's ratio for the host polymer.

$$\Delta_{max} = \gamma\epsilon \tag{2.5}$$

where γ is the strain sensitivity of SWCNT (the shift in wavelength caused by unit strain along the nanotube axis).

Inserting Equation 2.5 into Equation 2.4, we can obtain

$$\Delta_{nti} \approx \gamma\epsilon(\cos^2\beta - \nu\sin^2\beta) \tag{2.6}$$

2.2.2 Randomized SWCNT Systems

We can express G_{sys} and G'_{sys} as the integrated spectrum from all the SWCNTs in the system before and after the applied strain, respectively, with

$$G_{sys} = \sum_{i=1}^{n} I_{nti} g_{nti}(\lambda_{nti}) \tag{2.7}$$

$$G'_{sys} = \sum_{i=1}^{n} I_{nti} g_{nti}(\lambda'_{nti}) \tag{2.8}$$

where λ_{nti} is the original wavelength without strain, λ'_{nti} is the shifted wavelength due to strain, n is the total number of SWCNTs in the system, $g_{nti}(\lambda)$ is the shape function of the spectrum from the SWCNT i.

In practice, the distributions in polar angle θ and in x-y plane angle ϕ are not known a priori. However, the orientational distribution of nanotubes within a polymeric film (well dispersed) may follow a combination of the two limiting random distribution patterns: 2D planar and 3D spherical uniform distribution model (shown in Figure 2.2).

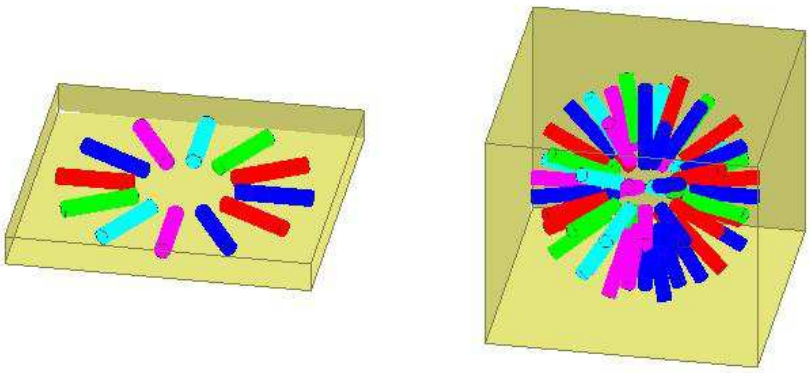

Figure 2.2 : Orientation of tubes in (left) planar and (right) spherical probabilistic models

Defining $f(\theta)$ as the probability distribution function for the orientation of single SWCNT as shown below:

$$f(\theta) = a \cdot \frac{1}{2\pi}\delta(\pi/2 - \theta) + b \cdot \frac{1}{2\pi^2} \tag{2.9}$$

where $a + b = 1$.

As shown in Figure 2.3, the measured emission spectrum from a SWCNT system containing SWCNT with different orientations is a superposition of the spectra from the SWCNTs in the system, with corresponding variations in intensities I_{nti} and strain-induced spectral shifts Δ_{nti} from λ_{nti} to λ'_{nti}.

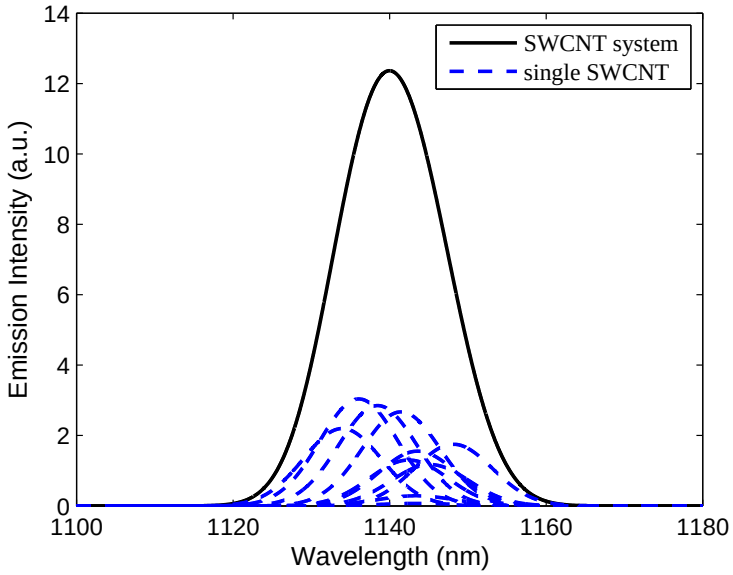

Figure 2.3 : Integrated spectrum from 10 nanotubes with 2D randomized orientation and randomized length.

The proportions of the two probabilistic models are represented by the two parameters a and b within Equation 2.9. Once the proportions of the two limiting case probabilistic models is determined, the integrated fluorescence spectrum can be computed. Further, the peak shift of the integrated spectrum can be obtained by using curve fitting algorithms.

A numerical model of randomized SWCNTs system is built to investigate the spectrum response of the SWCNTs system to the applied strain. For simplicity, one

single SWCNT species, (7,6), is chosen for the study and the properties of the SWCNTs are set to the parameters in Table 2.1. The properties of (7,6) Gaussian function is used to simulate the shape of fluorescence spectrum of each nanotube. Assume the shapes of all the spectrum emitted from (7,6) SWCNTs are the same, following Gaussian function with the same standard deviation $\sigma_{nt} = 5\ nm$ but with slightly different mean value μ_{nt} near $\lambda_{(7,6)} = 1140\ nm$. In the simulation, the expectation of the distribution μ_{nt} varies following a normal distribution with $\mu_\lambda = 1140\ nm$ and $\sigma_{wl} = 5\ nm$.

Table 2.1 : (7,6) SWCNT fluorescence features

Parameter	Detail
λ_{nti}, wavelength at peak	normal distribution: $\mu_\lambda = 1140\ nm$, $\sigma_\lambda = 5\ nm$
g_{nti}, spectrum shape of SWCNT i emission	Gaussian function: $\mu_{nti} = \lambda_{nti}$, $\sigma_{nti} = 5\ nm$,
m_{nti}, no. of segments (length)	uniform distribution: 20 - 40
I_{nti}, intensity of SWCNT i emission	m_{nti}
α, polarization-x axis	uniform distribution: $0\ -\ \pi$
θ, nanotube-z axis	uniform distribution: $0\ -\ \pi$
ϕ, nanotube projection in xy plane-x axis	uniform distribution: $0\ -2\ \pi$
$\gamma_{(7,6)}$, (7,6) strain coefficient $\frac{\partial \lambda_{(7,6)}}{\partial \epsilon}$	$1.2\ nm/m\epsilon$

The orientational distribution of nanotubes within a polymeric film (well dispersed) may follow a combination of the two distribution patterns. Theoretically, the thinner the polymer is, the closer the SWCNTs orientation would be to the planar system. The more the tubes are aligned within the plane of the substrate surface, the larger spectral peak shift the smart skin will show. Two numerical models are compared in Figure 2.4, where highly linear response is found for both cases.

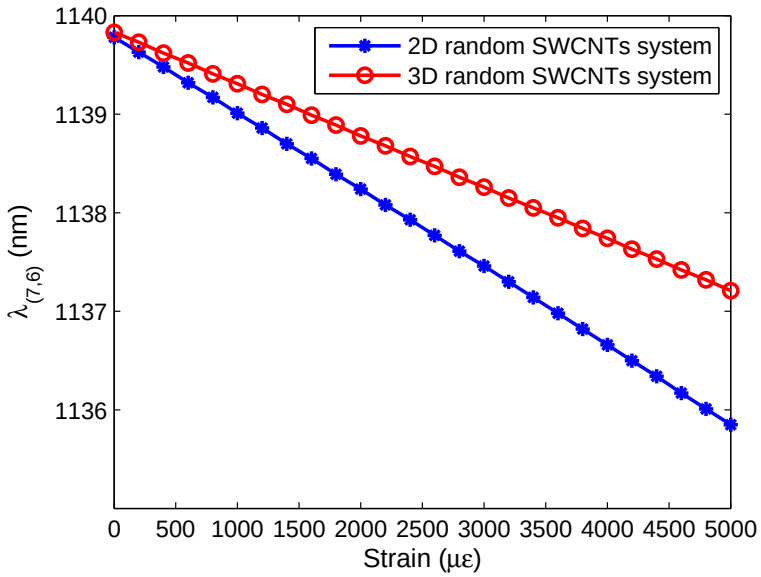

Figure 2.4 : The peak shift of 2D and 3D randomized SWCNTs system (n=2000).

2.3 Generation-I S^4 Film Fabrication

This section focuses primarily on the fabrication aspects of Generation-I smart skin based on the experience gathered in our previous experimental work [39, 40]. In order to function effectively, the nanocomposite requires adequate nanotube dispersion, effective load transfer from the substrate, to the film and to the nanotubes, strong nanotube fluorescence intensity, and resistance to environmental changes.

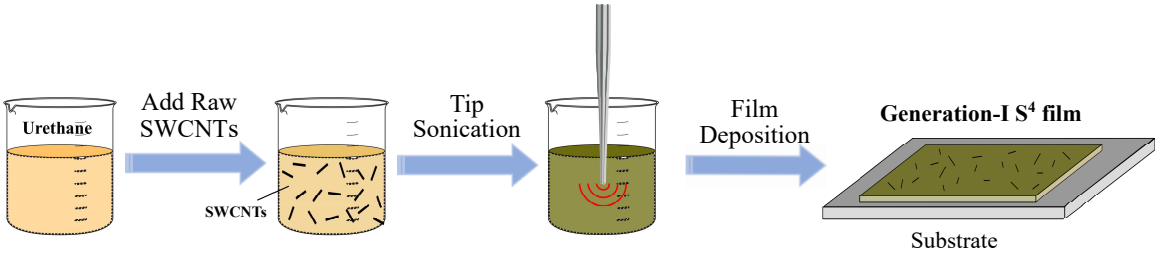

Figure 2.5 : The procedures in the fabrication of Generation-I S^4 films.

Figure 2.5 shows the procedures in the fabrication of Generation-I S^4 films. Firstly, raw SWCNTs grown in the Rice University HiPco reactor is selected for the study. These samples contain nanotubes with varied (n,m) structures are aggregated into bundles bound by van der Waals forces. Raw HiPco SWCNTs is added into a commercial exterior varnish (Minwax Helmsman Spar Urethane, 350 VOC compliant) at a weight/volume ratio of 0.5 mg : 1 mL (3 mg SWCNTs : 6 mL spar urethane). The composite is mixed by tip ultrasonication for 7.5 min (effective time) at a power of 1 W/mL (15 s on, 15 s off) and then more varnish is added to increase the volume by 50%. That mixture is then bath ultrasonicated for 10 min and tip ultrasonicated for another 1 min (effective time). The final weight/volume ratio of raw SWCNTs to urethane is 0.25 mg : 1 mL.

One should note that although longer ultrasonication leads to improved dispersion, it also causes nanotube cutting, giving a larger number of shorter nanotubes that appear to be less efficient in load transfer from the host polymer. We therefore carefully chose the duration of ultrasonication to balance nanotube dispersion and length. The SWCNT-urethane mixture is then spin-coated onto a PMMA substrate (75 mm x 25 mm x 6 mm) that has been surface-roughened using a fine sandpaper to improve adhesion and allowed to dry under ambient conditions. Spin coating/brush coating is repeated until the SWCNT fluorescence emission from the the surface coat is significantly intense, and then the sample is cured for days at room temperature prior to measurements.

2.4 Generation-I S^4 Device Setup

As shown in Figure 2.6 is the prototype strain sensing probe with a polarized laser excitation at a wavelength of 660 nm and at a power of 70 mW, through a circularized-

beam diode laser (PTI model PPM80). As shown in Figure 2.7, the laser beam is shot through a Schott KG3 filter to remove near-IR components and through a half-wave plate which enables the adjustment of the polarization plane. After the laser beam passes through the hole in the reflection mirror, it is focused onto the sample by a 30 mm focal length lens. A traditional resistive foil strain gage is affixed on top of the smart skin close to the measurement point where the interrogating laser illuminates the smart skin. The strain on the substrate is measured using another strain gage mounted at the corresponding location on the opposite surface of the slide. Readings from the two strain gages are monitored in real time to check the efficiency of strain transfer from substrate to polymer while axial strain is on the slide. Withey et al. [39] found that if the polymeric film is very thin (within 25 μm), the applied strain, as measured on the opposite surface of slide, is nearly equal to the strain measured on the surface of the polymer.

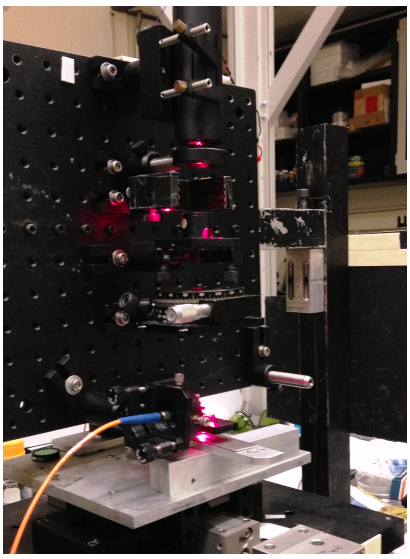

Figure 2.6 : Prototype S^4 device.

Spatial resolution in this method is equal to the size of the excitation beam pro-

jected onto the surface, which is approximately 100 μm by using this experimental setup.

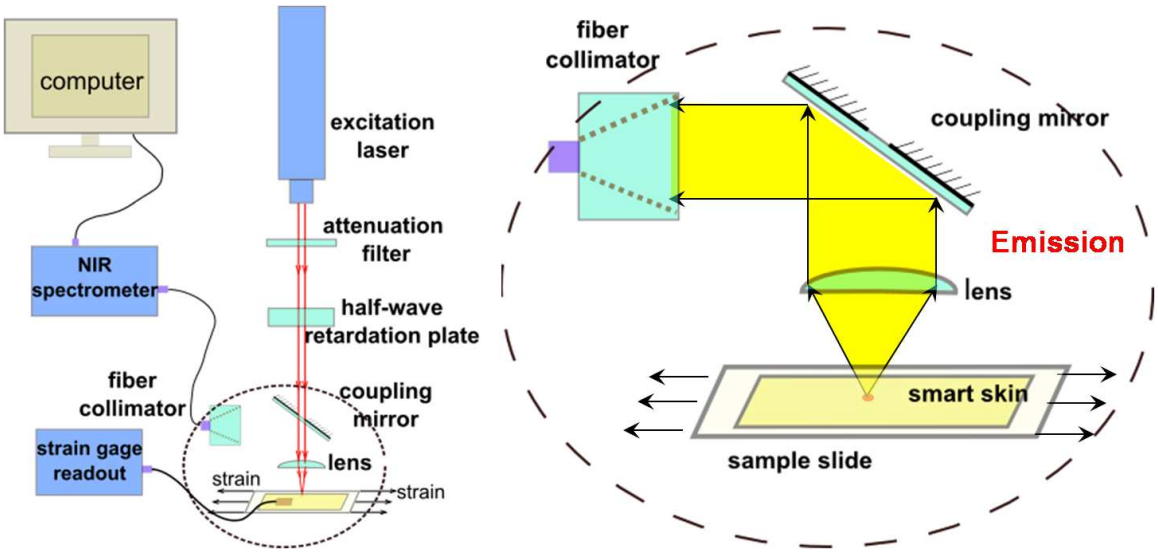

Figure 2.7 : Optical strain measurement setup.

2.5 Experiments and Results

The PMMA specimen is tested using a custom built four-point bending jig while strain is monitored by resistive foil strain gauges on the PMMA substrate bar. Strain values on the bar surface and in the polymer film are assumed to be nearly equal when the film is very thin. Strain is adjusted in steps of several hundred $\mu\varepsilon$ during loading and unloading. The experimental value of the strain sensitivity of peak separation of (7,6)-(7,5) can be calculated by using linear regression of the measured data as follows:

$$\gamma_{(7,6)-(7,5)} = \partial(\lambda_{(7,6)} - \lambda_{(7,5)})/\partial\epsilon \tag{2.10}$$

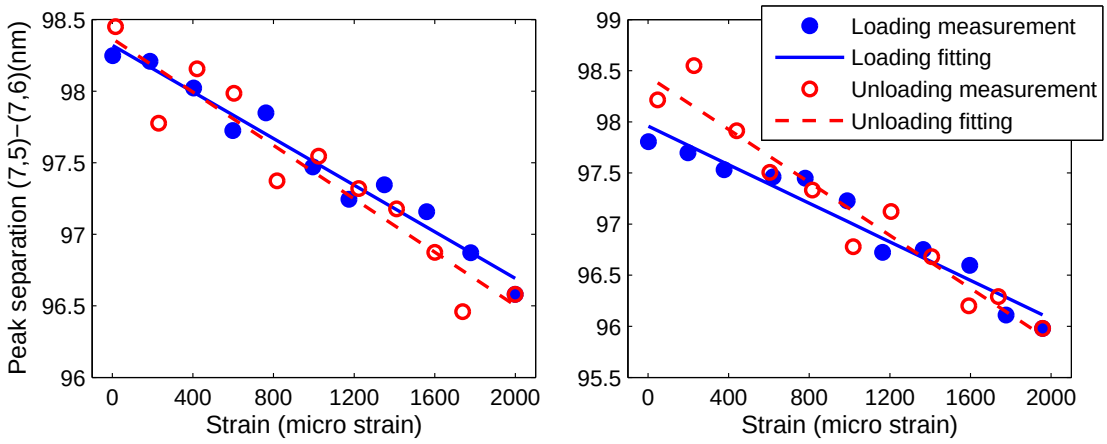

Figure 2.8 : Strain variation of differential spectral shift (left) load-unload cycle 3 (right) load-unload cycle 4. The difference in peak emission wavelengths of (7,6) and (7,5) nanotubes in a polymeric coating is plotted vs. strain in the substrate, as measured with a resistive strain gage. Blue solid circles show data measured with increasing strain; red hollowed circles are measured with decreasing strain. Straight lines show linear best fits to the data.

The S^4 film is subjected to cyclic deformation of 11 cycles with strain variation within from 0 to 2000 $\mu\epsilon$, as shown in Figure 2.8. In the load-unload cycle 3, load fitting $\gamma_{(7,6)-(7,5)} = 0.8\,nm/m\epsilon$ and unloading fitting $\gamma_{(7,6)-(7,5)} = 0.9\,nm/m\epsilon$. In load-unload cycle 4 as shown in Figure 2.8 (right), load fitting $\gamma_{(7,6)-(7,5)} = 0.9\,nm/m\epsilon$ and unloading fitting $\gamma_{(7,6)-(7,5)} = 1.3\,nm/m\epsilon$.

In the load-unload cycle 5 as shown in Figure 2.9 (left), load fitting $\gamma_{(7,6)-(7,5)} = 0.9\,nm/m\epsilon$ and unloading fitting $\gamma_{(7,6)-(7,5)} = 1.1\,nm/m\epsilon$. In the load-unload cycle 6 as shown in Figure 2.9 (right), load fitting $\gamma_{(7,6)-(7,5)} = 1.1\,nm/m\epsilon$ and unloading fitting $\gamma_{(7,6)-(7,5)} = 1.1\,nm/m\epsilon$.

In the load-unload cycle 7 as shown in Figure 2.10 (left), load fitting $\gamma_{(7,6)-(7,5)} =$

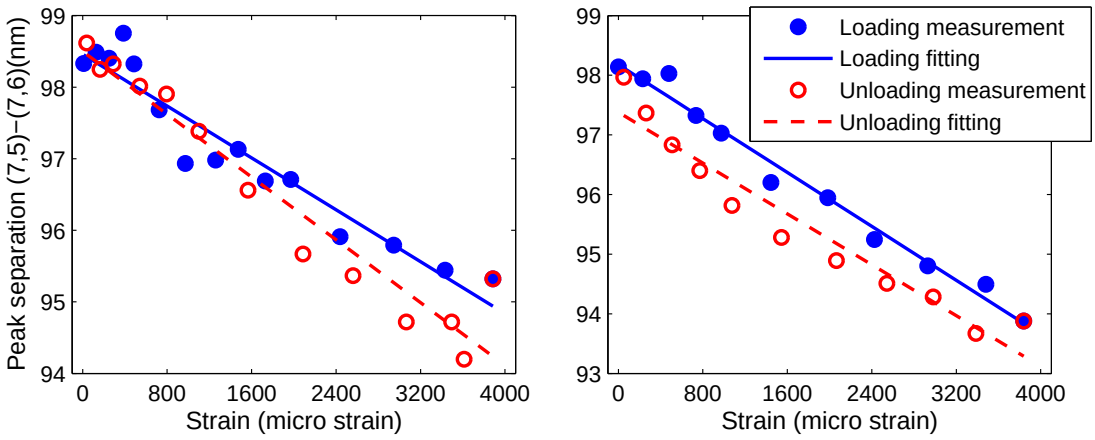

Figure 2.9 : Strain variation of differential spectral shift (left) load-unload cycle 5 (right) load-unload cycle 6.

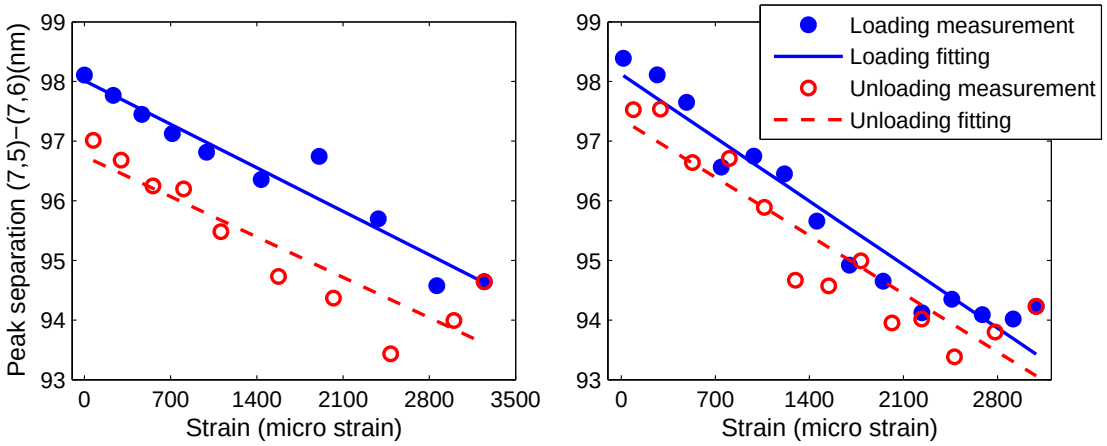

Figure 2.10 : Strain variation of differential spectral shift (left) load-unload cycle 7 (right) load-unload cycle 8.

$1.0\,nm/m\epsilon$ and unloading fitting $\gamma_{(7,6)-(7,5)} = 1.0\,nm/m\epsilon$. In the load-unload cycle 8 as shown in Figure 2.10 (right), load fitting $\gamma_{(7,6)-(7,5)} = 1.5\,nm/m\epsilon$ and unloading fitting $\gamma_{(7,6)-(7,5)} = 1.4\,nm/m\epsilon$.

In the load-unload cycle 9 as shown in Figure 2.11 (left), load fitting $\gamma_{(7,6)-(7,5)} =$

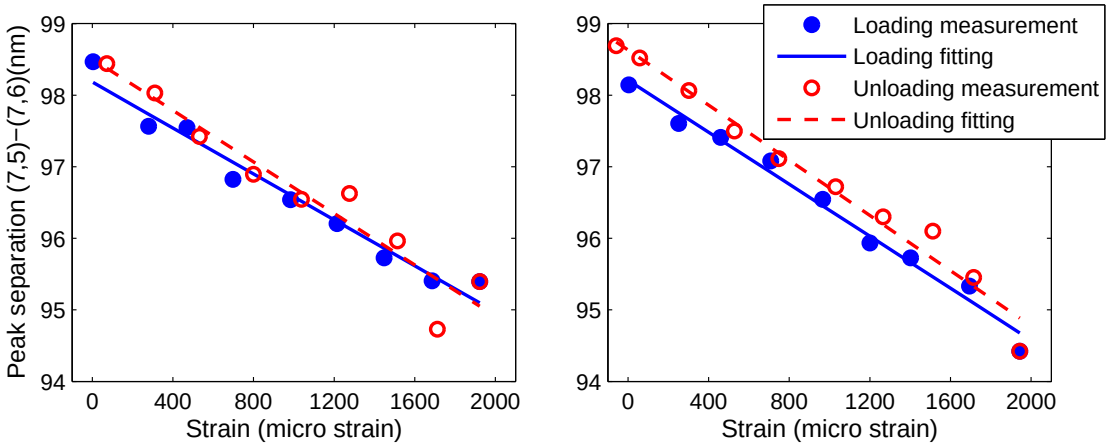

Figure 2.11 : Strain variation of differential spectral shift (left) load-unload cycle 9 (right) load-unload cycle 10.

$1.6\,nm/m\epsilon$ and unloading fitting $\gamma_{(7,6)-(7,5)} = 1.8\,nm/m\epsilon$. In the load-unload cycle 10 as shown in Figure 2.11 (right), load fitting $\gamma_{(7,6)-(7,5)} = 1.8\,nm/m\epsilon$ and unloading fitting $\gamma_{(7,6)-(7,5)} = 1.9\,nm/m\epsilon$.

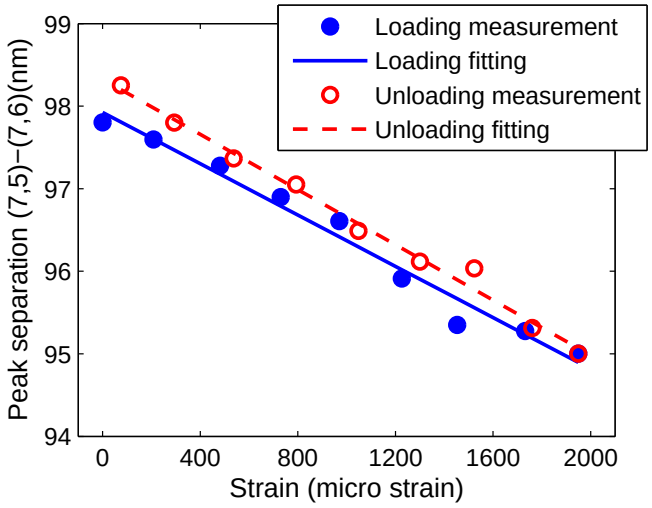

Figure 2.12 : Strain variation of differential spectral shift, load-unload cycle 11.

In the load-unload cycle 11 as shown in Figure 2.12, load fitting $\gamma_{(7,6)-(7,5)} =$

1.6 $nm/m\epsilon$ and unloading fitting $\gamma_{(7,6)-(7,5)} = 1.7\, nm/m\epsilon$.

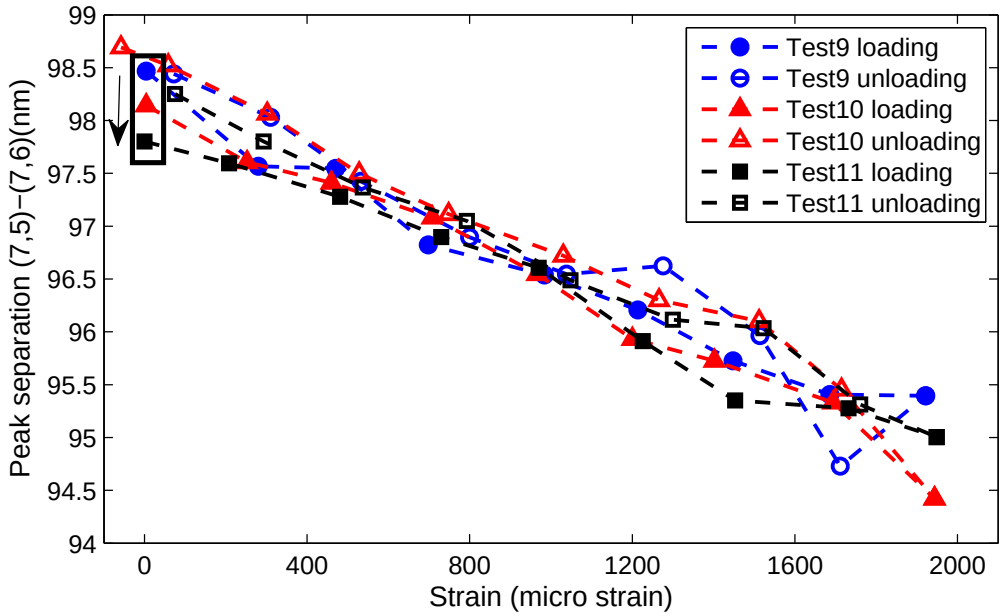

Figure 2.13 : Strain variation of differential spectral shift, load-unload cycle 9- 11.

From cycle 1 to cycle 11, the S^4 film is subjected to cyclic deformation with uniform maximum strain level using a four-point bending gig. As the tensile mechanically cyclic deformation is added on the S^4 film, the strain sensitivity $\gamma_{(7,6)-(7,5)}$ of the SWCNTs increases in general. For example, $\gamma_{(7,6)-(7,5)}$ increase from 0.9 $nm/m\epsilon$ in the 3rd loading half-cycle to 1.6 $nm/m\epsilon$ and $\gamma_{(7,6)-(7,5)}$ increase from 1.3 $nm/m\epsilon$ in the 3rd loading half-cycle to 1.7 $nm/m\epsilon$. Further as the cycle number increases, the shift pattern in loading half-cycle and the one in unloading half-cycle become much more consistent.

As the sample undergoes subsequent deformation cycles from 9 to 11, the S^4 film is subjected to cyclic deformation with uniform maximum strain level of 2000 $\mu\epsilon$ at each cycle. At the end of each cycle from 9 to 11, the peak separation of (7,6)-(7,5),

$\lambda_{(7,6)-(7,5)}$, at 0% strain is at lower wavelength than in the previous cycle. This means the residual tensile strain that occurs in the film. As shown in Figure 2.13, the black box at 0% strain indicates the behavior of the residual tensile stresses at the end of the deformation cycles.

2.6 Concluding Remarks

The results obtained from first-generation S^4 tests demonstrate proof-of-principle for the method. The linear dependence of peak response to applied strain has been investigated in both numerical simulation and experiments. It should be feasible to measure a strain field over a wide area simply by moving the optical system to each point of interest and capturing emission spectra for several polarization settings of the excitation beam. The measurement grid can be as coarse or fine as desired, because the SWCNTs are present throughout the coating. To obtain absolute strain values, one can apply empirical calibrations determined for the specific Smart Skin formulations and application methods that are used. Of course, for real field applications it is also necessary to have a strain reader system that is small and lightweight enough to be readily portable.

The preliminary studies in this chapter find that a consumer-grade urethane-based varnish seems to be a promising host material for S^4 films. However, properties of the polymeric film material are very important in practical implementations of this non-contact strain sensing method. The material must be reasonably transparent for the red and near-IR wavelengths of nanotube excitation and emission, and it should not significantly quench the intrinsic fluorescence of embedded SWCNTs. It also needs to support dispersions of individualized SWCNTs, to have a good interfacial adhesion, to display mechanical and environmental durability. Properties of the SWCNTs used

in the film are also very important. The nanotubes should be nearly pristine and unbundled to give bright near-IR fluorescence, and should have a good abundance of those specific (n, m) species used in the spectral analysis. The efforts in selecting materials for optimum strain-sensing application will be described in the following chapters.

Chapter 3

Development of Generation-II S^4 Films

3.1 Introduction

The principle of strain sensing technology by using fluorescence properties of SWCNTs has been demonstrated in Chapter 2. Raw SWCNTs are embedded in a thin urethane based polymer film that is applied to the surface of interest to give a thin "strain-sensing smart skin" or "S^4" film. The surfaces of interest might include aircraft wings and fuselages, helicopter body and rotors, building beams and columns, bridge beams and piers, pressure vessels and pipelines. Each SWCNT in the film acts as a sensor, and strain can be measured anywhere on the surface by irradiating that point with an interrogating laser beam and by collecting and analyzing the resulting nanotube fluorescence spectrum. The strain in any direction can also be found by rotating the polarization plane of the laser beam to selectively interrogate SWCNTs oriented in that direction.

The S^4 method exploits the unique photoluminescence properties of SWCNTs, which exist in a variety of distinct structural forms, each of which is labeled by a pair of integers (n, m) and has a specific diameter and roll-up angle. Most SWCNT structures are direct band gap semiconductors. Each of these semiconducting SWCNTs shows a sharp photoluminescence (fluorescence) peak at a short-wave infrared (SWIR) wavelength characteristic of that structure. The focus of our method is to track the changes in these peak positions, as it has been shown through theory and

experiment that axial stretching or compression of SWCNTs causes predictable systematic changes [1] in their band gaps and corresponding shifts in their spectra as shown in Figure 3.1. Our laboratory has also demonstrated that for bulk SWCNTs embedded in a polymer under a tensile load, there is a linear relation between the strain on the test surface and shifts in the measured nanotube spectral peak positions. [39, 40] Therefore, by capturing fluorescence spectra of the carbon nanotubes from an arbitrary point on the surface, this linear relation allows the strain state at that point to be determined. In addition to the ubiquitous and multi-directional nature of this sensing approach, a further advantage is that the sensing element is a thin, non-perturbing film that should need little maintenance.

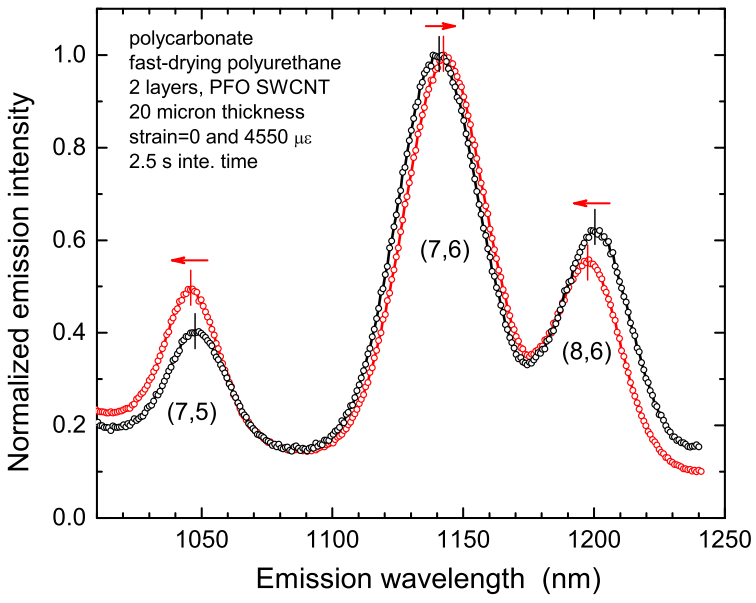

Figure 3.1 : SWCNT fluorescence spectral shifts due to strain.

There are several challenges to practical implementation of the S^4 method. One

is tailoring the SWCNT composition and dispersion in the composite film so as to optimize the precision with which fluorescence peak positions can be found. Another is developing instrumentation that can efficiently generate, capture, and interpret fluorescence spectra from the S^4 film, yet remain small and light enough for hand-held field use. Progress toward both of these goals is described below in the following sections.

3.2 SWCNTs Nanocomposite Suspension Treatment

3.2.1 Ultrasonication

SWCNTs often aggregate into long ropes or bundles either during preparation or after being suspended for an extended period. These bundles and ropes significantly decrease the homogeneity of the suspension (and by extension, the film), and result in ineffective load transfer between the polymer and the nanotubes. The bundles can also perturb the electronic structure of the tubes [30], quenching the IR fluorescence. By ultrasonicating the suspension prior to application on a surface, it is possible to greatly reduce the aggregation of the nanotubes. This process is one of the most important steps in preparing this skin, as agitation of the nanotubes can significantly increase the fluorescence intensity by separating and dispersing SWCNTs within suspension. In this study, the film suspensions are ultrasonicated using a tip sonicator at about 1 W/mL for varying durations.

3.2.2 Centrifugation

SWCNTs have a strong tendency to form parallel bundles or ropes through inter-tube van der Waals interactions [30]. In addition, the raw nanotubes that are mixed with

the polymer also often contain numerous impurities such as residual catalysts, which are products of the nanotube manufacturing process. As these unwanted bundles, ropes, and residual materials can hinder effective load transfer from the host polymer to the nanotubes, purification is needed. After raw nanotubes have been dispersed, performing centrifugation on nanocomposite suspensions can help remove some of the waste and purify SWCNTs. The nanocomposite suspensions are centrifuged at speeds ranging from 2,500 to 13,000 RPM and at duration ranging from 10 to 60 minutes. Once the suspension has been centrifuged, the supernatant is carefully decanted for use instantly.

3.2.3 Filtration

Filtration of the film suspension is also tested as an alternative to centrifugation for removing unwanted bundles and residual material. The filter can potentially remove the larger ropes and bundles present in the untreated suspension. A hydrophobic PTFE membrane with a pore size of 5 μm is placed in a filter holder, and the suspension is forced through the filter with a syringe.

Although forcing the suspension through a filter can give an improvement in stability and intensity, the filtration treatment is very time consuming. In this study, ultrasonication is the pre-treatment to disperse SWCNTs within polymer suspension; while filtration and centrifugation are the post-treatments to purify SWCNTs.

3.3 Material Study

3.3.1 Nanotubes

The traditional methods for SWCNT synthesis include laser ablation, arc-discharge and chemical vapor deposition (CVD). In this study, HipCO and CoMoCAT SWCNTs are investigated. The high-pressure carbon monoxide (HiPco) process (603 Kb) is developed at Rice University to create single-walled carbon nanotubes (SWCNT) from the gas-phase reaction of iron carbonyl with high-pressure carbon monoxide gas. The HiPco SWCNT is a fluffy-fibrous material with a bulk density of about 0.1 g/cm^3.

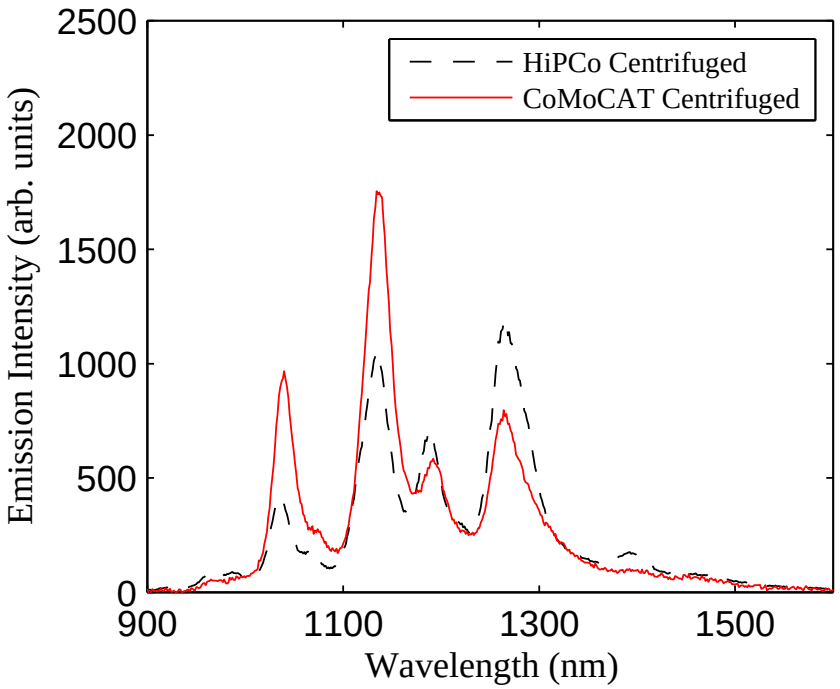

Figure 3.2 : Comparison of fluorescence of SWCNTs from different sources after centrifugation.

However, the HiPco method produces nanotubes with a wide distribution of diam-

eter and chirality. An alternative CVD approach achieves high selectivity of SWNT formation using a silica-supported Co-Mo catalyst (CoMoCAT). [41]

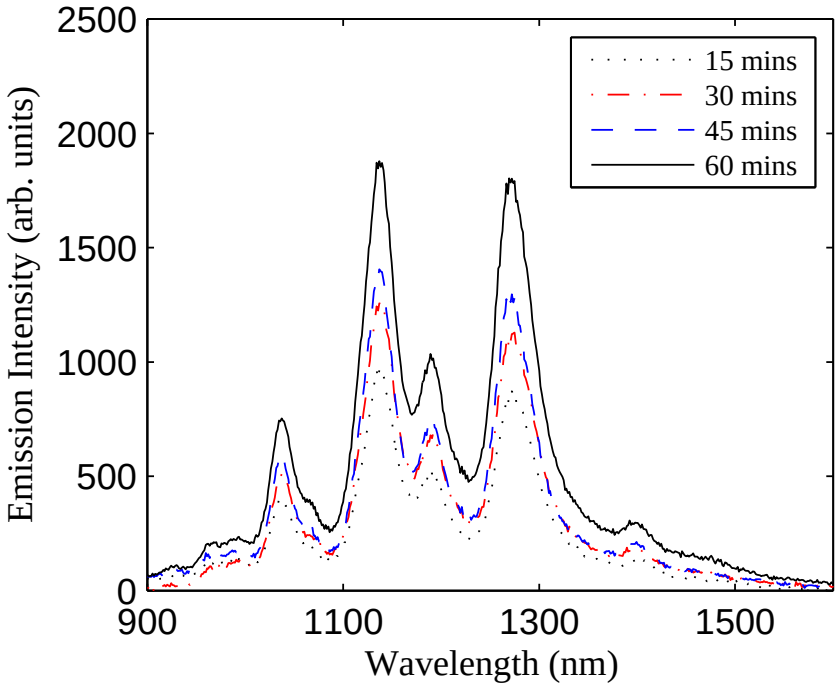

Figure 3.3 : Fluorescence of SWCNT suspension after ultrasonication for various times.

Figure 3.2 shows fluorescence results from centrifuged (5K RPM for 20 min) PMMA-xylene mixture samples of both HiPco SWCNTs and CoMoCAT SWCNTs. It can be seen clearly that the (7,5) and (7,6) peaks near 1040 and 1140 nm are very dominant for CoMoCAT nanotubes: they are about two times more intense than those of HiPco. These clear peaks of CoMoCAT nanotubes might be helpful in strain measurement using smart skin. However, HiPCo SWCNTs are less dense than CoMoCAT and this might be easier for HiPCo SWCNTs to be dispersed well within suspension.

3.3.2 Polymers

Polyurethane(PU)

Polyurethane (PU) is a polymer composed of organic units joined by carbamate (urethane) links. Polyurethane products often are simply called "urethanes", but should not be confused with ethyl carbamate, which is also called urethane. Polyurethanes neither contain nor are produced from ethyl carbamate. [42] In this dissertation, urethane typically refers to the former one rather than ethyl carbamate.

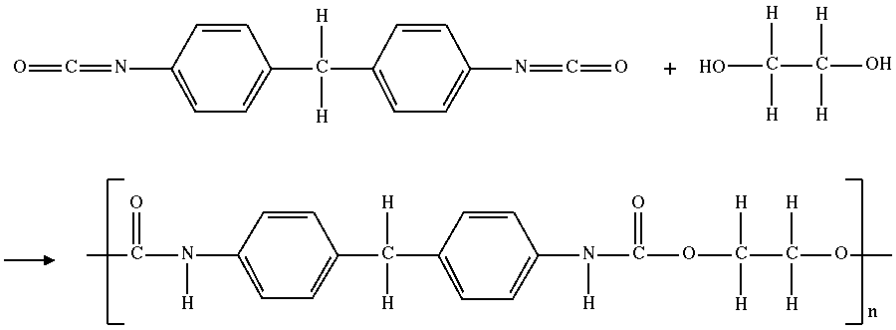

Figure 3.4 : Example of polyurethane synthesis, wherein the urethane groups NH(C=O)O link the molecular units. [2]

PU are formed by chemical reaction between a di/poly isocyanate and a diol or polyol, forming repeating urethane groups, generally, in presence of a chain extender, catalyst, and/or other additives. Often, ester, ether, urea and aromatic rings are also present along with urethane linkages in PU backbone [42]. Because a variety of diisocyanates and a wide range of polyols can be used to produce polyurethane, a broad spectrum of materials can be produced to meet the needs of specific applications. An example of polyurethane synthesis and the chemistry structure of the PU is shown in Figure 3.4. In a commercial urethane or polyurethane based product, the number of

urethane groups varies very much.

Poly(methyl methacrylate) (PMMA)

Poly(methyl methacrylate), also as known as acrylic or PMMA, is a transparent plastic, often used as a lightweight and shatter-proof replacement for glass. PMMA can be utilized as a casting resin, in inks and coatings, and as in other applications. One of the most common and useful reaction for making polymers is free radical polymerization. Free radical polymerization is used to make polymers from vinyl monomers (small molecules containing carbon-carbon double bonds). In Figure 3.5, PMMA can be made by free radical vinyl polymerization from the monomer methyl methacrylate.

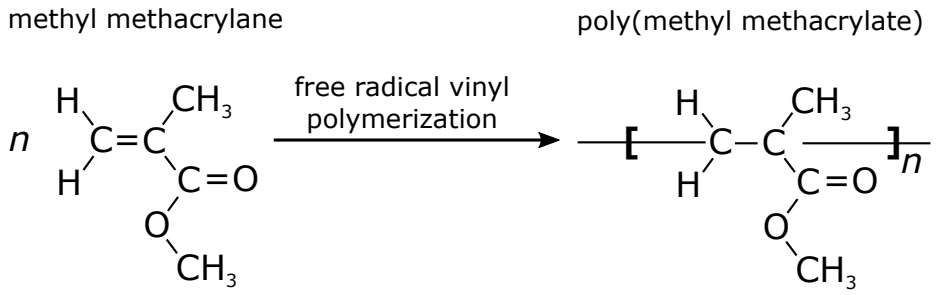

Figure 3.5 : PMMA made by free radical vinyl polymerization from the monomer methyl methacrylate.

SWCNT fluorescence spectrum sequences are measured by spectrometer as shown in Figure 3.6. Table 3.1 shows the statistics of (7,6) spectrum peak of SWCNTs-PMMA-xylene suspension with different short PMMA concentration. Average peak emission intensity and coefficient of variation of the (7,6) peak are two important features that can represent the strength and stability of a liquid sample consisting of CoMoCAT SWCNTs, PMMA and xylene.

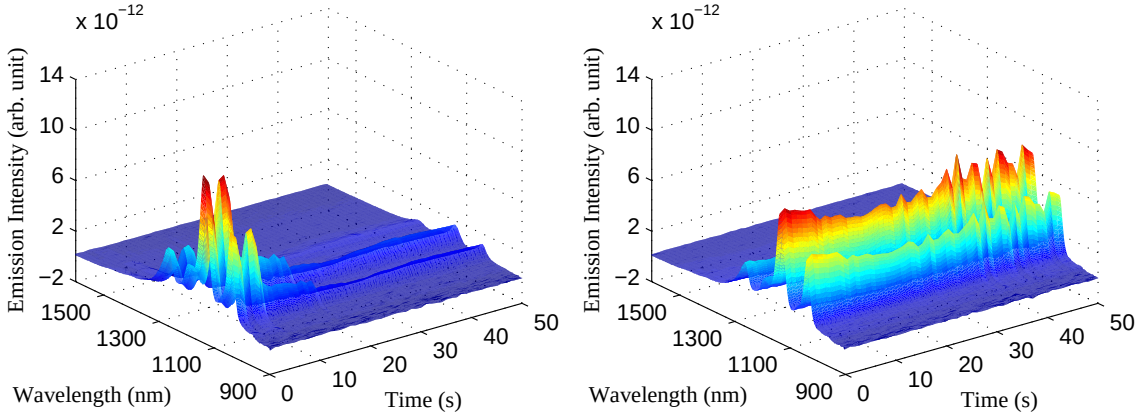

(a) before filtration

(b) after filtration

Figure 3.6 : Spectrum sequence of S-D06 before and after filtration.

Table 3.1 : Statistics of (7,6) spectrum peak of SWCNTs-PMMA-xylene suspension with different short PMMA concentration.

Suspension label	PMMA/NTs/xylene	mean (10^{-12})	std[1](10^{-12})	cov[2]
S-D06	short 3 g/1.5 mg/15 mL	10.975	1.285	0.095
S-D07	short 2.6 g/1.5 mg/15 mL	6.707	0.949	0.164
S-D08	short 2.2 g/1.5 mg/15 mL	4.096	0.885	0.347

[1] std is standard deviation;

[2] cov is coefficient of variation.

With SWCNTs concentration constant(SWCNT/xylene=0.010 g/mL), the influence of short PMMA (MW=35,000) concentration(PMMA/xylene) on fluorescence of SWCNTs has been investigated by varying from 0.147 g/mL to 0.200 g/mL. From Table 3.1, it is seen that a higher concentration improves fluorescence stability and intensity.

Table 3.2 : Study of different post treatment methods on S-D06.

Treatment method	PMMA/NTs/xylene	mean (10^{-12})	std (10^{-12})	cov
No post treatment	short 3 g/1.5 mg/15 mL	10.975	1.285	0.095
After centrifugation	short 3 g/1.5 mg/15 mL	4.685	0.207	0.044
After filtration	short 3 g/1.5 mg/15 mL	13.640	0.538	0.039

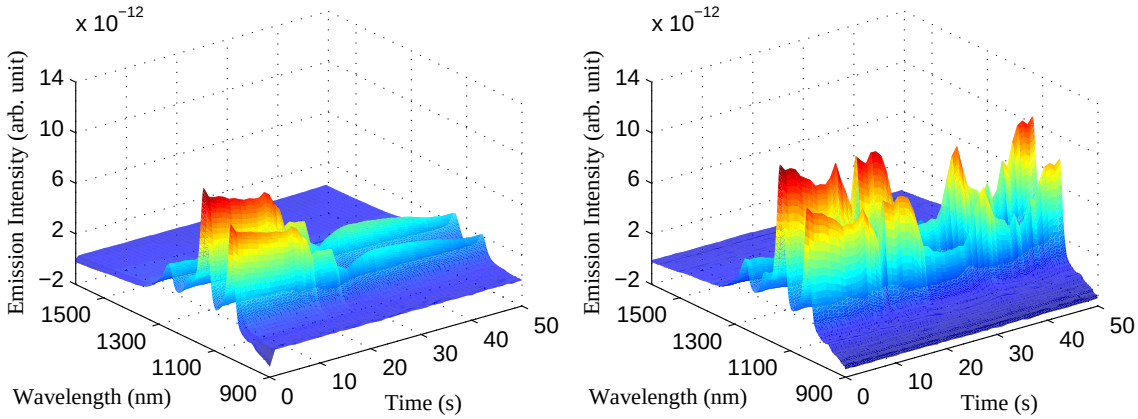

(a) before filtration

(b) after filtration

Figure 3.7 : Spectrum sequence of S-E06 before and after filtration.

Keeping SWCNTs constant(SWCNT/xylene=0.0067 g/mL), the influence of long PMMA (MW=350,000) concentration(PMMA:xylene) on fluorescence of SWCNTs has been investigated by varying from 0.060g/mL to 0.150g/mL. From the section "Influence of long PMMA concentration" within Table 3.1, it is shown that PMMA concentration at 0.12 g/mL had the greatest stability with smallest c.o.v.(coefficient of variation)=0.073, but the weakest signal with average peak intensity=2.67x10^{-12}; long PMMA concentration at 0.09 g/mL had the strongest signal with average peak intensity=5.82x10^{-12} and had a acceptable stability with c.o.v.=0.252.

Based on a series of tests, it is found that long PMMA (with Mw=350,000) is better than short PMMA (MW=35,000) at the same concentration(PMMA/xylene). The longer fibers of PMMA can better confine the SWCNTs and provide a more stable structure once xylene within liquid sample evaporates and the sample becomes solid. Thus, the recent studies are mostly focused on long PMMA rather than short PMMA. The optimum long PMMA concentration(PMMA/xylene) is around 0.09 g/mL based on the results.

Table 3.3 : Statistics of (7,6) spectrum peak of SWCNTs-PMMA-xylene suspension with different long PMMA concentration before filtration.

Suspension label	PMMA/NTs/xylene	mean (10^{-12})	std (10^{-12})	cov
S-E06	long 2.25 g/1.0 mg/15 mL	5.486	2.441	0.445
S-E07	long 1.8 g/1.0 mg/15 mL	2.670	0.195	0.073
S-E08	long 1.35 g/1.0 mg/15 mL	5.815	1.467	0.252
S-E09	long 0.9 g/1.0 mg/15 mLL	3.645	1.469	0.403

Table 3.4 : Statistics of (7,6) spectrum peak of SWCNTs-PMMA-xylene suspension with different long PMMA concentration after filtration.

Suspension label	PMMA/NTs/xylene	mean (10^{-12})	std (10^{-12})	cov
S-E06	long 2.25 g/1.0 mg/15 mL	8.387	2.561	0.305
S-E07	long 1.8 g/1.0 mg/15 mL	12.055	1.260	0.104
S-E08	long 1.35 g/1.0 mg/15 mL	14.970	1.460	0.097
S-E09	long 0.9 g/1.0 mg/15 mLL	3.560	0.897	0.250

Dispersion of SWCNTs within polymeric host should be checked in order to obtain a stable nano structure of smart skin. TS17 and TS18 (details shown in Table 3.4)

are examined using short-wave IR microscopic spectrometer. Figure 3.8 show the nonuniform dispersion of nanotubes clearly: the light area indicate the distribution of the nanotubes within the polymeric film and the dark area indicates PMMA; the resolution of measuring strain using smart skin is about 50 μm. This indicates that the filtration has little improvement in NTs' dispersion. This results is maybe due to the large size of the pore filter (5 μm). 5 μm seems to be too large to filter all the clusters of nanotubes. We will investigate this issue in the near future.

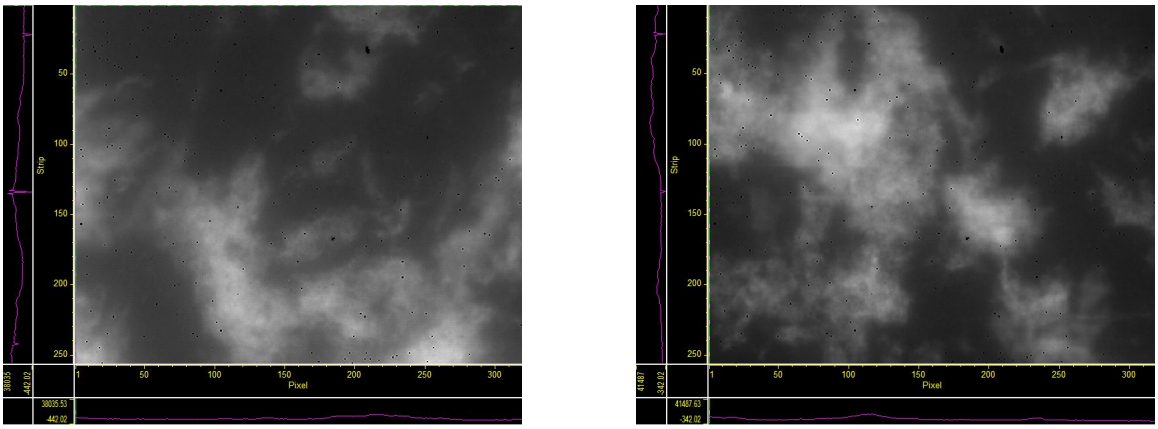

(a) TS17 (b) TS18

Figure 3.8 : 2D fluorescence microscopy on slide TS17 and TS18 (160 μm x 120 μm in space)

Poly(9,9-di-n-octylfluorenyl-2,7-diyl) (PFO)

Poly(9,9-di-n-octylfluorenyl-2,7-diyl), also known as F8 or PFO, is a polyfluorene specifically optimized for a variety of organic electronic applications. Most of researchers are interested in polyfluorene polymers because of their optical and electrical properties with applications on organic light-emitting diodes (OLEDs) and

polymer solar cells. Nish et. al. [43] used polyfluorene polymers in the preparation of SWCNTs solutions to efficiently disperse certain nanotube species with a high degree of selectivity. In their study, poly[9,9,dioctylfluorenyl-2,7-diyl] (PFO), poly[9,9-dihexylfluorenyl-2,7-diyl] (PFH), poly[(9,9-dioctylfluorenyl-2,7-diyl)-co-(1,4-phenylene)] (PFO-P) and poly[(9,9-dioctylfluorenyl-2,7-diyl)-alt-co-(1,4-benzo-2,10,3-thiadiazole)] (PFO-BT) are researched with both HiPCO and CoMoCAT SWCNTs. Photoluminescence excitation maps of SWCNTs in the solvent toluene using the polymers are studied. It is shown that PFO has particularly strong selectivity in extracting the (7,5), (7,6),(8,6), (8,7) and (9,7) near-armchair species. [43, 44] The chemical structure of PFO is shown in Figure 3.9.

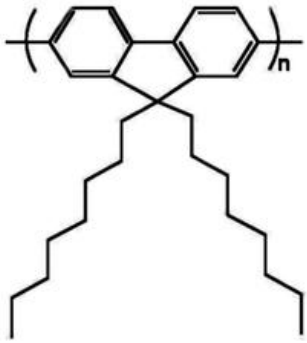

Figure 3.9 : Chemical structure of PFO.

3.4 Film Application Method

Successful application of a smooth polymeric film with well dispersed SWCNTs is of great importance in assuring accurate strain measurements. In our previous work [40], spin coating, brush coating and spray coating have been investigated to find some useful guidelines for applying the smart skin on metal substrates, such as aluminum,

steel and polymer.

According to the research in the previous sections, for given polymer matrix and organic solvent, the thickness of smart skin done by spin coating can be controlled primarily by the polymer concentration, the solution viscosity, and the spinning speed. Walsh et. al. [45] found the other parameters include the rate of solvent evaporation, which depends on the mass transfer coefficient from the liquid to the gas phase, the fluid flow conditions in the gas phase, spin time, and other processing details. The processing parameters affect the rheological properties of the polymer solution from the initial concentration to the highly viscous state when flow stops.

3.4.1 Spin coating method

Spin coating is a coating method achieved by dripping small amounts of polymer suspension onto a rapidly spinning substrate. The SWCNT-polymer-organic solvent mixture is spin-coated onto a slide that had been cleaned beforehand. The applied substrate is then allowed to dry under ambient conditions for about 3 minutes. Spin coating is repeated until the emission intensity of the smart skin is strong enough, and the sample is allowed to cure for hours or days (it depends on the polymer type and organic solvent type) at room temperature prior to measurements. The spin coating apparatus, as shown in Figure 3.10, allows the speed of the slide to be controlled by varying the voltage on motor.

After S^4 films have been applied and cured, a CG 204 Coating Thickness Tester is used to measure the thickness of the polymeric film. Investigations of the influence of long PMMA concentration on polymeric film thickness are shown in Table 3.5 with various parameters, such as PMMA concentration, spin speed, tip sonication.

The "Spin speed (0.075 g/mL)" section within Table 3.5 shows that with the in-

Figure 3.10 : Spin coating apparatus

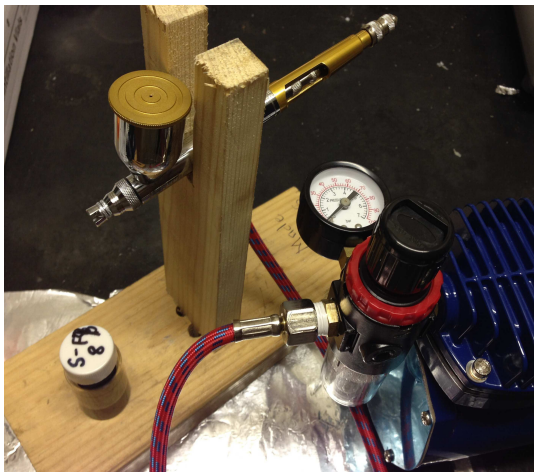

Figure 3.11 : Spray coating apparatus.

crease in spinning speed, the thickness of polymer layer decreases; and that 0.075 g/mL PMMA concentration is too low for preparing smart skins, because the ultimate thicknesses are less than 2.5 μm. From the investigations on liquid samples in Table 3.1 and 3.3, it is already known that long PMMA concentrations around 1 g/mL are best for strong and stable fluorescence of SWCNTs. Hence, we shifted our focus to PMMA-xylene suspensions with concentrations of 0.100 g/mL.

The "Spin speed (0.1 g/mL)" section within Table 3.5 shows: (1) Spinning motor voltage should be larger than 5 V for this suspension, otherwise coating could not cover the substrate uniformly; (2) the thickness jump of TS 4 and TS 7 might be due to the nonuniformity that is caused by the first few layers, so that the liquid is confined within the center area and this subsequently increased the thickness of the last two layers dramatically; (3) comparison between TS4, TS5, TS6, TS7 and TS8 shows that 8 V is the optimum speed for 0.1 g/mL PMMA suspension; (4) Little difference between TS9 and TS10 shows that 3 min is enough for the suspension (0.1 g/mL) to dry completely; (5) increase in the viscosity of suspension would lead to

Table 3.5 : Parametric studies of influences on film thickness (long PMMA,spin coating)

Parameter	Slide label	Suspension description			Spin speed	Amt /lyr	Interval	Thickness(μm)		
		PMMA/xylene	NTs	Sonic.				3 lyr	5 lyr	7 lyr
Speed (0.075 g/mL)	TS1	0.075g/mL	No	No	5 V	0.2 mL	2 min	1.00	2.10	2.50
	TS2	0.075 g/mL	No	No	10 V	0.2 mL	2 min	1.30	1.80	2.00
	TS3	0.075 g/mL	No	No	15 V	0.2 mL	2 min	1.20	1.30	1.40
Speed (0.1 g/mL)	TS4	0.10 g/mL	No	No	5 V	0.2 mL	2 min	2.40	11.70	15.90
	TS5	0.10 g/mL	No	No	10 V	0.2 mL	2 min	1.20	2.60	3.20
	TS6	0.10 g/mL	No	No	15 V	0.2 mL	2 min	1.10	1.80	2.50
	TS7	0.10 g/mL	No	No	7 V	0.2 mL	2 min	1.80	3.20	11.80
	TS8	0.10 g/mL	No	No	8 V	0.3 mL	3 min	2.00	3.10	11.80
	TS9	0.10 g/mL	No	No	8 V	0.3 mL	3 min	2.20	3.30	13.00
	TS10	0.10 g/mL	No	No	8 V	0.3 mL	5 min	2.20	3.30	13.00
SWCNTs concentration	TS11	0.10 g/mL	Yes	Yes	8 V	0.3 mL	5 min	1.10	1.70	2.50
	TS12	0.10 g/mL	Yes	Yes	8 V	0.3 mL	5 min	1.40	1.70	2.40
Sonication	TS13	0.12 g/mL	No	No	8 V	0.3 mL	5 min	3.10	15.50	22.00
	TS14	0.12 g/mL	No	Yes	8 V	0.3 mL	5 min	1.50	2.90	10.80

exponential growth of film thickness.

By comparing TS13 and TS14 slide samples shown in Table 3.5, we observe a dramatic decrease in film thickness from 22.00 μm to 10.80 μm. Referring to TS 10, we conclude that due to tip ultrasonication at a power of 15 W (15 s on, 15 s off duty cycle) for 1 hour, the viscosity of PMMA-xylene suspension at 0.12 g/mL dropped to that of PMMA-xylene suspension of concentration at less than 0.10 g/mL. This happens because tip sonication will make PMMA length shorter, which changes the

viscosity. Hence the influence of tip sonication on viscosity of PMMA suspensions should be considered in future research.

Table 3.6 : Influence of post filtration on polymer film thickness.

Slide Label	Suspension Description				Spinning speed	Interval	Thk.(μm) 7 lyr
	PMMA	PMMA/ NTs/xylene	Sonication	Filtration			
TS15	Short	0.2 g/0.1 mg/mL	1 hour	No	8 V	5 min	24.30
TS16	Short	0.2 g/0.1 mg/mL	1 hour	Yes	8 V	5 min	22.20
TS17	Long	0.09 g/0.067 mg/mL	1 hour	No	8 V	3 min	15.80
TS18	Long	0.09 g/0.067 mg/mL	1 hour	Yes	8 V	3 min	15.70

Table 3.6 lists results on the effect of filtration on film thickness. By comparing the thickness of polymeric film on TS15 and TS16, we can find filtration does not affect the viscosity of short PMMA-xylene suspensions very much. By comparing the thickness of polymeric films TS17 and T18, we see that filtration also does not affect the viscosity of long PMMA-xylene suspensions very much.

3.4.2 Spray coating method

Spray coating is a coating method that applies the polymer suspension onto a substrate using an airbrush. Compared to spin coating, spray coating has an advantage in scalability. The SWCNTs-polymer suspension (with low viscosity) can be spray-coated onto a large substrate surface using an airbrush and D500SR air compressor shown in Figure 3.11. The film is then allowed to dry within an enclosed environment at room temperature for hours in order to get a smooth polymer surface. The flow speed of the coating can be controlled by both the air pressure and the controller on the airbrush.

Here, it should be mentioned that, is not possible to use air brush to coat structural surfaces by the Generation-I S^4 films because of the high viscosity. Instead of spray coating, brush coating and spin coating methods are used to perform Generation-I S^4 film application. In Chapter 4, we will propose a new Generation of S^4 films, which can be spray coated onto large structural surface.

Table 3.7 : List of slide samples applied by spray-coating

Slide label	Long PMMA /NTs /xylene	Pressure (psi)	Cont. (rnd)	Thickness (μm)	
				center	bubble
AN1	1.5 g/1 mg/15 mL	40	2	1.4	3∼21
AN2	1.5 g/1 mg/15 mL	30	3	0.6∼2.2	3∼67
AN3	1.5 g/1 mg/15 mL	30	3	0.8∼1.5	3∼58
AN4	1.5 g/1 mg/16.67 mL	35	3	0.3	1.2∼13
AN5	1.5 g/1 mg/16.67 mL	35	3	0.2	3∼16
AN6	1.5 g/1 mg/16.67 mL	40	3	3.1∼15.7	-
AN7	1.5 g/1 mg/16.67 mL	40	3	1.7∼15.1	-

Table 3.7 shows the slide samples applied by spray-coating. In this study, the PMMA/NTs content is kept constant at 1.5 g/1 mg in order to get similar fluorescence features from different polymeric films with various thickness. First, PMMA-SWCNTs-xylene mixtures with PMMA/xylene=0.10 g/mL are applied onto slides AN1-AN3 with various controller positions and air pressures. By observing the slides, we found that higher air pressures give smaller air bubbles: when using 40 psi there are no air bubble within the polymeric film. The thickness of film in samples AN2 and AN3 containing air bubbles could be as thick as 50-60 μm. Hence, in order to reduce air bubble size, we diluted the suspension to PMMA/xylene=0.09 g/mL to

reduce viscosity. And we increased the air pressure to 35 psi and 40 psi expecting to remove most of bubbles. The air bubbles on AN6 and AN7 are gone, but the surface of polymer is still not very smooth with thickness $1.7 \sim 15.1\ \mu m$.

3.5 Design of Generation-II S^4 Films with PFO Treatment

We begin with raw SWCNTs grown in the Rice University HiPco reactor. These samples contain nanotubes with varied (n, m) structures are aggregated into bundles bound by van der Waals forces. There are also impurities such as amorphous carbon, giant fullerenes, and metallic catalyst residue from the nanotube growth process. For our application, this material should be processed to disaggregate the bundled SWCNTs [30], remove impurities, and select a subset of the (n, m) structures so as to simplify the S^4 fluorescence spectrum and allow more precise determination of peak wavelengths. We use a combination of selective dispersion and centrifugation to address these goals.

Dispersion is achieved using the organic polymer poly(9,9-dioctylfluorenyl-2,7-diyl), or PFO, which is known to selectively coat and solubilize a small set of SWCNT structures having roll-up angles near 30 degrees (see Figure 3.12). We add solid PFO to toluene at a mass concentration of 1 mg/mL and use tip ultrasonication for 60 min at a power of 1 W/mL (with a duty cycle of 20 s on, 40 s off) to dissolve the PFO. Raw SWCNTs grown in the Rice University HiPco reactor are then added to the PFO/toluene solution at a concentration of 1 mg/mL as shown in Figure 3.16. To disperse the nanotubes, the mixture is tip ultrasonicated at a power of 1 W/mL (20 s on, 40 s off) for 15 to 45 min until the sample appears homogeneous. We then centrifuge it for 30 min at 13,000 RPM at 25 $^{\circ}C$ to pellet out impurities. After centrifugation, the supernatant containing disaggregated, selected SWCNTs

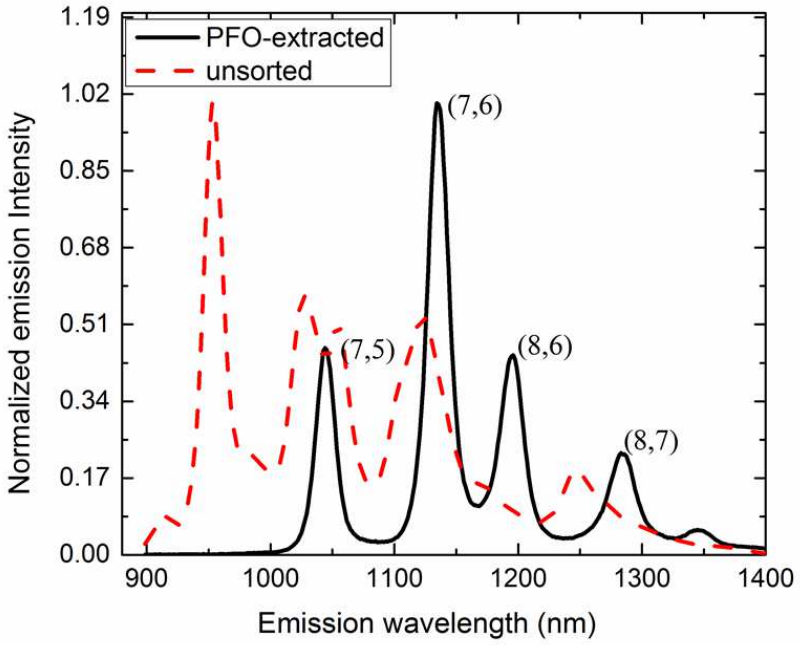

Figure 3.12 : Fluorescence spectra from an unsorted dispersion of HiPco SWCNTs (red dashed line) and a HiPco sample extracted into a toluene solution of PFO (black solid line). Peaks from the PFO-extracted sample are labeled with the corresponding (n, m) indices.

coated with PFO is carefully pipetted out and added to a commercial exterior varnish (Minwax Helmsman Spar Urethane, 350 VOC compliant) at a volume ratio of 1:1. After having explored several potential polymeric host materials, we find that this varnish provides adequate nanotube compatibility, transparency at the excitation and fluorescence wavelengths, adhesion, and durability in exterior applications. The composite is mixed by tip ultrasonication for 6 min at a power of 1 W/mL (20 s on, 40 s off) and then more varnish is added to increase the volume by 50%. That mixture is then tip ultrasonicated for another 6 min. One should note that although longer

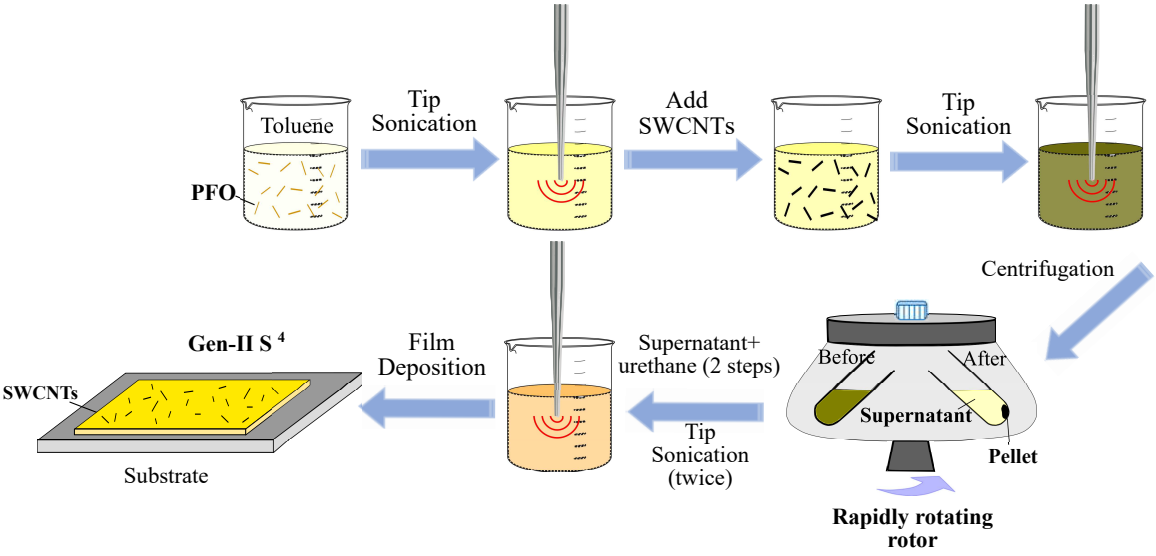

Figure 3.13 : Fabrication procedures of Generation-II S^4 films.

ultrasonication leads to improved dispersion, it also causes nanotube cutting, giving a larger number of shorter nanotubes that appear to be less efficient in load transfer from the host polymer. We therefore carefully chose the duration of ultrasonication to balance nanotube dispersion and length.

Successful application of a smooth polymeric film with well dispersed SWCNTs is of great importance in assuring accurate strain measurements. For these tests, we spin-coat the composite containing SWCNTs, PFO, toluene, and urethane varnish onto a PMMA bar (76 x 19 x 6.35 mm) or an steel/aluminum slide (76 x 25 x 1 mm) that had been surface-cleaned using ethanol and Kimwipes to remove organic contaminants. The applied film is then allowed to dry under ambient conditions. The thickness of first film layer prepared in this way may be as low as 4 μm on a steel/aluminum substrate or 10 μm on PMMA. In order to increase the measured fluorescence intensities, we sometimes apply one or two additional layers by repeating the spin coating process, allowing several hours of room temperature curing between

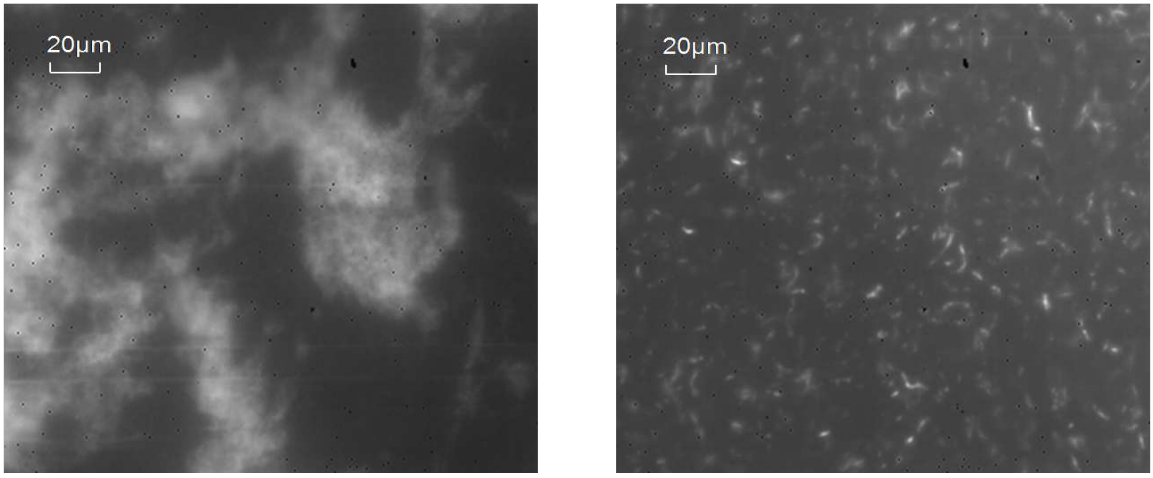

Figure 3.14 : Short-wave IR fluorescence microscopy images of smart skin films. The left frame shows unevenly dispersed SWCNTs (unsorted) in PMMA; the right frame shows well dispersed, randomly oriented SWCNTs (PFO-extracted) in urethane.

applications. Figure 3.14 shows SWIR fluorescence microscope images of S^4 films and illustrates the superior dispersion and individualization achieved using the PFO-based protocol described above. Industrial scale use of the S^4 method will of course need to rely on other application methods such as brush or spray coating (Figure 3.15).

3.6 Compact-Size Generation-II S^4 Probe

As shown in the schematic diagram of Figure 3.16, nanotubes in the S^4 film are excited with linearly polarized light from a 70 mW diode laser emitting at 660 nm. This wavelength provides near-resonant excitation for the (7,5) and (7,6) SWCNT structures, which are among those extracted by PFO. The laser beam is passed through a short-pass filter to remove any weak SWIR components, and through a half-wave retardation plate on a computer-controlled polar rotation mount to allow automated adjustment of its polarization plane. The excitation beam passes through a 2 mm

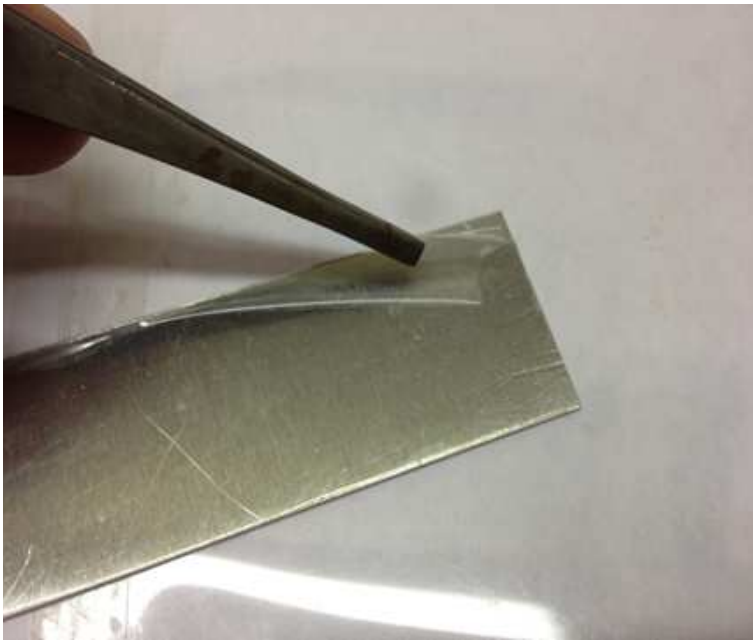

Figure 3.15 : Smart Skin on a steel slide.

hole in a coupling mirror and is focused onto the sample by an aspheric lens with a focal length of 11 mm.

Fluorescence from the S^4 film is captured and collimated by the same aspheric lens and reflected by the coupling mirror into a fiber collimator. This optical element focuses the fluorescence into the core of a multimode optical fiber ending at the entrance slit of a modular SWIR spectrometer (B&W Tek Sol 1.7). The spectrometer contains a thermoelectrically cooled 512 channel InGaAs detector array, allowing efficient measurement of the SWIR emission spectrum without spectral scanning.

As a step towards practical implementation of S^4 non-contact strain measurements, we have constructed a prototype portable reader that mounts all of the optics except for the SWIR spectrometer on a 4" $\times$ 6" hand-held platform (see Figure 3.17). Because the spectrometer is also relatively compact (ca. 8" $\times$ 4" $\times$ 3"), the read-out hardware may be connected to a notebook computer to provide an easily portable sys-

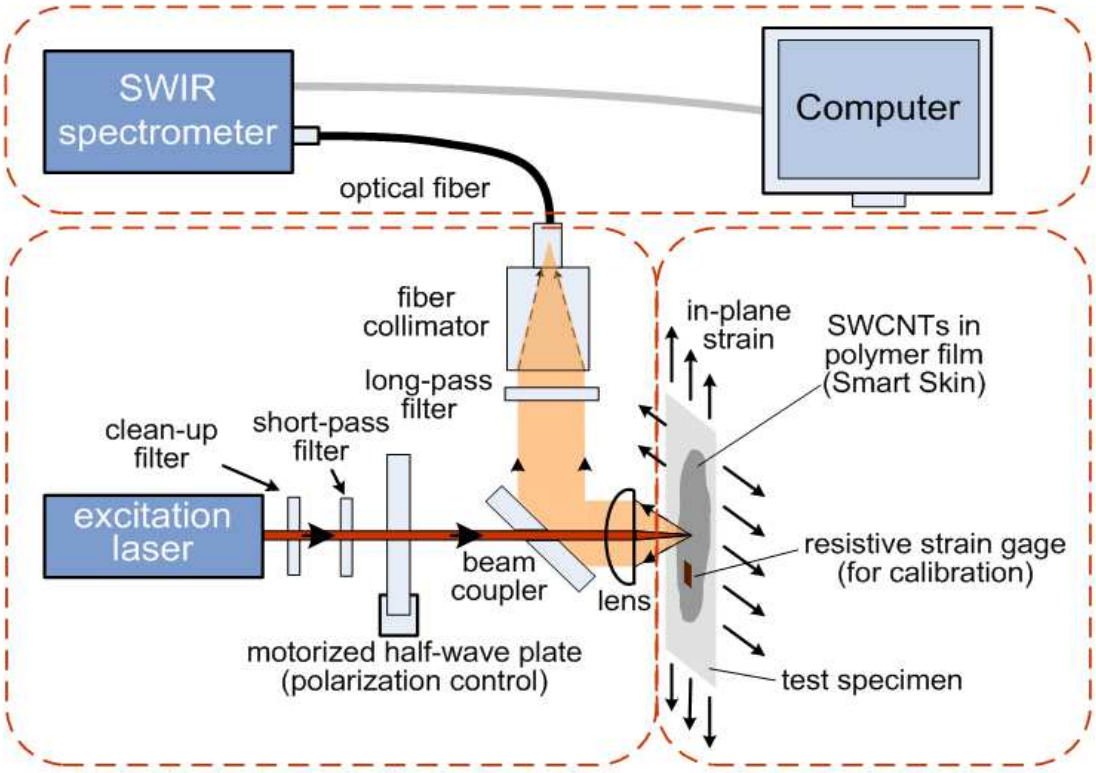

Figure 3.16 : Schematic diagram of Generation-II S^4 probe.

tem for non-contact strain measurement. To make calibrated S^4 performance tests on specimens with smart skin coatings, we affix a conventional resistive foil strain gage on top of the coating close to the optical measurement point. The strain on the substrate is independently monitored by another strain gage mounted at the corresponding location on the opposite surface of the PMMA specimen bar. Readings from the two strain gages are collected in real time to check the efficiency of strain transfer from substrate to polymer. We find that for S^4 films thinner than ca. 20 μm, the applied strain as measured on the opposite surface of the bar is nearly equal to the strain measured at the surface of the film. Hence, in the results section we report the readings from the strain gauge mounted on the substrate as calibration values to

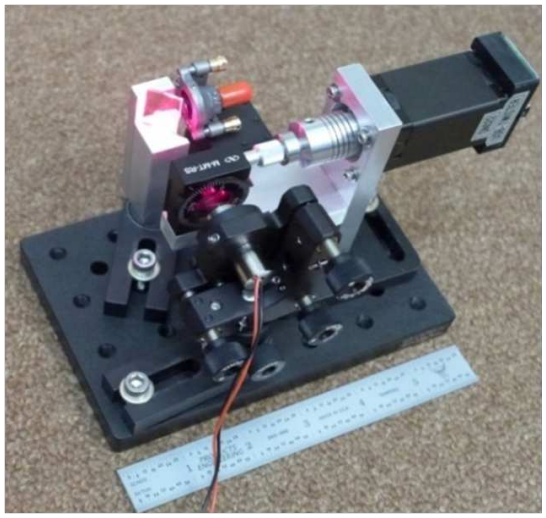

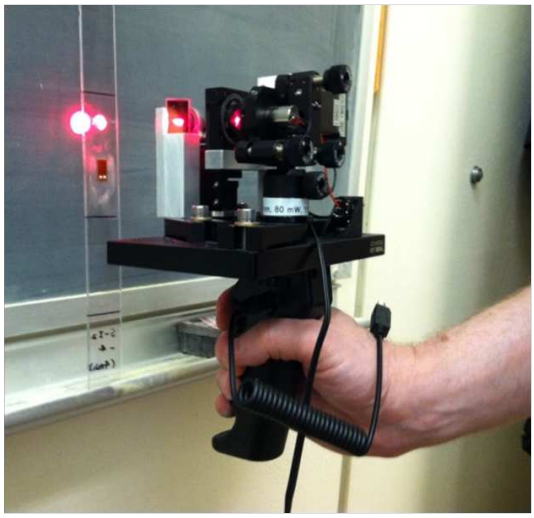

Figure 3.17 : (a) S^4 probe head on its 4" x 6" base (b) S^4 probe head with handle

compare with spectral data.

3.7 Experimental Results

3.7.1 Durability of S^4 Films under Longtime Laser Interrogating

When the interrogating laser is focused on one point for a certain period, heat can melt the polymer film and affect SWCNTs. In order to check the durability of the smart skin over time, we need to investigate how much damage the laser will cause to SWCNTs within the smart skin. Damage can be revealed by a drop of emission intensity as fluorescence is monitored over time.

Figure 3.18 shows the fluorescence of a slide for varying durations of laser exposure. We can see that after more than 2 hours exposure to laser excitation, the smart skin can still emit a very high intensity with only 10% reduction in the initial intensity. This implies that the smart skin can be exposed to laser excitation for a very long time without a serious decrease in signal strength. This ensures the capability in

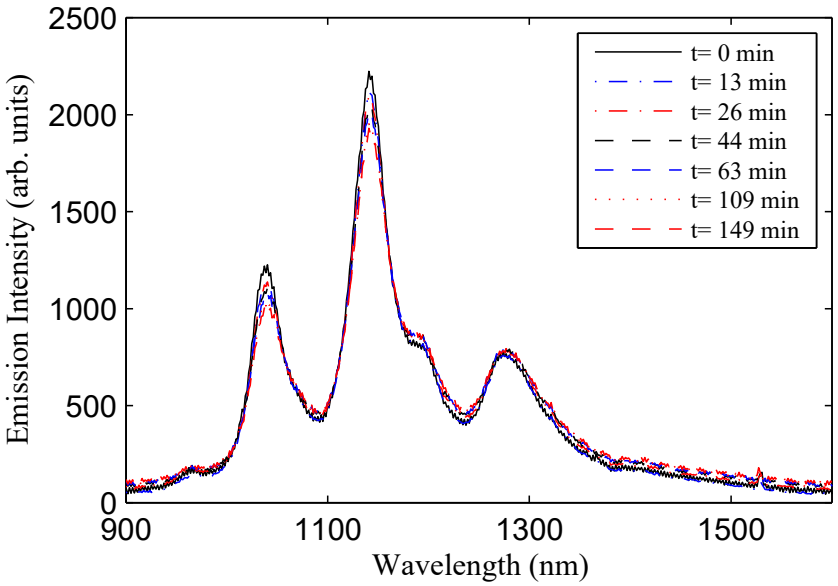

Figure 3.18 : Emission spectra of S^4 film under longtime laser exposure

monitoring strain for a longtime.

3.7.2 Mechanical Test 1

The peak positions of (7,5), (7,6), and (8,6) SWCNT fluorescence from S^4 films are found by separately fitting local Gaussian functions to the emission peaks near 1050 nm, 1140 nm and 1200 nm, as shown in Figure 3.19.

Resolution is one key factor defining the sensitivity of a sensor. Strain resolution is the smallest measurable change in strain, typically quoted in dimensionless units of millistrain ($m\varepsilon$) or microstrain ($\mu\varepsilon$). In our method, strain resolution is determined by the precision with which fluorescence peak wavelengths can be measured, which is in turn controlled by the spectral resolution of the spectrometer, the spectral width of the fluorescence peak, and the signal-to-noise ratio of the measured spectrum. Our spectrometer's resolution of 2 nm is significantly less than the width of the fluorescence

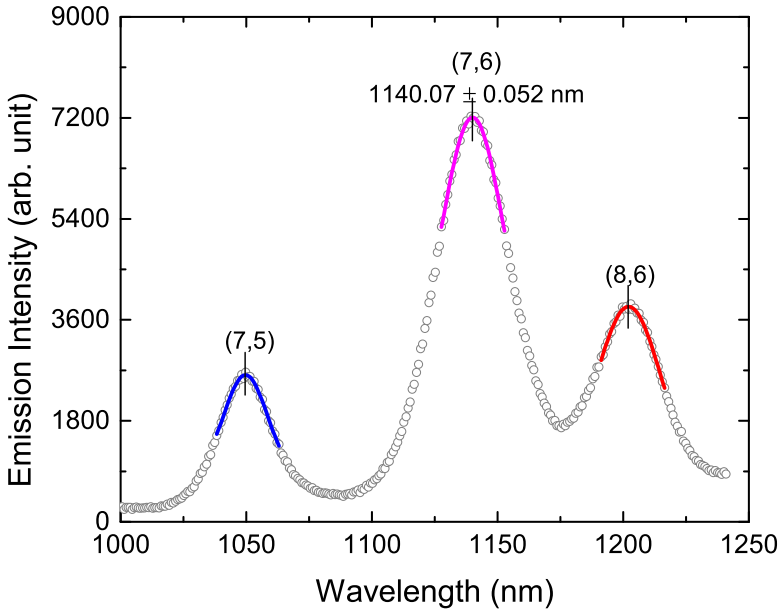

Figure 3.19 : Peak positions determined by curve fitting.

peak and spectral resolution. The signal-to-noise ratio depends on excitation laser intensity, SWCNT concentration in the film, SWCNT fluorescence quantum yield, optical collection efficiency, detector sensitivity and noise, data acquisition time, and data averaging. For the dominant (7,6) peak, we find that averaging 10 acquisitions of approximately 2 s from a typical S^4 film each allows us to determine the peak wavelength with a standard deviation of approximately 0.052 nm. Since the theoretically predicted (7,6) strain coefficient (the slope of its peak position vs. strain, $\partial\lambda(7,6)/\partial\epsilon$) is approximately 1.2 $nm/m\varepsilon$, this gives a standard deviation for the strain measurement of ca. 45 $\mu\varepsilon$. In practice, the stain uncertainty is somewhat larger than this because the effective strain coefficient for an ensemble of randomly oriented SWCNTs is smaller than that of a single aligned nanotube, and slippage effects can also reduce the coefficient. Strain resolution can be improved by combining peak position

measurements from different SWCNT structures, because the sign and magnitude of strain coefficients vary with (n,m). For example, we typically monitor the difference between the (7,5) and (7,6) peak positions, which has a predicted coefficient of 3.5 $nm/m\varepsilon$, or approximately three times that of (7,6) alone. Spatial resolution, or gage length, in the S^4 method is determined by the diameter of the excitation beam at the film surface. This dimension is normally ca. 0.1 mm, but it can be readily reduced to a few micrometers, if necessary. The gage length can be increased as needed by scanning the laser probe during spectral acquisition.

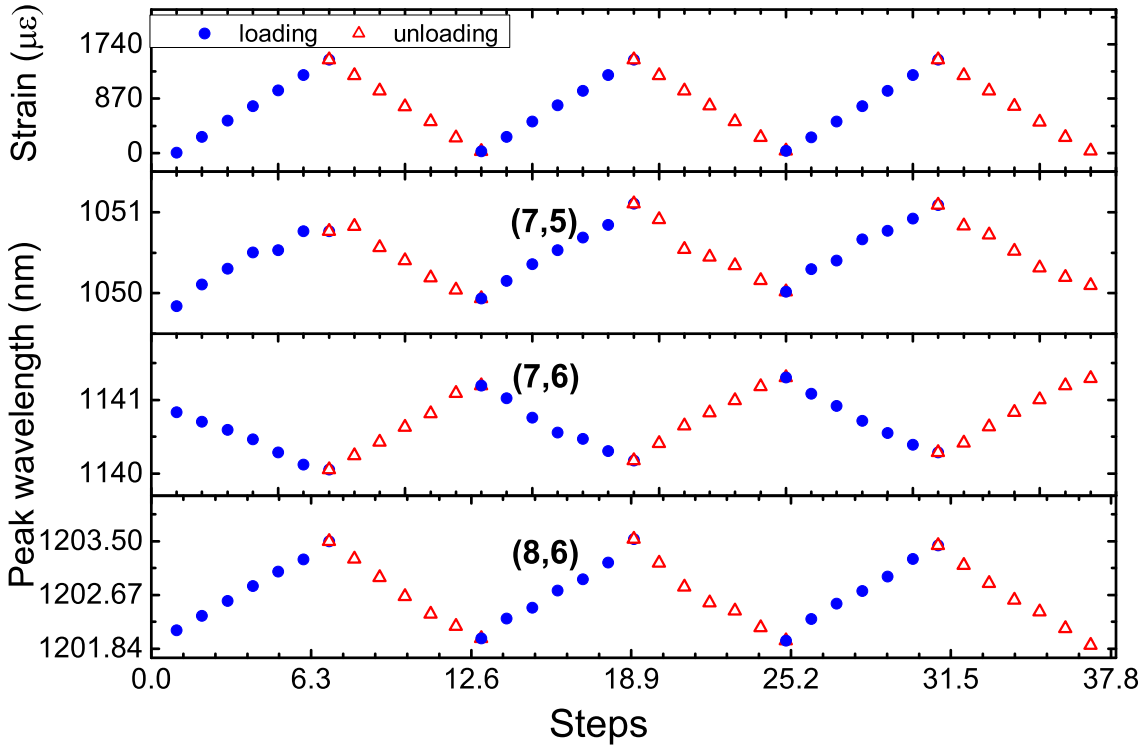

Figure 3.20 : Response of SWCNT peak positions to cyclic tensile strain in specimen

PMMA specimens coated with the SWCNT smart skin are subjected to tensile deformation using a custom built four-point bending jig over the strain range from 0

to 1500 $\mu\varepsilon$. Figure 3.20 shows the sequence of applied deformations and the resulting responses of the three spectral peak positions. The (7,5), (7,6), and (8,6) peaks shifted systematically with the applied strain, confirming efficient load transfer from the PMMA bar to the polymeric coating to the embedded SWCNTs.

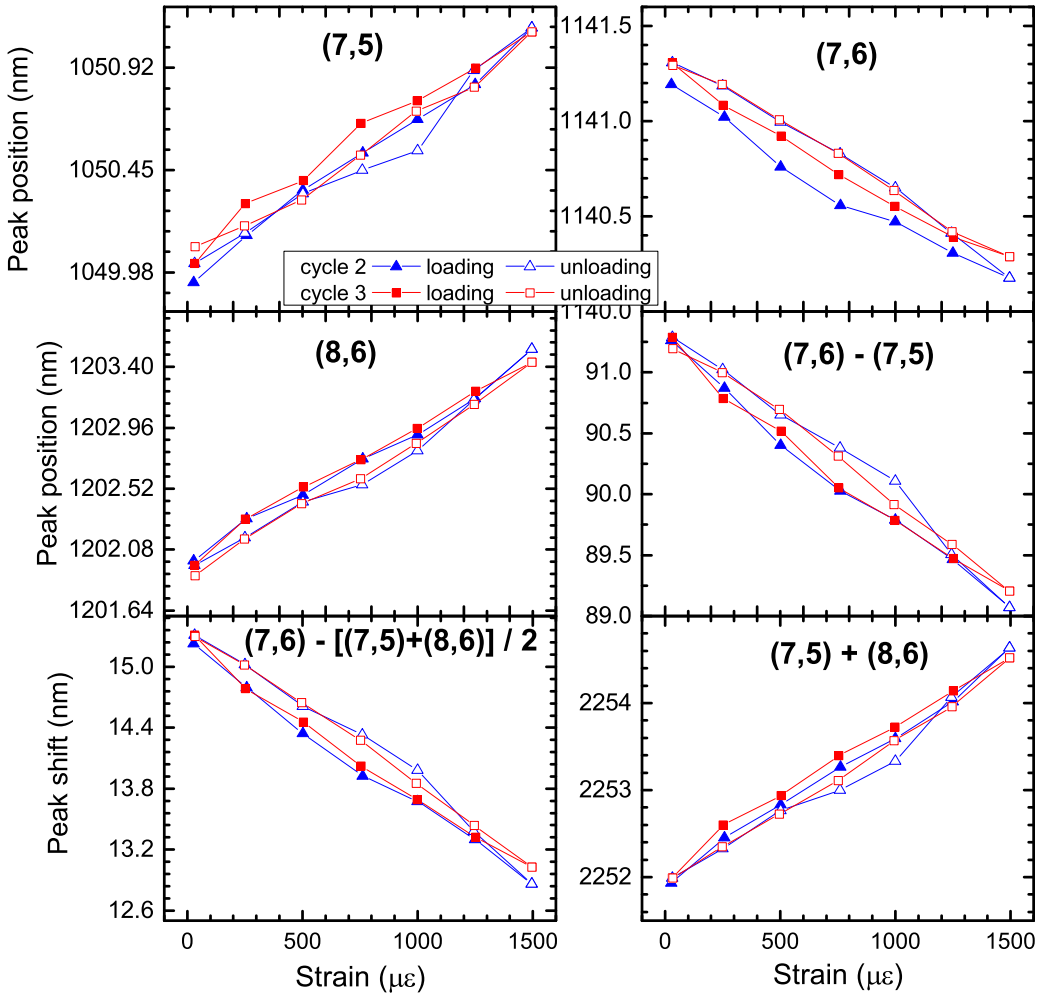

Figure 3.21 : SWCNT peak positions and shifts vs. tensile strain on specimen.

The spectral peak positions are shown as a function of tensile strain in Fig-

ure 3.21. In this figure, we have omitted data from the first cycle, which seems to show relaxation of initial nanotube strains caused by shrinkage forces as the S^4 film cured. The observed slopes of the three peak positions with strain are $\partial\lambda(7,5)/\partial\epsilon = 0.736\,nm/m\varepsilon$, $\partial\lambda(7,6)/\partial\epsilon = 0.712\,nm/m\varepsilon$, $\partial\lambda(8,6)/\partial\epsilon = 1.042\,nm/m\varepsilon$ respectively. The strain coefficient for the (7,5) - (7,6) peak separation for both loading and unloading curves is about 1.4 to 1.5 $nm/\mu\varepsilon$ ($14 \sim 15\,nm/\%$). This is less than the theoretical prediction because of the random distribution of SWCNT orientations in the film and some slippage of nanotubes in the polymer host arising from imperfect adhesion. As the sample undergoes deformation cycles with larger strains, up to 3000 $\mu\varepsilon$, the agreement between loading and unloading curves degrades, leading to a visible hysteresis loop (see Figure 3.23). We attribute this effect to molecular level damage in the smart skin at the nanotube-polymer interface. Further investigations on this subject are planned.

Figure 3.24 shows the response of the three peak positions of the SWCNTs within the smart skin due to the cyclic tensile deformation. We hypothesize that the initial deformation cycles allowed relaxation of initial strains in the nanotubes caused by forces exerted as the S^4 film shrank during curing. Following this relaxation process, our data suggest that the coating shows nearly elastic deformation behavior. The zero-strain peak positions for the remaining eight cycles agree closely, suggesting no further relaxation of residual strain. The downward drift of (8,6) peak position at 5000 $\mu\varepsilon$ within the first 5 loading-unloading cycles is likely due to the relaxation of initial strains and friction at the interface between the polymer and nanotube. However, the drift appears to stabilize after the fifth cycle. We are still optimizing the material preparation to minimize these effects.

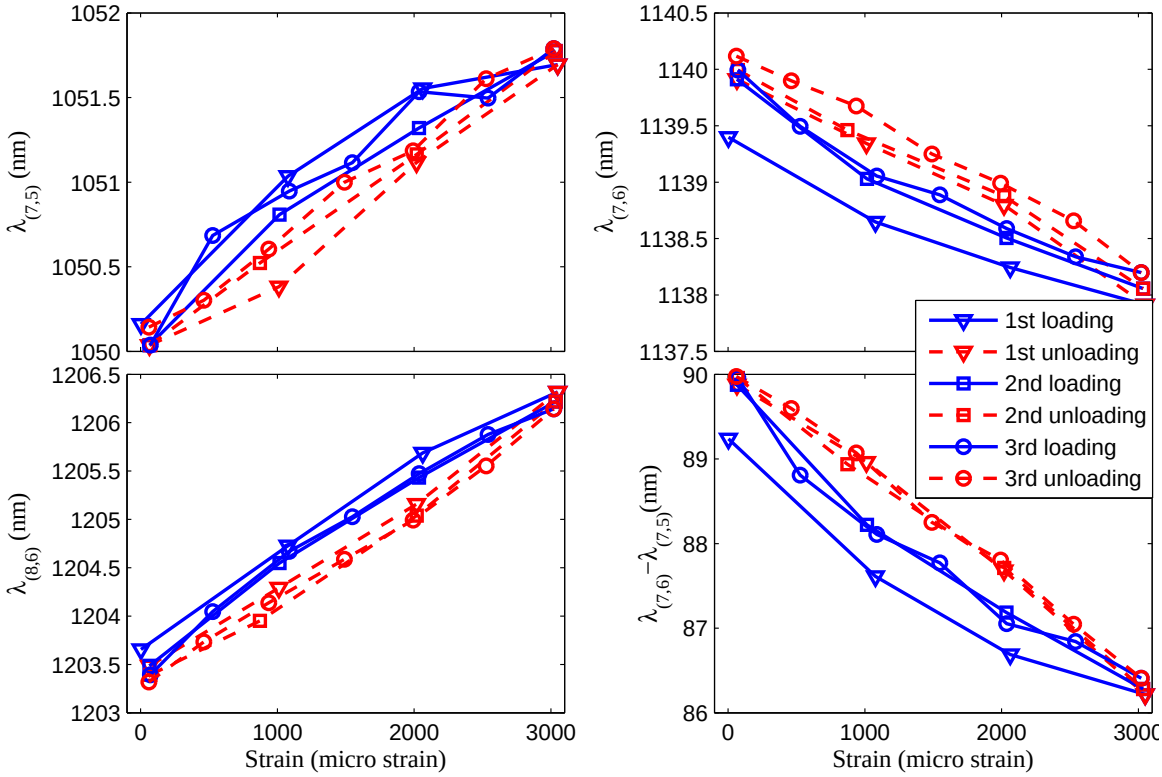

Figure 3.22 : Response of SWCNT peak positions to cyclic tensile strain from 0 to 3000 $\mu\varepsilon$ in specimen.

3.7.3 Mechanical Test 2

The Generation-II composite material described above was applied as a liquid to various test substrates and allowed to cure to give S^4 films approximately 10 to 20 μm thick. Spectra from SWCNTs in the film were then measured using the prototype readout apparatus while the specimen was subjected to controlled loading in tension. Actual induced strains were measured with conventional resistive foil gages for comparison with the observed changes in spectral peak positions. Figure 3.25 shows an example of the correlation found between spectral response of the S^4 film and the independently measured deformation of a PMMA test specimen that was strained

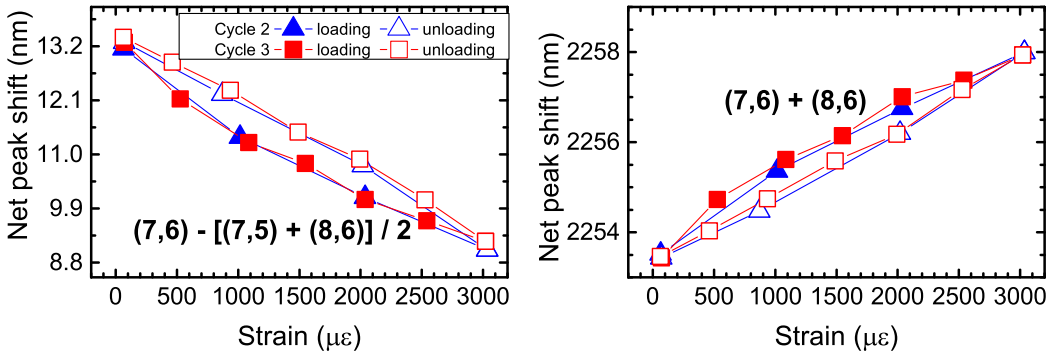

Figure 3.23 : Combinations of SWCNT peak positions vs. tensile strain on specimen. The spectral peaks used for each frame are listed. Data for the first cycle have been omitted for the same reason described in the text for Figure 3.21.

between 0 and 1000 $\mu\epsilon$ during two cycles of loading and unloading. The response is highly linear in this range, although at higher strains we observe deviations attributed to slippage of nanotubes in the host film. The upper limit to strains measureable by the S^4 method will be determined by the strength of interfacial adhesion between SWCNTs and the surrounding polymer.

As described above, the S^4 method can also determine the axis of strain. We illustrate this in Figure 3.26, which shows data measured for the spectral response (difference between the (7,6) and (7,5) peak wavelengths) at one point on a test specimen that was strained to different extents along a single axis. For each strain level there is a smooth and systematic variation of spectral response as a function of the polarization direction of the excitation laser beam. The maximum responses are clearly found at 0 degrees, which is the actual strain axis. It is clear then that the S^4 method can determine directions as well as magnitudes of substrate strains.

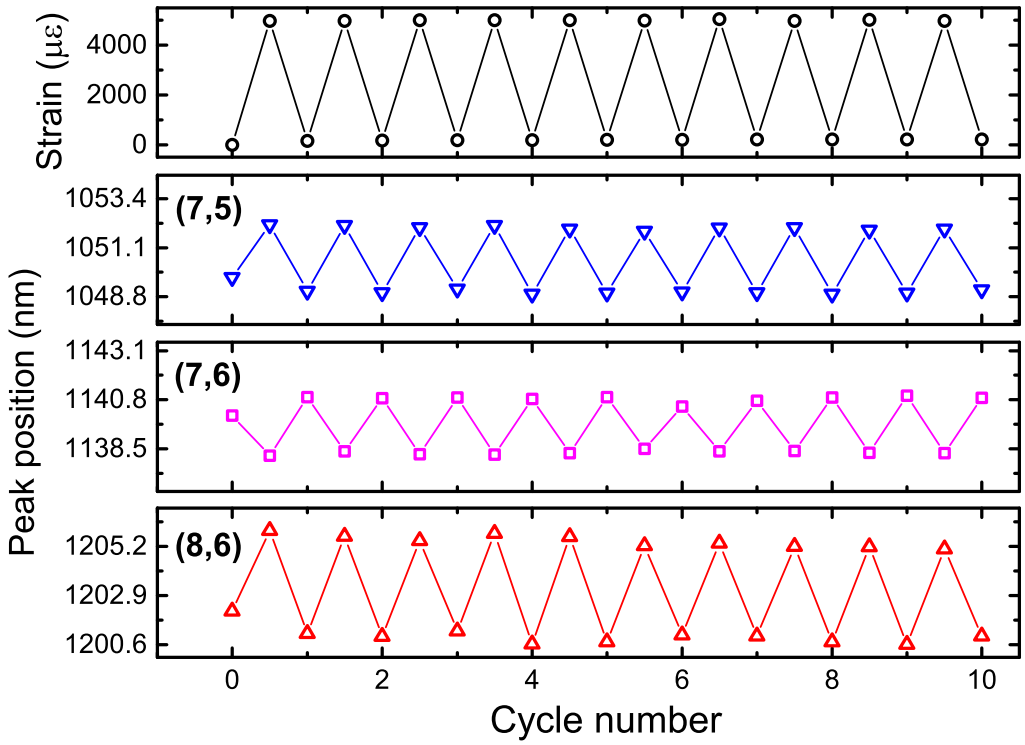

Figure 3.24 : Response of SWCNT peak positions to cyclic tensile strain from 0 to 5000 $\mu\varepsilon$ in specimen.

3.8 Concluding Remarks

In this study, we demonstrate progress toward the practical implementation of non-contact optical strain measurement using carbon nanotubes in polymeric films as sensors. Generation-II S^4 solution is designed using PFO-extracted SWCNTs and urethane. PFO is used to purify and select out certain species of SWCNTs of interest. In this processing, the nanotubes are individually dispersed, a small number of structural forms are preferentially retained, and many impurities are removed. Af-

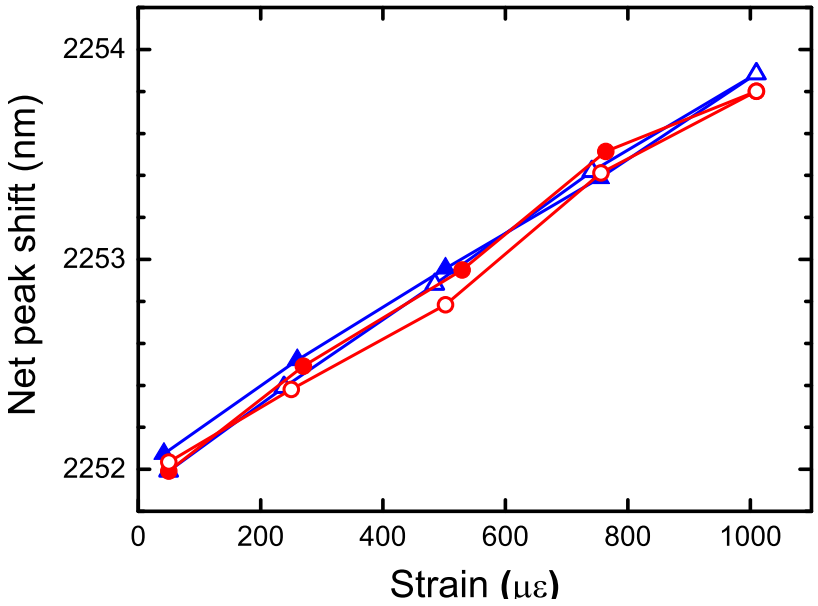

Figure 3.25 : Measured spectroscopic peak shift parameter ((7,5) + (8,6)) from a Generation-II S^4 film vs. independently measured strain in the PMMA substrate. Data are shown for two loading/unloading cycles.

ter mixing with the urethane, application to test surfaces, and curing, we observed strong and distinct SWCNT fluorescence signatures from the S^4 films. The fluorescence spectra are captured with a novel optical system that is compact and light enough to permit field use. The achieved optical data precision corresponds to strain resolutions in the range of 10 to 100 $\mu\varepsilon$. Test specimens have been subjected to cyclic deformations from 0 up to 5000 $\mu\varepsilon$ while recording spectral shifts from the S^4 films and readings from conventional strain gages. The results show promising repeatability for the S^4 method, although effects from imperfect interfacial adhesion between polymer film and SWCNTs can be seen, especially at higher strains. We anticipate that the fidelity of these optical strain measurements will improve as further refinements are made to improve the properties of the S^4 composite films.

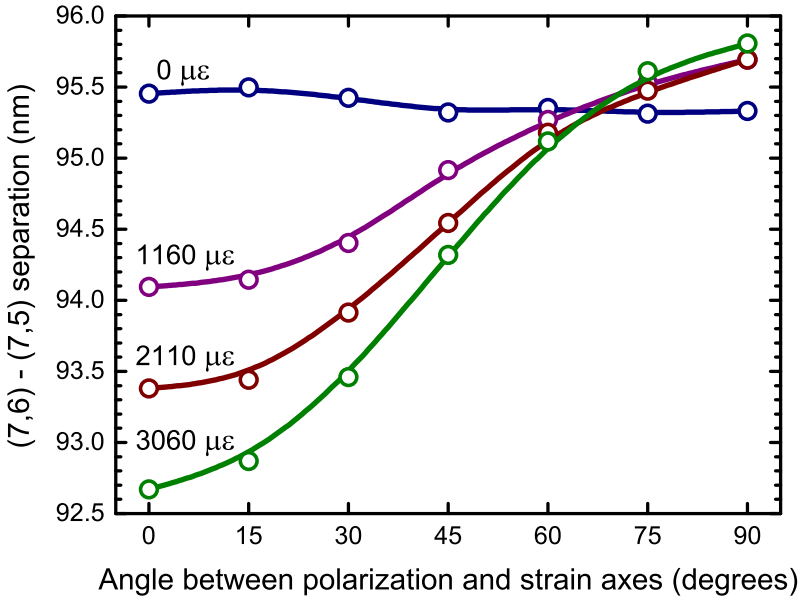

Figure 3.26 : Points show the (7,6) - (7,5) peak separation from an S^4 film as a function of excitation beam polarization direction. Tension is applied to the test substrate along the zero-degree direction to give the three different labeled strains. Solid curves are best fits to cos^2 functions with adjusted amplitudes.

Chapter 4

Development of Generation-III S^4 Films

4.1 Introduction

As described in Chapter 2, the prototype S^4 film is prepared by dispersing raw SWCNTs into commercial urethane varnish. Although these Generation-I S^4 films showed promising results for strain sensing, their fluorescence spectra are congested from the presence of emission peaks from numerous (n,m) species and the intensity is greatly hindered by other waste materials, such as carbon ropes and bundles. Furthermore, the impurity and large concentration of nanotubes within Generation-I smart skin during the film fabrication can easily make the concentration and orientational distribution of nanotubes nonuniform in the respect of space, for example, clustering of nanotubes can occur in some spot while less dense nanotubes in other places. Because the thorough dispersion of nanotubes within high viscous urethane varnish is never easy and the reaggregation of nanotubes within liquid state of varnish occurs all the time even after quick film deposition. These will further cause nonuniformity of fluorescence features, such as emission intensity and wavelength in space. This hampers the extraction of precise peak positions and interpretation of correct strain state. In order to avoid this problem, Generation-II S^4 films were developed in Chapter 3. In the films, PFO is used to preprocess the SWCNTs to provide structural sorting and purification. [46] As shown in Figure 4.1a and Figure 4.1b, such Generation-II S^4 films display more structured fluorescence spectra, allowing precise measurements of

several (n,m) peak positions and the use of combined peak shifts for improved strain determinations. [47]

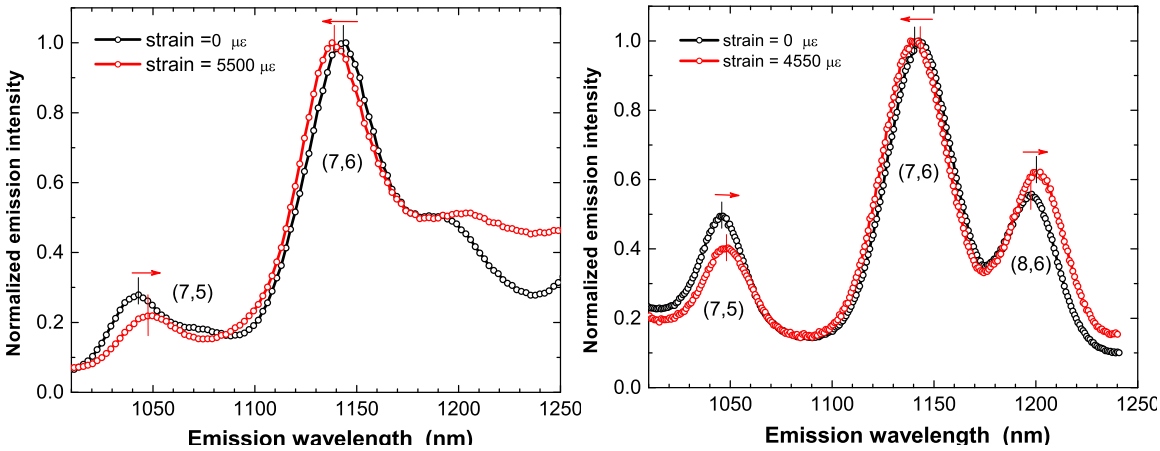

(a) Generation-I (b) Generation-II

Figure 4.1 : Strain-induced changes in emission spectra for Generation-I S^4 film (left panel) and Generation-II S^4 film (right panel). The excitation wavelength is 660 nm.

The two goals mentioned Chapter 3 have been achieved by Sun et. al. [46]: one is tailoring the SWCNT composition and dispersion in the composite film with the adoption of PFO treatment on SWCNTs; the other is developing compact-size instrumentation which can efficiently generate, capture, and interpret fluorescence spectra from the S^4 film. However, during preparation and evaluation Generation-II "S^4" films, we discovered that some issues of the sensing film still remain unsolved, especially quenching of intensity of fluorescence due to chemical reaction between carbon nanotubes and polymer. [47] More efforts to make "S^4" films towards a more practical full-field, non-contact strain sensing technique will be described in this Chapter.

4.2 Quenching Interactions

Practical implementation requires the capture of high quality emission spectra to allow precise determination of small strain-induced changes in peak positions. In addition, these spectra must be acquired quickly to enable the preparation in reasonable amounts of time of strain maps derived from measurements at many locations on a surface. These constraints imply the need for spectra with high signal-to-noise ratios, so optimization of fluorescence signal strengths is important.

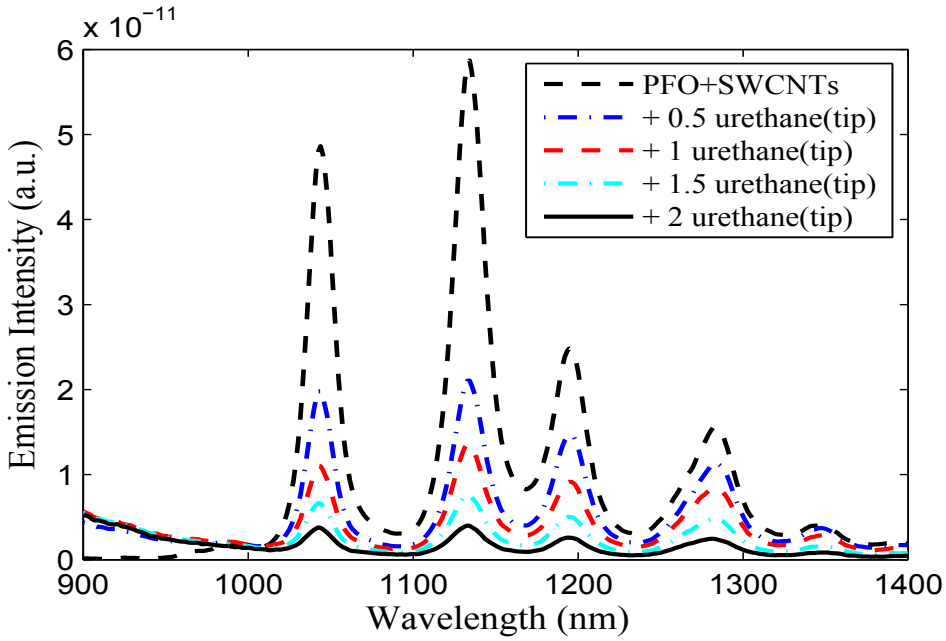

Figure 4.2 : Emission spectra of PFO-SWCNTs mixed with spar urethane by tip sonication. The data have been scaled to compensate for the effects of dilution.

During the fabrication of Generation-II S^4 nanocomposite suspension, one important step is adding PFO-extracted SWCNTs into polymeric matrix (Minwax Spar Urethane) as described in Chapter 3. Theoretically, if there are no chemical reactions between SWCNTs and the polymers in the mixture (PFO and urethane), the fluo-

rescence intensity (normalized by SWCNTs concentration) would remain the same after the step. However, by tracking the fluorescence of the SCWCNTs within the suspension before and after the process step, we find the fluorescence decrease dramatically after the step of process. The SWCNT emission intensity is substantially reduced by quenching interactions between SWCNTs and the urethane host material. To investigate this quenching effect, we have measured emission spectra of a standard preparation of PFO-extracted SWCNTs after mixing with different amounts of the commercial spar urethane varnish.

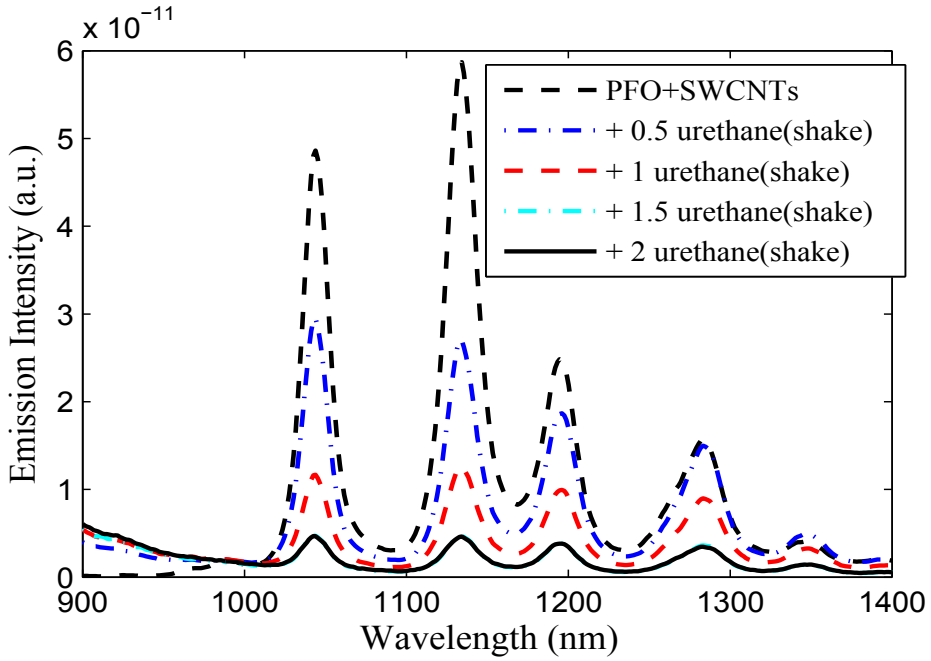

Figure 4.3 : Emission spectra of PFO-SWCNTs mixed with spar urethane by shaking. The data have been scaled to compensate for the effects of dilution.

As shown in Figure 4.2, the emission intensity of SWCNT peaks decreases monotonically and dramatically after 1 volume of SWCNT suspension is added to 0.5, 1, 1.5, or 2 volumes of urethane and mixed by 2 min of tip ultrasonication. Note that

these spectra have been scaled to account for volumetric dilution, so the decreases indicate a strong reduction in the nanotubes fluorescence quantum yield. To determine whether this effect might result from SWCNT damage in the ultrasonication process, we prepared equivalent mixtures with the varnish in which manual shaking is applied instead of tip ultrasonication. The results, plotted in Figure 4.3, show fluorescence quenching that is nearly as severe. Table 4.1 lists the normalized fluorescence intensities measured at four different (n,m) emission peaks after mixing with four different varnishes. It is found that all of the varnish compositions cause emission quenching by at least 83%, with the smaller diameter nanotubes most strongly affected. This is consistent with a chemical interaction mechanism that is facilitated by the higher reactivity of small diameter SWCNTs caused by curvature bond strain. We conclude that different polymeric host materials or new film structures should be explored to optimize the optical efficiency of S^4 coatings.

Driven by the issues discovered, we need to design a new S^4 in order to: 1) further enhance fluorescence intensity of the S^4 films to reduce the measuring time (integration time for spectrometer); 2) make S^4 films robust to harsh weather, including UV damage; 3) make S^4 films have uniform features in space (film thickness, SWCNTs concentration, SWCNTs orientational distribution) to ensure a better (reference free) full-field strain measurement; 4) adopt an easier film-application method (hard to perform air brush coating for Generation-II S^4 films). These issues will be discussed and addressed in the coming sections. We will improve the properties of S^4 film as a better strain sensing network by tailoring the film structure and film-fabrication protocol.

Table 4.1 : Ratios of emission intensities from liquid suspensions of SWCNTs in PFO/toluene mixed with polymeric varnishes in 1:2 volume ratios, relative to emission intensities before mixing with varnish. Values are corrected for volumetric dilutions. Tip and shake denote mixing by tip ultrasonication and mechanical shaking, respectively.

Commercial varnish	Main components	Final / initial emission intensity (7,5)	(7,6)	(8,6)	(8,7)
Minwax Spar urethane (tip)	aliphatic hydrocarbon solvent, urethane	7.8%	6.8%	10.4%	15.7%
Minwax Spar urethane (shake)	aliphatic hydrocarbon solvent, urethane	9.6%	7.9%	15.4%	22.2%
Minwax Fast-dying polyurethane (shake)	aliphatic hydrocarbon solvent, polyurethane	4.9%	4.7%	8.6%	9.5%
Epifanes Clear High Gloss Varnish (shake)	resins, tung oil, petroleum naphta	7.1%	6.5%	11.4%	16.1%
Duralux Marine Spar Varnish (shake)	resin, mineral spirits (aliphatic and aromatic solvents)	4.3%	4.2%	6.6%	7.5%

4.3 Design of Generation-III S^4 Films

As described in Section 4.1 and Section 4.2, the issues including the reaction between SWCNTs and various polymeric host (such as urethane, polyurethane and mineral spirits) in Generation-II S^4 films quench the fluorescence a lot. Till now, we haven't found a non-reactive polymeric host which can mix well with and be compatible with PFO-SWCNTs-toluene suspension. Hence, we have to address the issue by changing the film structure of Generation-II S^4 films. Instead of mixing the PFO-SWCNTs-

toluene suspension with reactive polymeric host in a layer structure as a whole, we want to prevent or minimize the contact of PFO-SWCNTs-toluene suspension with reactive polymeric varnish, so that the reaction between SWCNTs and reactive polymer can be prevented.

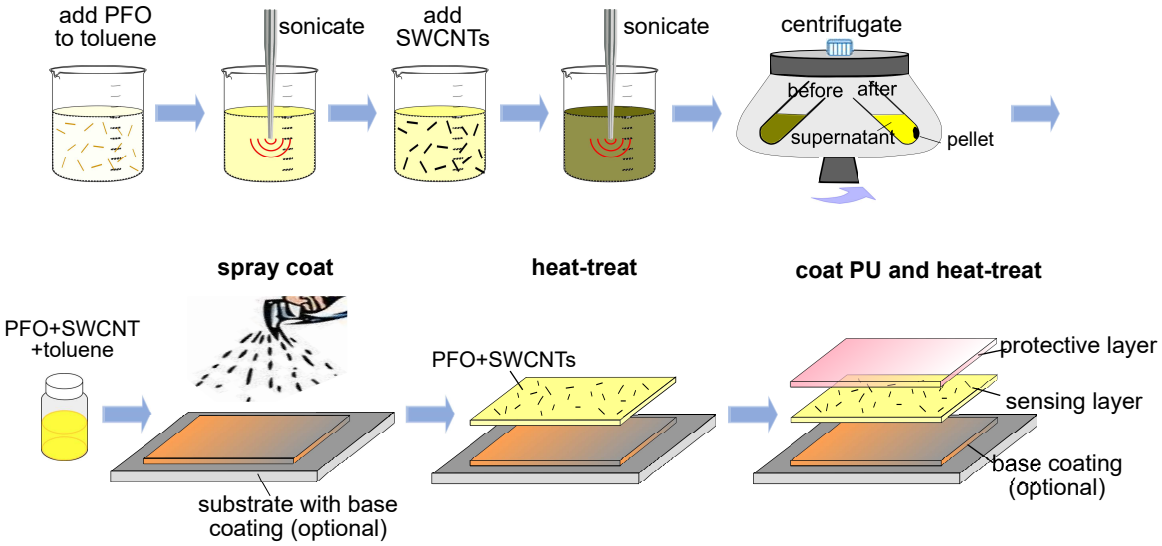

Figure 4.4 : Protocol for preparing S^4 films with layer-layer structure.

In the preparation of the Generation-I S^4 film [39, 40] solution as shown in Figure 2.5, raw HiPco SWCNTs which are not purified are mixed with a consumer-grade exterior urethane varnish and dispersed by ultrasonic agitation. Although the Generation-I S^4 films shows promising results for strain sensing [39], their fluorescence spectra are congested and broadened by the presence of emission peaks from numerous (n,m) species, which hampers the extraction of precise peak positions and shifts. In the Generation-II S^4 films (Figure 3.16), we use PFO to pre-process and purify raw carbon nanotubes by selective extracting (7,5),(7,6),(8,6) and (8,7) SWCNTs. [46] These processed samples are mainly individual SWCNTs wrapped around by PFO that is solubilized in toluene and these samples are mixed in urethane by

tip sonication. Although the Generation-II S^4 film has a simpler and clearer fluorescence spectra, allowing more precise measurements of several (n,m) peak positions, the emission intensity is quenched dramatically by more than 80% when mixing PFO extracted SWCNTs and urethane. We suspect that strong chemical interaction occurs between PFO, SWCNTs and urethane damaging the SWCNTs electronic structures in large amount. [47] The quenching in fluorescence emission results in lower signal-to-noise ratios and makes data collection time longer to ensure the same accuracy of measurement. To find a chemically insensitive polymeric host to PFO extracted SWCNTs, that does not quench the emission intensity, we monitored emission spectra of a standard preparation of PFO-extracted SWCNTs after mixing with several different commercial varnishes. Unfortunately, all the SWCNTs emission intensities are quenched and decrease dramatically by an order of magnitude. [47] In the present study on Generation-III S^4 film, we solve the issue by designing a new film structure to optimize the optical efficiency of S^4 coatings. We propose a layer-by-layer structure for the S^4 film and use heat treatment to optimize the characteristics of the films.

4.3.1 PFO-SWCNTs Sensing Layer

In preparation of Generation-II S^4 films, we find that the refreshment of PFO-extracted SWCNTs sample is required before mixing or application, because after being placed at one place for certain time, the diluted SWCNTs in PFO-toluene would aggregate lowering the emission intensity. After tip sonication treatment refreshment of the sample, the emission intensity would be regathered to an acceptable level as shown in Figure 4.5.

We firstly brush coat PFO-SWCNTs-toluene suspension (centrifugated) on to an aluminum slide and then track emission spectrum change at liquid and solid state. As

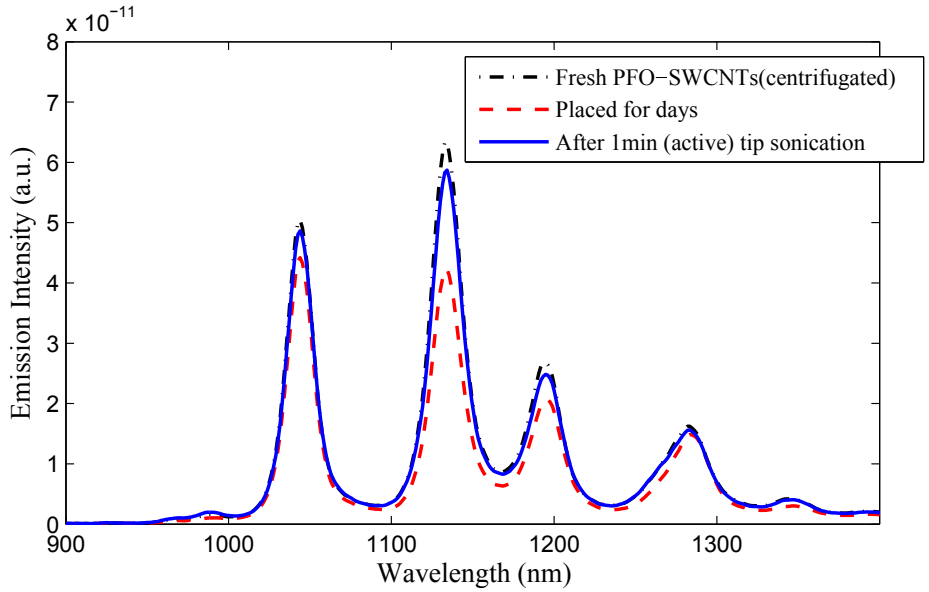

Figure 4.5 : Emission spectrum of PFO-SWCNTs-toluene suspension (black dot-and-dashed line) right after centrifugation, (red dashed line) placed for days and (blue solid line) refreshed by tip sonication (all measured using 642 nm laser, 100 ms integration, 20 frames averaged).

shown in Figure 4.6, the wavelengths of the peaks increase after curing and the peaks become wider due to the aggregation of SWCNTs during drying. Peaks at (8,6) and (8,7) become less dominant and flat, making the later curve fitting at those positions harder and less accurate.

However, compared to the Generation-II S^4 film formed by using urethane and PFO-SWCNTs-toluene mixture, the emission spectrum within PFO-SWCNTs films shows a clearer, stronger and shaper peak features. From the point of view of emission intensity and clear peak features in spectrum, the PFO-SWCNTs film could be a better film type for the next generation S^4 sensors.

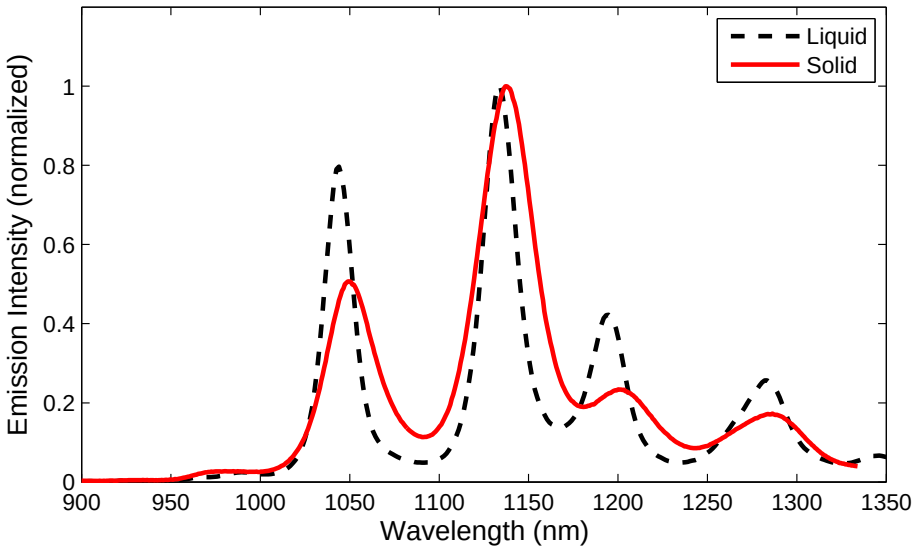

Figure 4.6 : Emission spectrum of PFO-SWCNTs-toluene liquid (@642 nm excitation) and of solid PFO-SWCNTs-toluene film (@660nm exciation); all the peaks shift to the right side after curing.

4.3.2 Heat Treatment on Sensing Layer

The annealing of plastics can be defined as a secondary process wherein the plastic is brought to a certain temperature, kept there for a time, and then cooled to room temperature. The primary reasons for annealing include the reduction or removal or residual stresses and strains, dimensional stabilization, reduction or elimination of defects, and improvement of physical properties. Homogeneous properties inside S^4 film, which includes film thickness, SWCNTs concentration and SWCNTs orientational distribution, are needed for future full-field strain sensing. However, as discovered, the standard deviation of the original strain is between 440 $\mu\varepsilon$ and 650 $\mu\varepsilon$ in the PFO-SWCNTs film after curing at room temperature. The uneven original strain condition within the film should be relaxed and a more homogeneous strain

condition should be made before the later application as a full-field strain sensor. It is assumed that hot temperature below the melting temperature (T_m) and above the glass-transition temperature ($T_g = 75\ ^\circ C$ [48]) of PFO can make PFO polymer softer and make nanotubes relax within PFO without causing too much possible damage. Within the designed range of the temperature, PFO is in a molten or rubber-like state, where carbon nanotubes which is comparative hard can relax their interaction with soft PFO. The treatment within T_g and T_m might lower the strain concentration at some spots and further make strain distribution within newly made smart skin smoother.

To validate the assumption, a 2D scanning is performed on a PFO coated aluminum specimen on a 4 mm x 30 mm rectangular area with a grid of 5 x 31. In total, the emission spectra at 155 spots on the grid are collected for a statistical study.

Figure 4.7 shows the statistical evaluation of the wavelengths at the peaks in spectra collected at 155 spots on PFO-SWCNTs film spray-coated on an aluminum slide treated after different temperatures. The standard deviation (std) in the wavelength at (7,6)-(7,5) separation is 0.88 nm. The sensitivities of Generation-I and Generation-II S^4 vary from 1.4 $nm/\mu\epsilon$ to 2.0 $nm/\mu\epsilon$. It implies that the standard deviation of the original strain is as much as 440 $\mu\epsilon$ in the PFO-SWCNTs film. We need to relax the original strain conditions within the film and make a homogeneous strain distribution before later strain sensing measurements. We assumed that hot temperature below the melting point of PFO can make PFO polymer softer and make nanotubes relax within PFO without causing too much possible damage.

Table 4.2 shows the statistics of wavelengths at peaks due to heat-treatment at various temperatures. The heat treatment of the film is performed on a heating plate within an enclosed container (providing enclosed heat environment) for 1 hour. The

Table 4.2 : Statistics of wavelengths at peaks due to heat-treatment at various temperature (unit: nm).

Temperature (^oC)		(7,5)	(7,6)	(8,6)	(8,7)	(7,6)-(7,5)
25	mean	1050.41	1139.26	1182.16*	1282.16	88.86
	std	0.71	0.26	130.18*	0.43	**0.82**
85	mean	1047.81	1139.52	1194.87	1285.36	91.71
	std	0.43	0.24	0.44	0.44	0.42
100	mean	1047.06	1140.34	1194.47	1288.27	93.28
	std	0.34	0.17	0.28	0.33	0.32
105	mean	1046.7	1140.48	1193.98	1288.44	93.78
	std	0.38	0.17	0.29	0.32	0.39
110	mean	1047.43	1140.51	1194.94	1288.45	93.08
	std	0.34	0.21	0.24	0.31	0.37
115	mean	1047.71	1140.93	1195.1	1289.26	93.22
	std	0.29	0.18	0.16	0.33	0.28
125	mean	1049.24	1142.09	1197.51	1292.39	92.85
	std	0.22	0.17	0.12	0.23	**0.17**

spectra are measured after the temperature on film cools down to room temperature 25 $^\circ C$ gradually. The heating temperature listed in the table are actual temperature measured by a non-contact IR infrared thermometer. As shown in Figure 4.7, the standard deviation drops gradually from 0.82 nm to 0.17 nm after the heat treatment temperature increase from 85 $^\circ C$ to 125 $^\circ C$. The standard deviation in the original strain condition (with no external strain added) from around 500 $\mu\epsilon$ to around 100 $\mu\epsilon$, making S^4 better in full-field strain sensing.

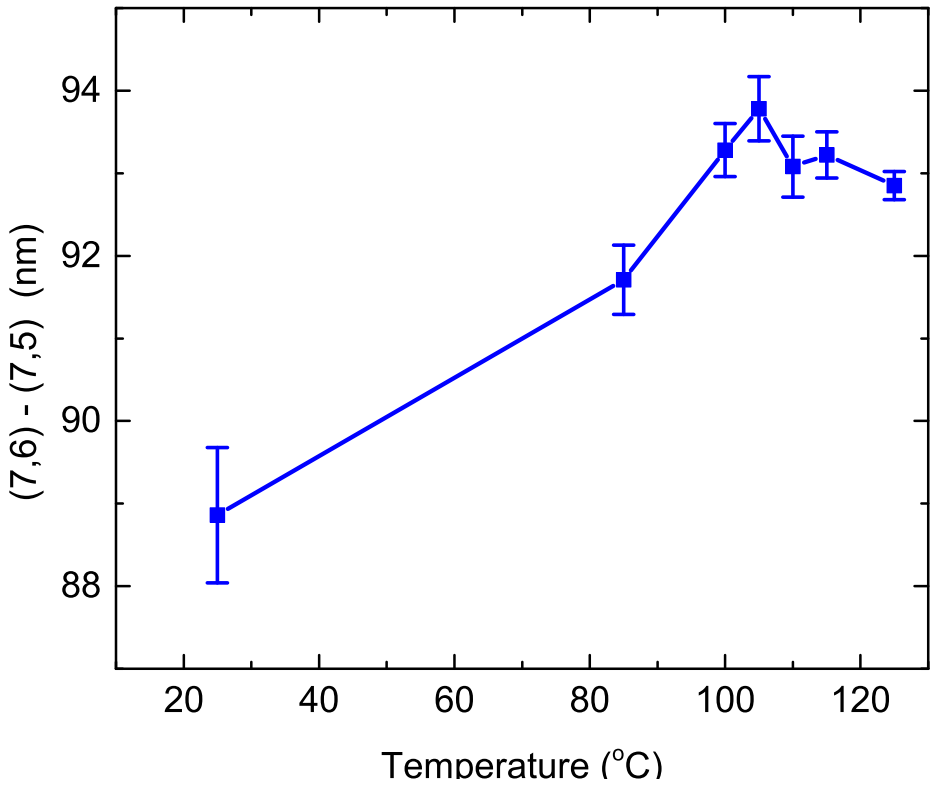

Figure 4.7 : Peak separation of (7,6)-(7,5) change due to heat treatment at various temperature.

4.3.3 Layer-by-Layer "Sandwich" Structure for S^4 Films

Although the Generation-II S^4 films outperform the Generation-I S^4 films by emitting a clearer spectra that can be analyzed more precisely, quenching interactions between the polymer host and SWCNTs reduce SWCNT emission intensity by an order of magnitude. Severe quenching interaction between raw SWCNTs and urethane exists even in the Generation-I S^4 film formulation as well. Failure in finding a non-reactive polymer host to embed SWCNTs led us to think in the direction of separating the PFO-extracted SWCNTs from the polymer host. Hence, we fabricate PFO processed SWCNTs (PFO and processed SWCNTs) directly as the strain sensing layer (shown

in Figure 4.4) which is a single-layered SWCNT-polymer skin embedded onto the metallic surface and the emission intensity is restored (shown in Figure 4.6). To protect the single sensing PFO-SWCNTs layer from harsh environment that a real structure is exposed to, a protective polyurethane layer is coated which is independent of the PFO-SWCNTs layer.

Because PFO-SWCNTs-toluene solution has a relative low viscosity compared to our Generation-I and Generation-II S^4 film solution, the suspension can be sprayed on a substrate to form a very thin film with a thickness of less than 0.4 μm. Because the sensing layer is very thin, the error caused when strain is transferred from structure to sensor is negligible. Compared to the spin coating and brush coating which were adopted in the Generation-II S^4 films, spray coating has a big advantage in the sense of scalability. The maintenance of spray tool would be much easier if using low viscous PFO-SWCNTs-toluene solution rather than using highly viscous polymer-SWCNTs solution that is widely used in industry. The quick evaporation of toluene enables the curing time of the PFO-SWCNTs fast. These characteristics of PFO-SWCNTs-toluene solution permit spray-coating on large structural surfaces such as civil infrastructures, mechanical systems and aerospace structures.

Firstly PFO-SWCNTs-toluene suspension is coated on to an aluminum slide and then emission spectrum change is tracked at liquid and solid state. The wavelengths of the peaks increase after curing and the peaks become wider due to the aggregation of SWCNTs during drying. Peaks at (8,6) and (8,7) become less dominant, making the curve fitting at these positions less accurate. Compared to the previously developed Generation-I and II types of S^4 films, the emission spectrum of PFO-SWCNTs films shows a much clearer, stronger and sharper peak feature. Using the same brush coating, the thickness of the films is more than 20 μm for the Generation-I raw Hipco

SWCNTs and urethane film, 10 μm for PFO-extracted SWCNTs and urethane film and about 0.4 μm for PFO-SWCNTs sensing film because of the different viscosity of the solutions. The mechanical strain transferred from structure to coating decreases from the bottom surface to the top surface of the films, so given all other conditions being same, the thinner a polymer coating is, the more efficient the strain transfers from coating to S^4 film sensor. Hence, in the characterization of our S^4 film, we usually prefer a thinner smart skin with stronger fluorescence emission. Among the three type S^4 film sensors, the PFO-SWCNTs sensing film outperforms the other two, emitting the clearest fluorescence spectrum. With a larger emission intensity and clearer spectra, the PFO-SWCNTs sensing layer is the most important component in the proposed layer-by-layer S^4 film structure. The load/strain transfer is ensured with the proposed sensing layer of PFO and SWCNTs, which is demonstrated as a practical idea by the results of the study which will be presented in the following sections.

Outdoor structural surfaces are usually exposed to harsh weather conditions. In addition, the sensing layer needs to be protected from other chemical exposure such as oxidation, UV light, acid rain and sea air, so a dense and protective overcoat layer needs to be designed to block these chemical invasions. In this study, AkzoNobel Polyurethane Topcoat (a commercial polyurethane that is widely used in aerospace industry for painting aircraft surfaces) is used as a protective coat for the layer-by-layer assembly of the new S^4 film. Compared to other commercial urethane or polyurethane products, the AkzoNobel polyurethane is optically transparent containing no color pigments, which allows laser to pass through without much decay. In the emitted fluorescence spectrum, considerable background caused by polyurethane is not observed. Adding proper amount of a commercial thinner solvent, the AkzoNobel®

polyurethane can be conveniently sprayed on structural surfaces (as currently done in aircraft).

For the fabrication of the new S^4 films, a layer-by-layer sandwich film-sensor structure is proposed which consists of three stacked layers from bottom to top(see Figure 4.4): a base coating layer (usually a very thin anti-corrosion coating) as commonly seen in aerospace industry (optional; not considered in this study), a strain-sensing layer of PFO processed SWCNT layer and a protective polyurethane layer. Comparing the spectra on sensing layer before and after applying an additionally protective polyurethane layer (see Figure 4.9), it is found that the emission intensity on the sensing layer remains almost the same. The application of the protective PU layer doesn't hinder the emission fluorescence. It shows the layer-by-layer sandwich structure is very promising in development of an S^4 film with a superior optical efficiency.

The wavelength at peaks shift after the curing of the protective layer, indicating the change in the strain conditions of embedded SWCNTs in the second layer. (7,6)-(7,5) peak separation changes from 85.04 nm to 95.37 nm consistently throughout the space, implying a 0.6% compressive strain. The spectral shift (causing compressive strain) observed might be due to the evaporation of solvent following the curing of the polyurethane. However, given the even strain distribution, this consistent or concurrent relative change in wavelength does not affect the films capacity in serving as a full-field strain sensor for sensing strain contour, which is a localized strain pattern relative to that of nearby regions. More studies on how to reduce the added compressive strain will be carried out in future research.

Comparing Figures 4.8a and 4.8b, we find that the magnitudes of the peaks in emission intensity has no quenching. Table 4.3 shows the spectrum statistics on PFO-SWCNTs film (S-I9-0-Spr-1), while Table 4.4 shows the spectrum statistics on

Table 4.3 : Spectrum statistics on PFO-SWCNTs film (S-I9-0-Spr-1).

Parameter		(7,5)	(7,6)	(8,6)	(8,7)	(7,6)-(7,5)
λ (nm)	mean	1050.9	1135.94	1197.84	1278.52	85.04
	std	0.79	0.46	0.95	0.68	0.98
I (a.u.)	mean	5710.35	13724.4	3879.46	3029.84	NA
	std	895.18	1782.34	710.74	521.03	NA

PFO-SWCNTs film with an additional layer of polyurethane cured for 2 days. The wavelength at peaks shift after the application of the additional layer of polyurethane, indicating the change in the strain conditions of SWCNTs in smart skin. (7,6)-(7,5) peak separation changes from 85.04 nm to 95.37 nm, implying an 0.6% compression strain in SWCNTs. We will further analyze the reason for the big spectral shift after the application of the top coating.

Table 4.4 : Spectrum statistics on PFO-SWCNTs film with additional layer of polyurethane (S-I9-0-Spr-1)

Parameter		(7,5)	(7,6)	(8,6)	(8,7)	(7,6)-(7,5)
λ (nm)	mean	1045.05	1140.42	1186.29*	1283.54	95.37
	std	0.46	0.74	6.87*	0.59	0.96
I (a.u.)	mean	6972.27	13152.8	4053.57	2769.84	na
	std	1262.54	2193.49	669.57	483.86	na

* Erroneous peak fitting results of (8,6) peak due to the interference of (7,6) peak.

For the actual fabrication of the Generation-III S^4 film, we propose a layer-by-

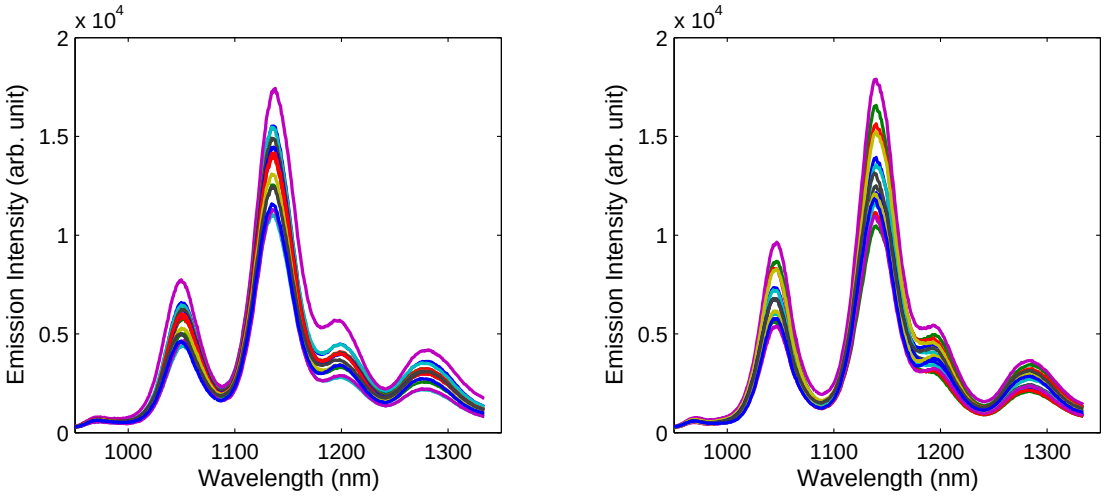

(a) Sensing layer

(b) Sensing layer + PU layer

Figure 4.8 : Spectra at 15 different measuring locations (left) on a PFO-SWCNTs film on a roughened PMMA substrate, and (right) on a PFO-SWCNTs layer + PU layer film.

layer "sandwich film-sensor structure as follows: 1) spray coat PFO-SWCNTs-toluene (centrifugated) suspension on a clean, roughened substrate to form the sensing layer; 2) perform heat treatment on the sensing layer of PFO-SWCNTs film, by using heating tools such as a vacuumed oven; 3) spray or brush coat a protective coating, such as polyurethane, on the top of the cured sensing layer of PFO-SWCNTs film.

4.4 Statistical Evaluation of S^4 Films

4.4.1 Automated Strain Scanning System

Practical application of the S^4 method requires a compact readout apparatus that can be easily positioned and an automatic computerized system for measuring large or complex surfaces in a controllable fashion. Figure 4.10 shows a schematic dia-

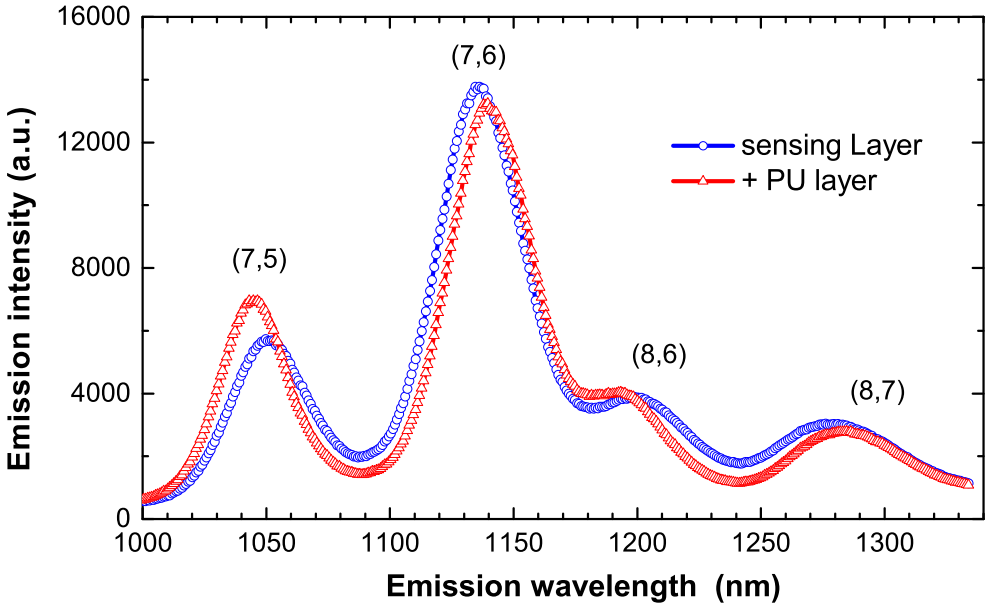

Figure 4.9 : Emission spectra (averaged using measurements at 15 different locations) on sensing layer and on sandwich structured S^4 film (under 660 nm laser excitation).

gram of an S^4 reader head incorporating a small diode laser for SWCNT excitation. In this study, the wavelength of the exciting laser is set at about 660 nm. Optical components, such as filters, half-wave plate and lenses are firstly used to filter, polarize and focus the laser. The SWCNT fluorescence emissions are then collected and transmitted to a spectrometer for measuring the near-infrared (NIR) spectra. This optical reader is compact and light enough to be positioned by a 3D printer (shown in Figure 4.10), whose tracking and control system enables accurate positioning and measurement. Computer program moves the read head to the desired x,y-coordinates and z-coordinate (for proper optical distance from the specimen surface) with a spatial resolution of less than 0.1 mm. The S^4 automation system can be used to move the optical read head to any position or orientation on test specimens precisely in

order to measure NIR spectra to develop strain maps.

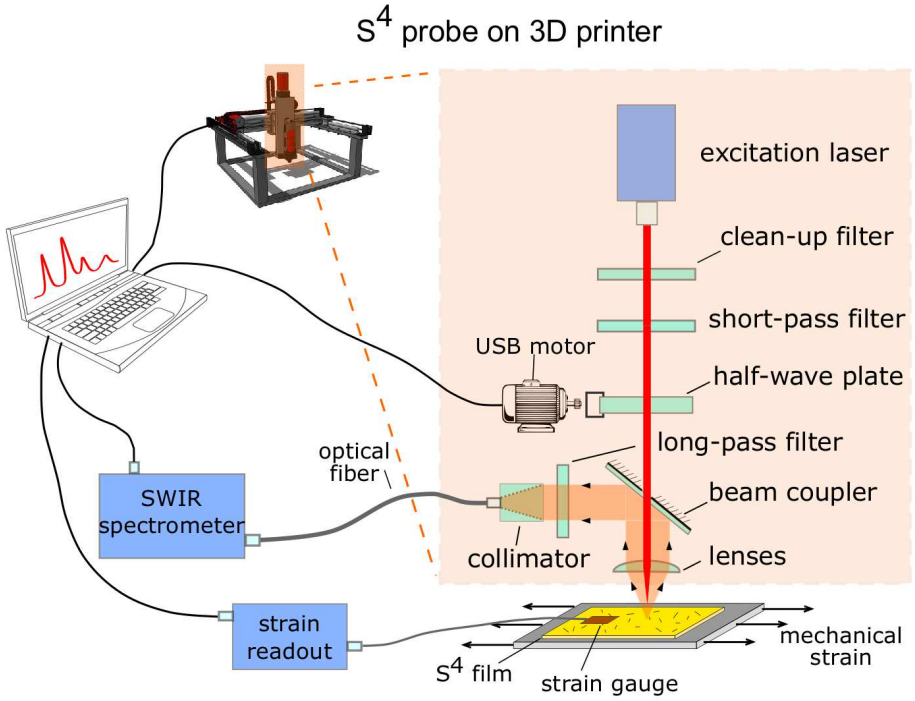

Figure 4.10 : Schematic diagram of S^4 strain probe on a 3D printer.

Automation of the S^4 strain measurements is an important goal for two reasons. First, it allows large data sets to be collected and statistically analyzed in short amount of time. This enables us to identify factors that limit the S^4 techniques' performance and quantitatively evaluate improvement efforts. Second, automation is clearly essential for practical implementation and surface strain mapping. S^4 automation involves both hardware and software. In order to assess film homogeneity and measure strains at specific location and direction, we have adapted a small commercial 3D printer (see Figure 4.12) by replacing its print head assembly with a version of our optical read head that is still lighter and more compact than the one shown in Figure 4.11.

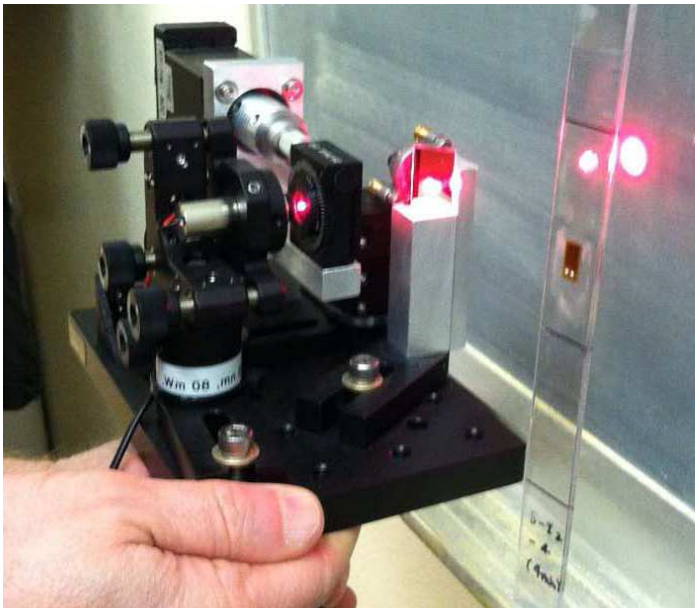

Figure 4.11 : Photo of the 4" x 6" hand held S^4 optical probe.

This new scanning optical strain reader is shown in Figure 4.12. A notebook computer running custom LabVIEW software controls positioning of the read head and spectral data acquisition from the multichannel InGaAs spectrometer. Through stepper motor controllers, the program moves the read head to the desired x,y-coordinates (within a range of 200 mm x 200 mm) and then adjusts the z-coordinate (height) for proper optical distance from the specimen surface. This process allows measurements on tilted or curved specimens. Positioning resolution is better than 0.1 mm in all axes. We note that the gage length for S^4 measurements is smaller than 0.1 mm. It is determined by the spot size of the focused excitation beam and is independent of film thickness. After the emission spectrum has been captured at a point/direction, the program precisely locates the specific (n,m) emission peaks selected for strain monitoring typically (7,5), (7,6) and (8,6) by fitting to separate local Gaussian functions.

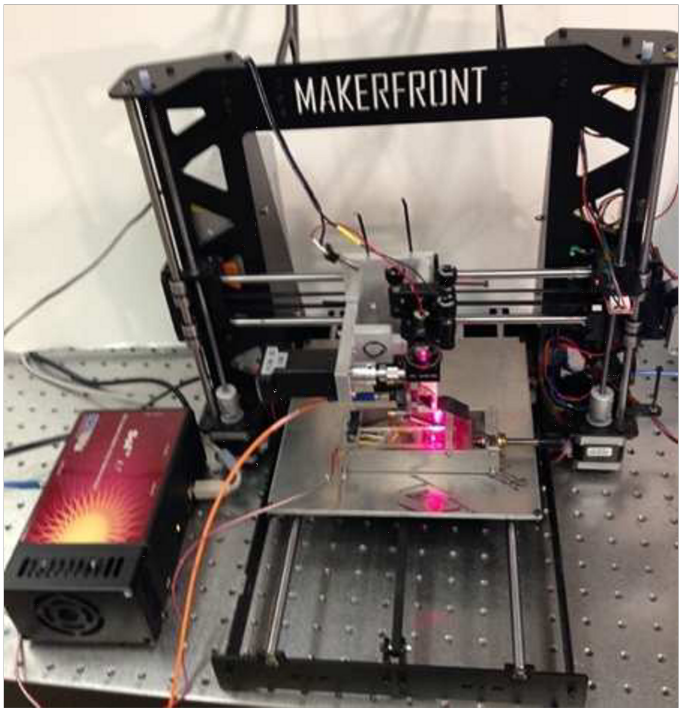

Figure 4.12 : Photo of the S^4 probe head mounted onto a computer-controlled 3D printer frame to allow automated scanning of specimens. The orange optical fiber transmits fluorescence collected from the S^4 film to the short-wave infrared (SWIR) spectrometer seen in the lower left corner of the photo.

Measurement uncertainties in S^4 strain map data may be caused by the limited precision of single-point strain readings and also point-to-point differences in S^4 film properties, such as inhomogeneous initial strains. The automated scanning system described above allows us to explore and distinguish these contributions. Figure 4.13 shows a histogram of the (7,6) peak wavelengths found from 1650 repeated spectral measurements at the same position on an S^4 film. The results fit very well to a Gaussian distribution with 3σ (3 x standard deviation) of 0.35 nm, corresponding to 100 $\mu\epsilon$ in deduced strain.

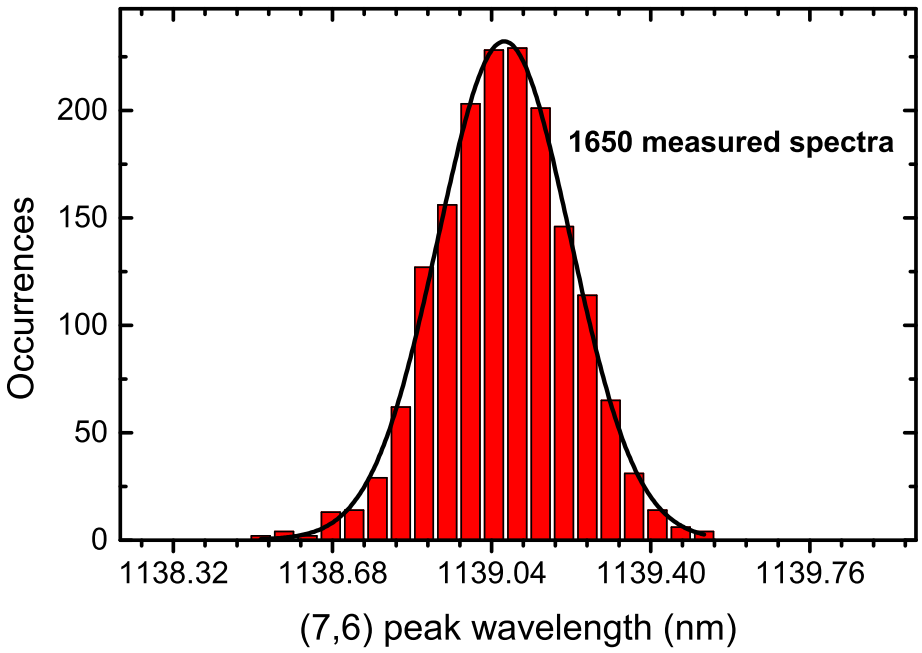

Figure 4.13 : Histogram of (7,6) peak positions deduced from 1650 repeated spectral measurements at one position on an S^4 test film. The solid line is a Gaussian best fit to the data.

We would then expect that S^4 measurements made at different points on a specimen surface would show variations in spectral peak positions given by this value plus a contribution from spatial inhomogeneity. The latter might result from local strain differences in uneven polymer films induced by contraction during curing. Using the automated scanning system and 2.5 s of data acquisition per position, we have performed spectral measurements at a grid of 169 positions on the surface of a Generation-III S^4-coated test plate before it is deliberately strained. Values found for the (7,6) (7,5) peak separation, which is proportional to strain, are plotted as a 2D color map in Figure 4.14. One can see that this baseline strain map shows minor systematic patterns that slightly exceed the single-point measurement precision.

The standard deviation for the entire set of 169 points is 0.23 nm. Future experiments will explore ways to minimize the underlying spectral variations by optimizing coating formulations, surface pre-treatments, application techniques, and film curing methods. We also hope to improve the precision of peak wavelength measurements by increasing the signal-to-noise ratio of captured spectra. This is achieved by using Generation-III S^4 films, that avoid strong quenching of SWCNT fluorescence and provide more intense spectra, and/or by increased averaging of spectral data.

4.4.2 Statistical Evaluation of PFO-SWCNTs Film

Since PFO-SWCNTs-toluene suspension has a low concentration of PFO 1 mg/mL in toluene, the suspension can be used to perform air-brushed film application due to the low viscosity. This is a big advantage in future coating on large structural surface compared to the first two generations of S^4 films. Figure 4.8a shows the spectra at 15 different measuring locations on PFO-SWCNTs film (sprayed). According to our experience, distribution in thickness of PFO-SWCNTs film (sprayed) is better than the brush-coated one and the standard deviation in emission intensity of the former also outperforms the latter. In the further study, we will adopt spray coating as the main strategy to apply PFO-SWCNTs film.

Table 4.5 shows the statistical investigation of the wavelengths and magnitudes at the peaks in spectra collected at 155 spots on PFO-SWCNTs film (S-I9-0-spr) spray-coated on an aluminum slide at room temperature. The standard deviation (std) in the wavelength at (7,6)-(7,5) separation is 0.82 nm. The sensitivities of Generation-I, II and III S^4 vary from 14 $nm/\%$ to 20 $nm/\%$. It implies that the standard deviation of the original strain is 440 $\mu\varepsilon$ in the PFO-SWCNTs film.

After fabrication of S^4 films, we have to examine, supervise and control the quality

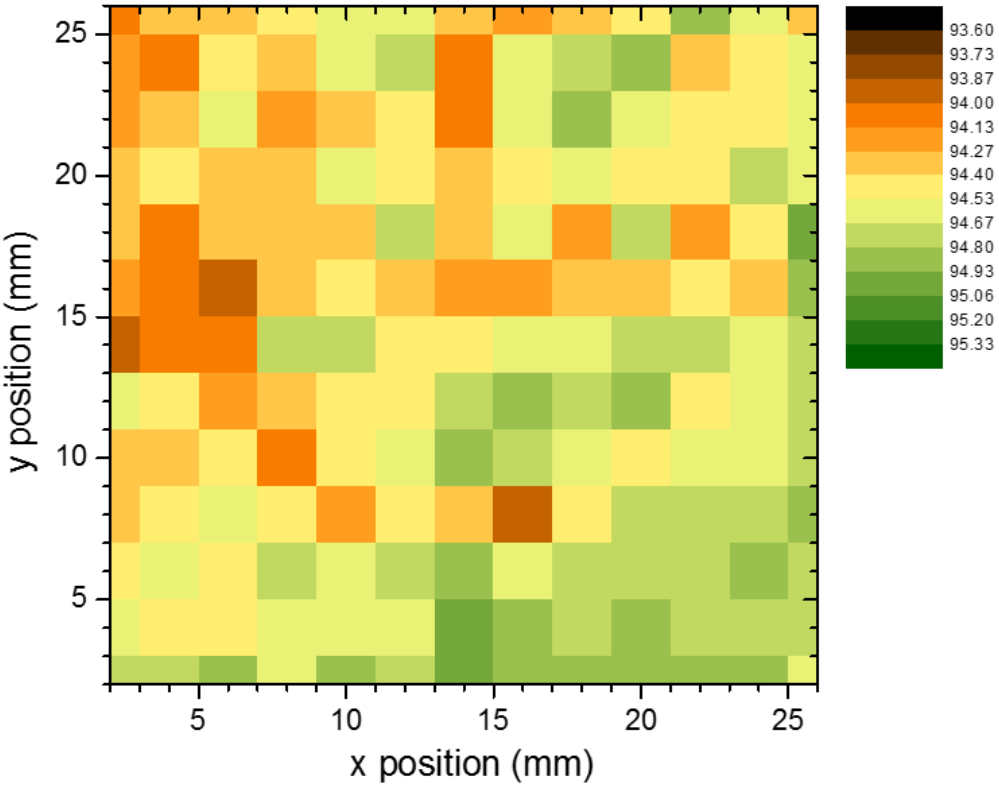

Figure 4.14 : Plot of spectral strain parameters measured by scanning 169 points on the surface of an substrate coated with an S^4 film. Note that this is a baseline map measured before the specimen was strained. Color-mapped values show separations (in nm) between (7,6) and (7,5) spectral peaks. The standard deviation of the full set of points is 0.23 nm.

of a film before it is used as a reliable full-field sensor. Throughout the sensing film, qualities ,such as smoothness in film thickness, homogeneity in SWCNT concentration distribution, randomness in SWCNT orientational distribution and non-existence of SWCNTs aggregation, should be checked and ensured.

We now evaluate the SWCNT concentration distribution and orientational distribution in a point-by-point sense by viewing the short-wave IR fluorescence mi-

Table 4.5 : Statistics of 155 spectra measured on PFO-SWCNTs film (S-I9-0-spr)

Parameter		(7,5)	(7,6)	(8,6)	(8,7)	(7,6)-(7,5)
λ (nm)	mean	1050.41	1139.26	1182.16	1282.16	88.86
	std	0.71	0.26	130.18	0.43	**0.82**
I (a.u.)	mean	22506.34	40625.10	10312.74	5722.24	na
	std	4584.70	7805.69	5343.70	1790.67	na

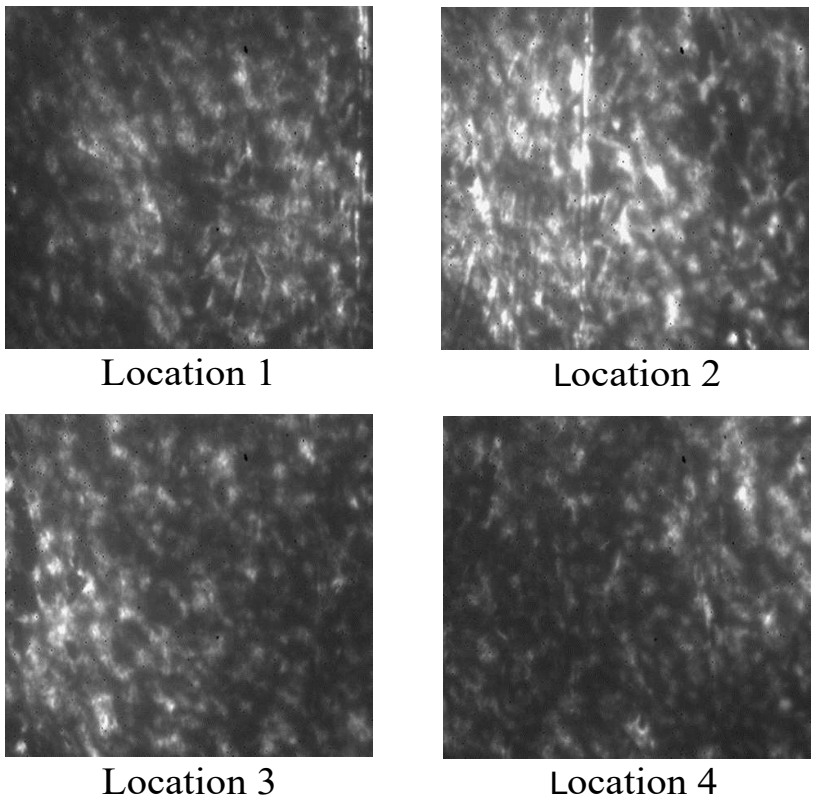

Figure 4.15 : Short-wave IR fluorescence microscopy on Generation-III S^4 film ($160\,\mu m \times 120\,\mu m$)

croscopies. Figure 4.15 is the short-wave IR fluorescence microscopies taken at four random location with the size of $160\,\mu m \times 120\,\mu m$ on the prepared Generation-III S^4

film (S-I9-0-Spr-1). Laser penetrates through transparent PMMA bar and onto S^4 films; hence, there might be some reflection and refraction from the top surface of PMMA bar(roughened) as evident in vertical lines at location 2 (see Figure 4.15).

Figure 4.16 shows the emission spectra at four different spots with a diameter of 2 μm providing a detailed view of the existence of sufficient amount of all the four SWCNTs species of our interest, (7,5), (7,6), (8,6) and (8,7), within such a small area.

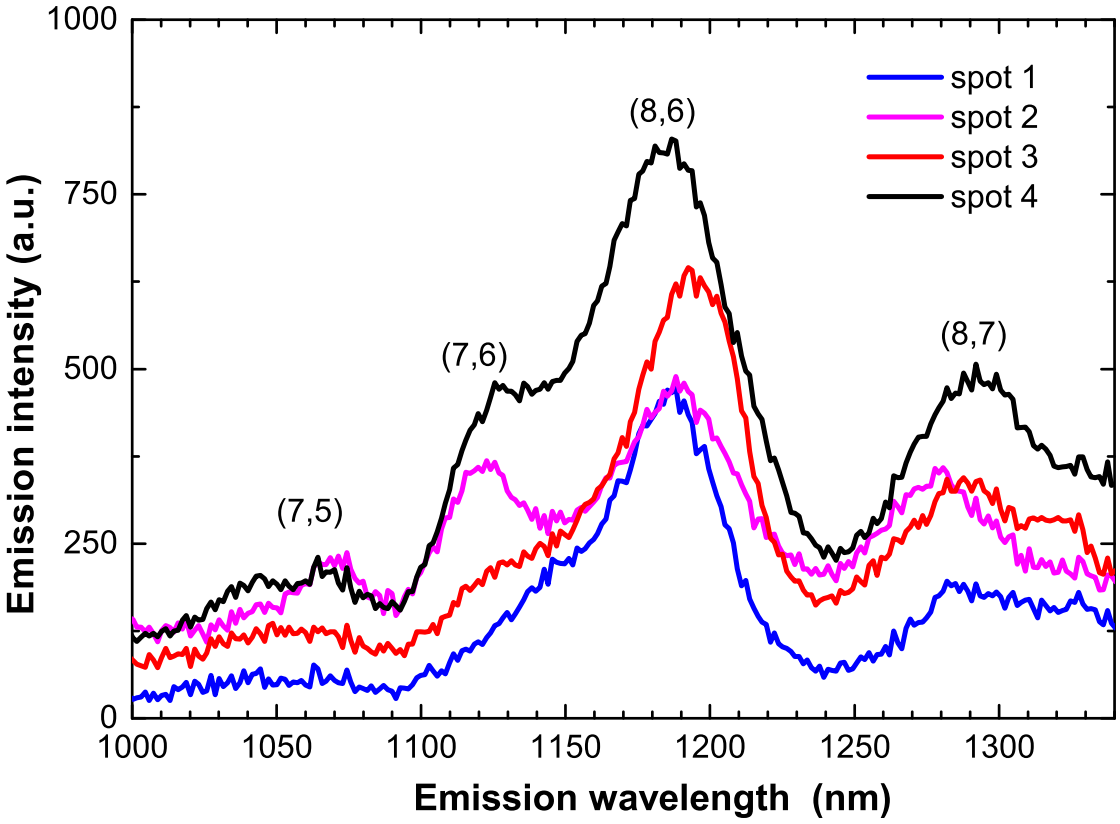

Figure 4.16 : Spectra measured at 4 different spot on S^4 film with an aperture with a diameter of 2 μm (740 nm laser excitation).

By using statistical evaluation of wavelength, we can ascertain the strain condition in smart skin as described in previous sections. Also from the correlation

coefficients between the wavelengths of different species of carbon nanotubes, we can infer the existence of aggregation of SWCNTs from different species. For example, Table 4.6 shows a PFO-SWCNTs film (S-I10-AlPlate-1) prepared by using PFO-SWCNTs-toluene suspension at different temperature before and after heat treatment. The standard deviation of (7,6)-(7,5) peak separation shown in Table 4.6 does not change very much even under a heat treatment at 140 $^{\circ}C$ which is close to the melting temperature of PFO at about 175 $^{\circ}C$. The strong negative correlation between (7,5) wavelength and (7,6) wavelength does not change much after the heat treatment(as shown in Table 4.7). This indicates that the aggregations of (7,5) and (7,6) nanotubes are so much that the strain relaxation cannot take place even in a softer polymeric environment under hot temperature. The correlation coefficient matrix of peak wavelength (peak position) to peak, and the correlation coefficient matrix of peak magnitude to peak magnitude can also provide us with much information. The exploitation of those statistical results can benefit us in developing better smart skin.

4.5 Mechanical Tests of Generation-III S^4 Film

4.5.1 Mechanical Tests: Point-Wise Strain Sensing

PMMA specimens coated with the Generation-III smart skin are subjected to cyclic deformation over the strain range from 0 to 2000 $\mu\varepsilon$. Figure 4.17 shows the sequence of applied deformations and the resulting responses of the three spectral peak positions. The (7,5), (7,6) peaks shifted systematically with the applied strain, confirming efficient load transfer from the PMMA bar to the polymeric coating to the embedded SWCNTs. Figure 4.18 shows the linear dependence of the peak separation and the

Table 4.6 : Wavelength statistics of PFO-SWCNTs film (S-I10-AlPlate-1) before and after heat treatment

Temperature (^oC)		$\lambda_{(7,5)}$	$\lambda_{(7,6)}$	$\lambda_{(8,6)}$	$\lambda_{(8,7)}$	$\lambda_{(7,6)} - \lambda_{(7,5)}$
25	mean	1050.65	1135.84	1197.76	1275.62	85.19
	std	0.75	0.64	0.91	1.02	1.32
100	mean	1045.46	1138.06	1193.24	1281.06	92.60
	std	0.52	0.66	0.47	0.80	1.16
120	mean	1044.96	1138.88	1193.24	1282.30	93.92
	std	0.41	0.60	0.39	0.74	0.99
140	mean	1044.24	1139.68	1193.32	1282.74	95.43
	std	0.48	0.56	0.59	0.73	0.99

Table 4.7 : Wavelength-wavelength correlation coefficient before and after heat treatment

Temperature condition		(7,5) pos.	(7,6) pos.	(8,6) pos.	(8,7) pos.
Before heat treatment, 25 ^oC	(7,5) pos.	1.00	-0.78	0.31	-0.78
	(7,6) pos.	-0.78	1.00	-0.46	0.82
	(8,6) pos.	0.31	-0.46	1.00	-0.29
	(8,7) pos.	-0.78	0.82	-0.29	1.00
After heat treatment, 140 ^oC	(7,5) pos.	1.00	-0.83	0.37	-0.79
	(7,6) pos.	-0.83	1.00	0.07	0.87
	(8,6) pos.	0.37	0.07	1.00	-0.02
	(8,7) pos.	-0.79	0.87	-0.02	1.00

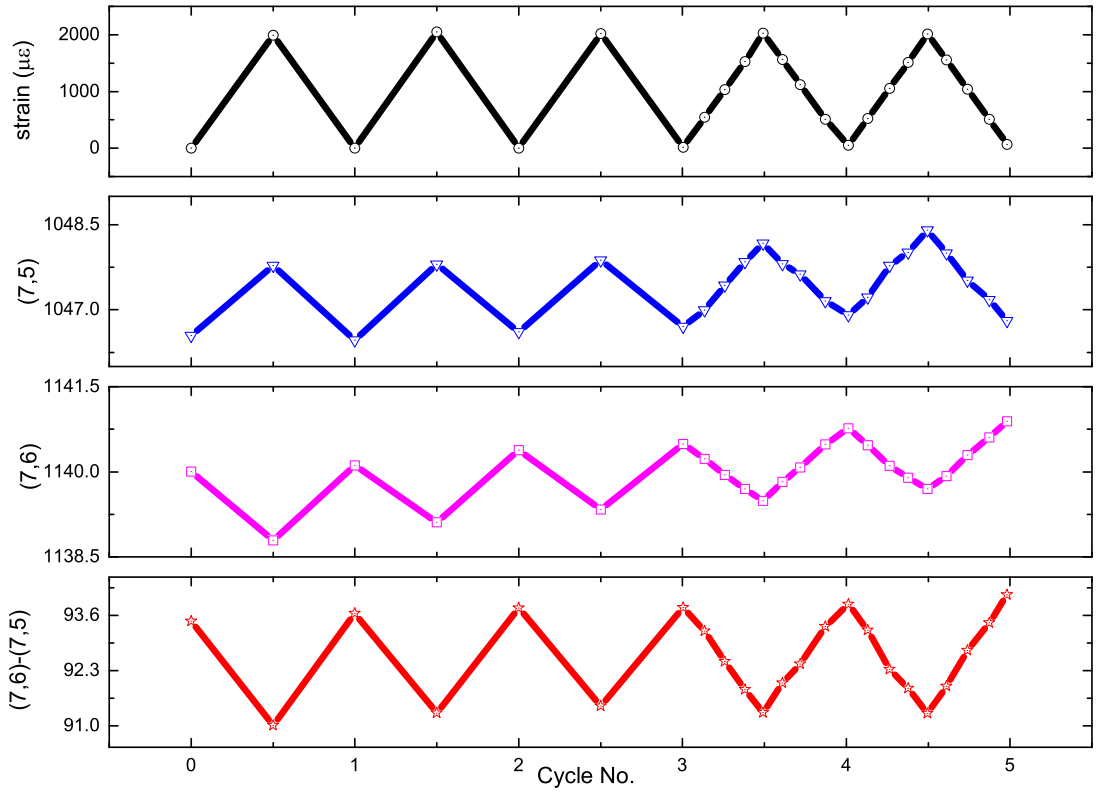

Figure 4.17 : Peak position response due to cyclic load of Generation-III smart skin (S-I9-0-2).

applied strain.

4.5.2 Mechanical Tests: Full-Field Strain Sensing 1

A 6061 aluminum alloy bar (coated with the PFO-SWCNTs layer) has a dimension of 2" × 12" × 1/8"; with a modulus of elasticity: E= 10,000 ksi; Yielding stress: σ_y= 35,000 psi; Ultimate stress: σ_u= 42,000 psi; Possion's ratio: ν=0.33; Yielding Force: F_y= σ_y × A = 35,000 psi x (2 in × 1/8 in) = 8,750 lbf. Theoretically, at a load of 8,750 lbf, the plastic strain would be approximately 2000 $\mu\varepsilon$. 2 strain gauges are used on the backside of the bar for validation.

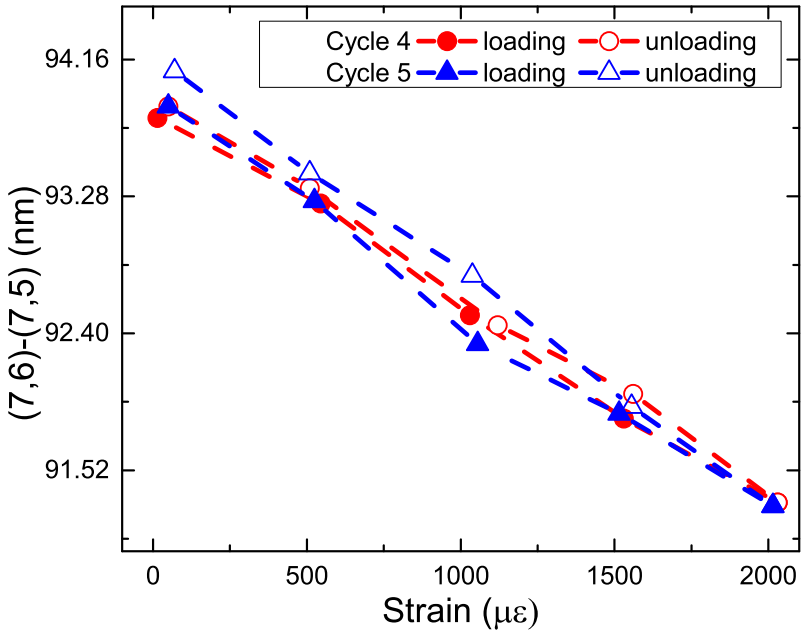

Figure 4.18 : Peak separation of the 4th and 5th load-unload cycle

In order to evaluate the spatial strain sensing efficiency of Generation-III S^4 film, a mechanical test of the bar is performed using MTS hydraulic machine. In the beginning the bar is loaded from 0 to 6,250 lbf and then load is released, with residual strain of less than 100 $\mu\varepsilon$, which is too small to detect. The bar is loaded again from 0 to 8,000 lbf for the second time (far from ultimate load 10,500 lbf).

As shown in Figure 4.19, the bar reached plastic state. After 7,000 lbf, strain grew nonlinearly, indicating failure, with steadily increasing load at 20 lbf/s. However, the gripping area of the bar was held firmly by the hydraulic grip. We suspect it is caused by small defects in the bar and initiated by a failure of the bar at gripping area. Because of the sudden failure, the two strain gages detached from the aluminum surface and the strain backed to around zero.

The strain map scanning measuring of 25.4 mm x 50.8 mm is chosen with a step size of 2.54 mm; in total 11 x 21 data points are used. A statistical evaluation

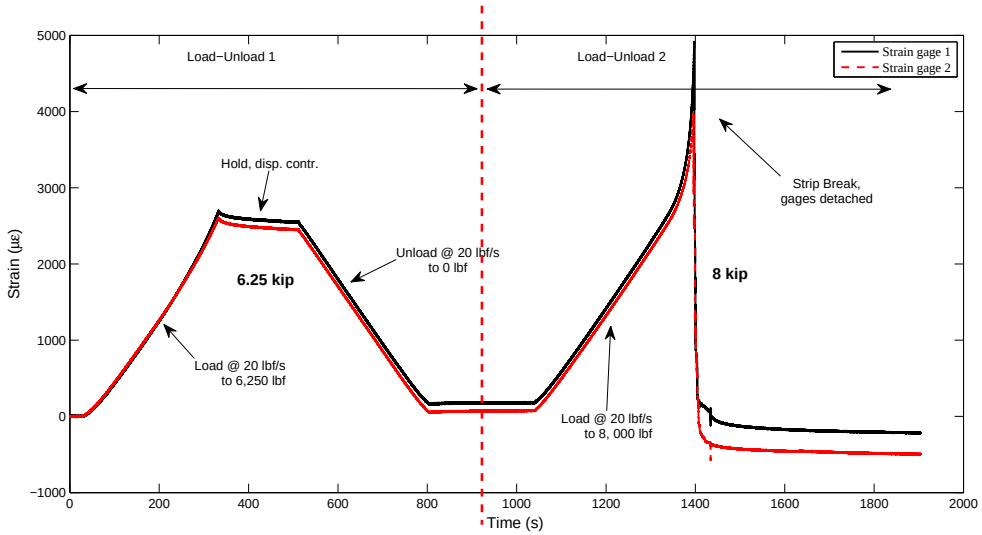

Figure 4.19 : Load-unload protocol and strain time histories

Table 4.8 : Statistics of S-I10-AlPlate-1 before and after loading

Load condition		$\lambda_{(7,5)}$	$\lambda_{(7,6)}$	$\lambda_{(8,6)}$	$\lambda_{(8,7)}$	$\lambda_{(7,6)} - \lambda_{(7,5)}$
Before Load	mean	1044.24	1139.68	1193.32	1282.74	95.43
	std	0.48	0.56	0.59	0.73	0.99
After Load	mean	1051.04	1135.71	1196.03	1277.22	84.67
	std	1.24	1.12	2.88	1.26	2.25

indicates large plastic strain within the aluminum bar. Usually, smart skin has a strain sensitivity in (7,6)-(7,5) peak separation of about 1.4 $nm/m\epsilon$. Hence, 10 nm decrease in (7,6)-(7,5) peak separation (shown in Table 4.8) means 5,000 $\mu\epsilon \sim$ 7,000 $\mu\epsilon$ tensile strain. The results are very reasonable. More experiments on 2D strain scanning will be carried out next on another metallic bar.

4.5.3 Mechanical Tests: Full-Field Strain Sensing 2

Two dimensional (2D) strain sensing can be performed by obtaining the fluorescence spectrum on a grid of positions. In order to evaluate the spatial strain sensing efficiency of the Generation-III S^4 film, a mechanical test of a copper bar is performed. As shown in Figure 4.20 (right), a copper bar (with a hole in middle) coated with S^4 film is steadily stretched by axial force using a MTS hydraulic testing system. The dimensions of the specimen are 304.8 mm x 50.8 mm x 6.35 mm and the hole has a diameter of 6.35 mm. The newly designed S^4 film is applied on the front side and four channels of strain gages serving as data control are attached on the back side as shown in Figure 4.20 (left). An axial load is applied on the specimen and increased gradually at a fixed rate until yielding of the material near the hole due to the stress concentration (see Figure 4.21). After holding for several minutes, the load is released gradually at fixed rate until the axial load relaxes completely. Plastic strain is created in the specimen because of the permanent deformation of the material near the hole. The hydraulic grips are released completely before subjecting the sample to strain scanning.

Pointwise strain validation measurements are performed by the attaching strain gages at the specified locations (see Figure 4.20 left). Strain gages at channel 1 and channel 2 measure strain in loading direction (referred to as x direction) and are located 10 mm away from the center of the hole in y direction. Strain gages at channel 3 and channel 4 are located 10 mm away from the center of the hole in x direction to measure strain in x direction and y direction, respectively. The purpose of attaching the strain gauges is to monitor the strain condition during the mechanical loading and to compare it to the S^4 strain measurements. Also it should be noted that before the mechanical test, 2D strain scans were performed on the

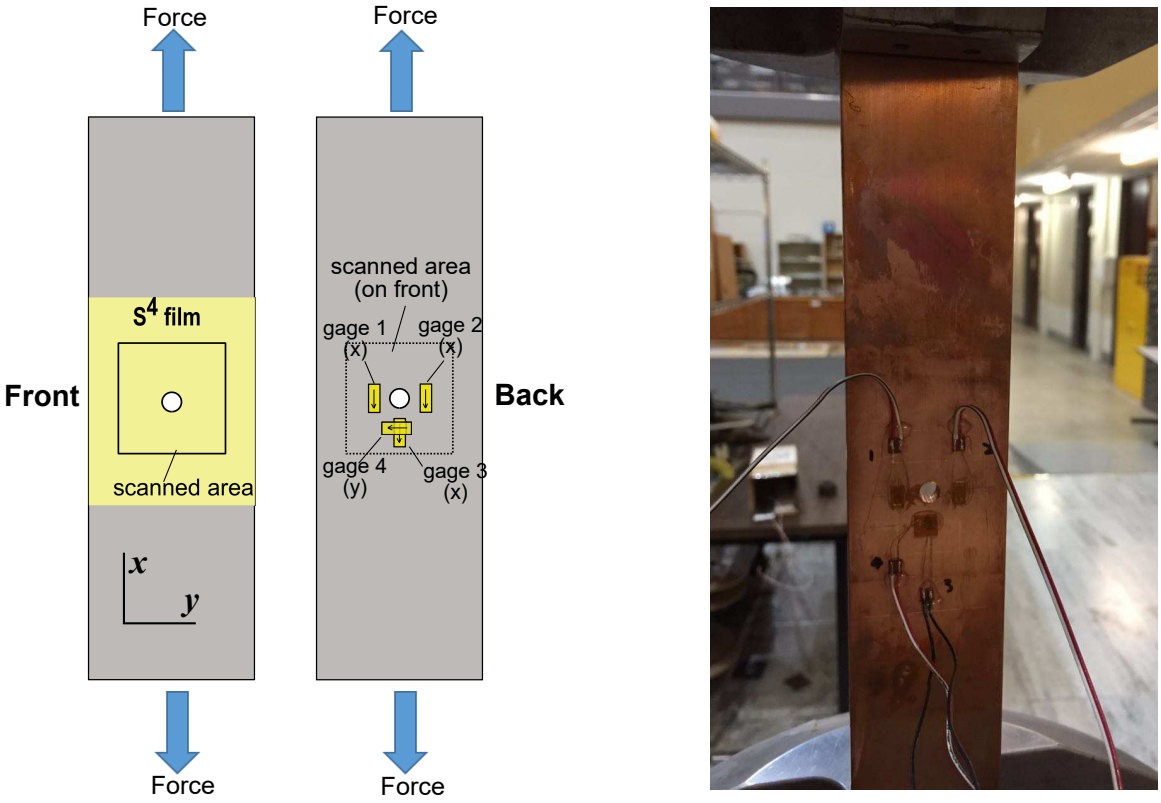

Figure 4.20 : (left) Schematic diagram of smart skin and strain gage deployments. (right) Photo of a copper specimen mounted on a MTS machine.

same area around the hole (bounded within a square area of 40 mm x 40 mm) using the aforementioned noncontact strain-sensing setup shown in Figure 4.12. The time histories of the strains recorded during the mechanical test from discrete strain gages are shown in Figure 4.21 (b). The axial force is applied in 3 loading-unloading cycles with peak values of 8,000 lbf, 12,000 lbf and 16,000 lbf as shown in Figure 4.21 (a). In the process, strain collected from strain gauges are monitored measure the plastic strain which occurs in the plate. In the first two loading-unloading cycles, not much plastic strains are observed. While in the third cycle loading, total strains measured in channel 1 and channel 2 strain gages grow exponentially until reaching

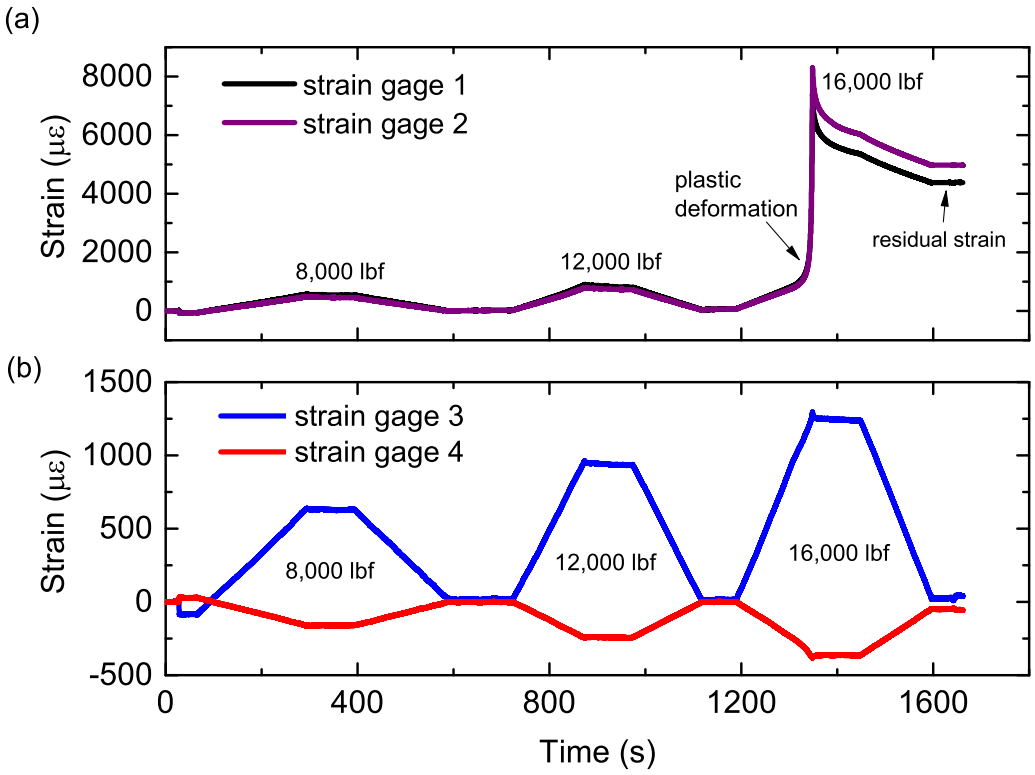

Figure 4.21 : The time histories of the strains recorded from the strain gages.

about 7400-8300 $\mu\epsilon$, the maximum strain in loading direction as shown in Figure 4.21 (a). A nonlinear increase in strain due to a linearly increasing load at a fixed location implies the specimen or part of the specimen has exceeded the yielding stage. In the unloading stage of the third cycle, strains in channel 1 and channel 2 gages decreased to 4392 $\mu\epsilon$ and 4973 $\mu\epsilon$, respectively, after unloading. In Figure 4.21 (b), channel 3 and channel 4 strain histories reveal that the total strains go back to almost zero without much plastic strains remaining indicating that the material on the measured spot are still within elastic stage. After mechanical test, a fluorescence scanning is performed on the plastically deformed plate by using the 2D scanning system.

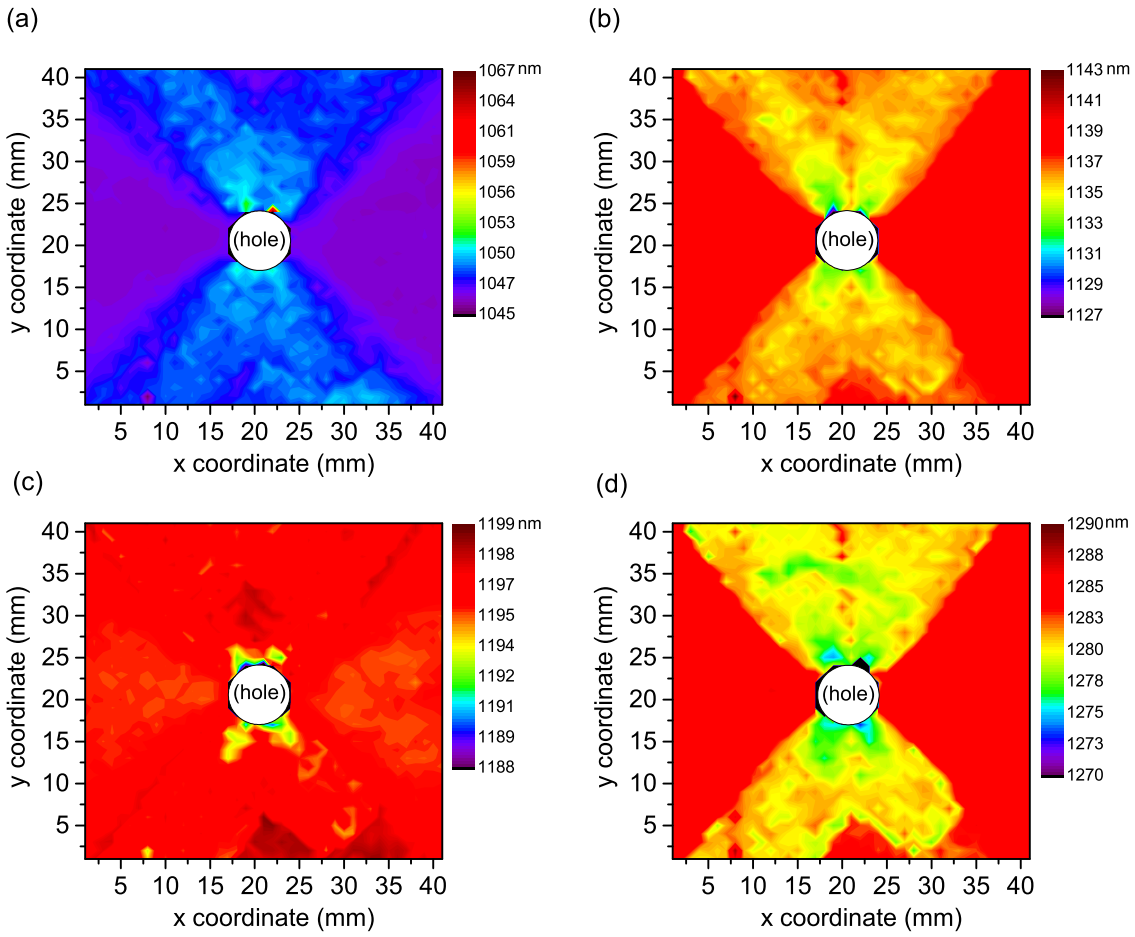

Figure 4.22 : Distributions on S^4 film of wavelengths at (a) (7,5) peak, (b) (7,6) peak, (c) (8,6) peak, (d) (8,7) peak after residual deformation on the copper plate.

Spectra are measured by using a series of measurements on a rectangular grid of 41 mm x 41 mm. In total, 1681 spectrum are obtained by sequentially interrogating the SWCNTs at each spot of the grid intersections. Figure 4.22 shows the interesting distributions of (n,m) peaks caused by the permanent strain on the copper plate after the mechanical test. The contours of the strain distributions are reconstructed by interpolating the wavelength values at the grid spots. From Figure 4.22, interesting

patterns in the strain contours are observed.

In Figure 4.22 (a), the (7,5) contour map at the top side and bottom side of the hole within x∈[15 mm, 25 mm] shows a relatively larger values of wavelengths. While relatively smaller values are found within an hourglass shaped are to the left and right side of the hole. Because (7,5) SWCNTs species is classified as mod 2 semiconducting SWCNTs, larger wavelength means more tensile strain applied on the SWCNTs, while smaller means more compressive strain. Hence, Figure 4.22 (a) shows tensile strain on the top and bottom of the hole while compressive strain on the left and right side of the hole. In Figure 4.22(b) and (d), the contour maps at the top and bottom of the hole within x∈[15mm, 25mm] represent relative smaller values of wavelengths. Because (7,6) and (8,7) SWCNTs species both are classified as mod 1 semiconducting SWCNTs, smaller wavelength means more tensile strain applied on the SWCNTs, while larger means more compressive strain. Relatively larger values can be found within an hourglass shaped area to the left and right side of the hole. Hence, Figure 4.22(b) and (d) show tensile strain on the top and bottom of the hole while compressive strain on the left and right side of the hole.

The results from Figure 4.22 (a), (b), (d) show a consistent physical perspective. However, Figure 4.22 (c) somehow cannot explain the mechanical strain distribution clearly. This is due to the poor quality of the fluorescence spectrum at (8,6) of this batch of S^4 films for testing. The (8,6) spectrum peak is not very distinct due to the influence of the (7,6) peak. Since the peak is not very distinguishable, the accuracy of obtaining the wavelength at the peak by curve fitting analysis is limited considerably. This one of the main reasons that the peak separation of (7,5) and (7,6) is used to perform strain sensing.

The shift of peak separation (7,6)-(7,5) is linearly dependent on applied strain

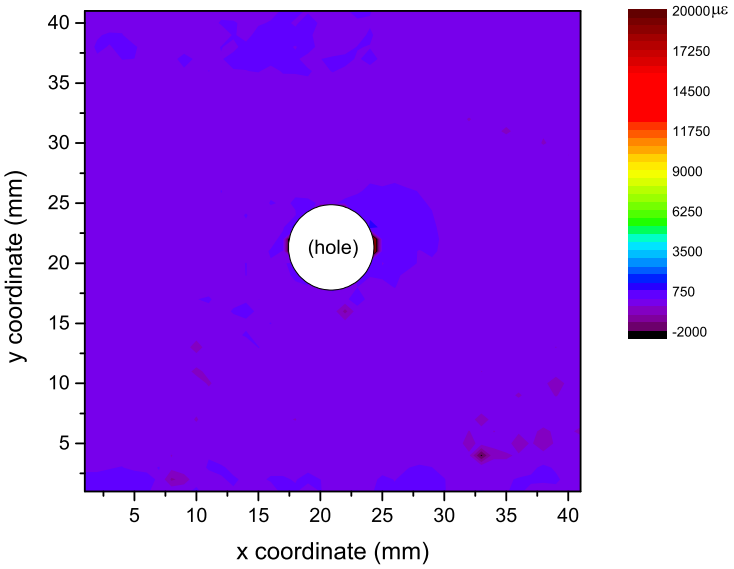

Figure 4.23 : Strain distributions in x direction ϵ_{xx} measured by S^4 before mechanical stretching (PFO-SWCNTs spray coated and polyurethane brush coated).

and has a shift rate of 1.4 $nm/m\epsilon$ for the (7,5)-(7,6) peak separation, which has been verified from the pointwise experiment. As shown in Figure 4.23 and Figure 4.24, the strain distributions of ϵ_{xx} before test and after test are measured by S^4 film using (7,6)-(7,5) peak separation data. The active gage length and the active gage width of channel 1 and channel 2 strain gages are 3.2 mm and 2.5 mm, respectively. In Figure 4.24, two rectangular boxes with black border indicate the positions of the two strain gages. As known, strain gages measure the average values of strains within the covered area. Within the box the strain are about 5000-5500 $\mu\epsilon$, which match the strain readings from the two strain gauges very well. Strain contour is successfully mapped and the strain/stress concentration phenomena caused by the structural irregularity introduced (hole in middle) is clearly identified.

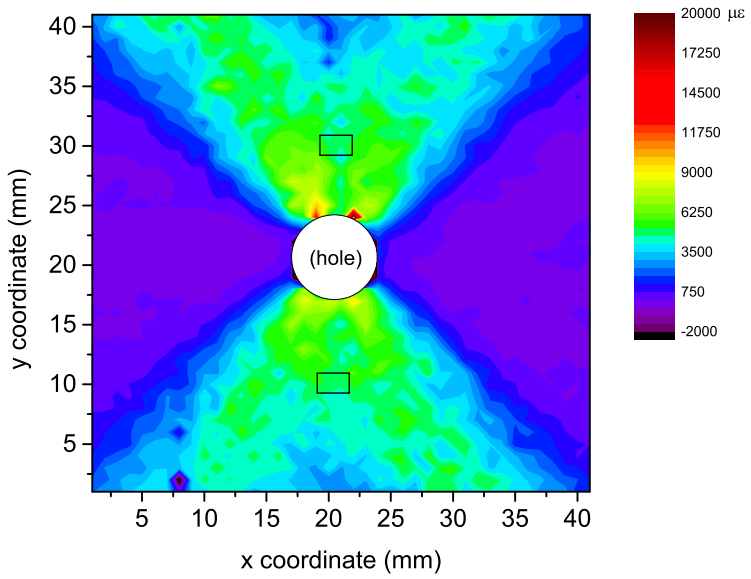

Figure 4.24 : Strain distributions in x direction ϵ_{xx} measured by S^4 after stretched. PFO-SWCNTs spray coated and polyurethane brush coated.

4.6 Concluding Remarks

In this Chapter, a layer-by-layer film structure (Generation-III) is proposed to minimize the possible chemical reaction between polymer matrix and SWCNTs in order to obtain fluorescence spectrum with higher quality which enhances the accuracy of strain interpretation. Mechanical tests are performed (1) on a PMMA bar, (2) an aluminum bar and (3) a copper bar with central hole respectively. The results of the first experiment show linear dependence of (n,m) peak responses to the applied mechanical strain validating S^4 as an efficient strain sensor. The second experimental rate of spectral shift for peak separation between (7,6) and (7,5) peaks, which is about 1.4 $nm/m\epsilon$ indicates sufficient stress transfer from PFO-SWCNTs. In the third experiment, an axial loading-unloading test is performed on a copper plate (with a

hole in middle), coated with S^4 sensor, to yield the material around the hole causing plastic strain in the specimen. Plastic strain is measured by using the automated S^4 sensing system. A series of spectrum are firstly obtained on a rectangular grid with a dimension of 41 mm x 41 mm. The strain values are then interpreted by curve fitting technique and a strain map is reconstructed by 2D interpolation method. The interpreted strain values at the corresponding locations on the S^4 film matches the conventional strain gage readings. The strain contour captured by the S^4 film corresponds satisfactorily to the mechanical phenomena of the stress/strain concentration caused by the hole in the plate. This reconstructed 2D strain contour map is the first such demonstration of the full-field strain sensing ability of S^4 film sensor on a macroscopic metallic structure based on fluorescence spectroscopy. By far, the mechanical tests of the Generation-III S^4 films show a good performance in strain sensing. More investigations will be performed to evaluate the S^4 film as a full-field sensing technology and to apply it in structural health monitoring and damage identification. In future, the new S^4 can be applied widely in engineering realms including, non-destructive testing, structural maintenance and damage identification.

Chapter 5

Application of S^4 on Measuring Full-field Residual Strain Fields

5.1 Introduction

Many failures in structures, such as ships, airplanes and offshore structures, are caused directly or indirectly by stress concentration. In this interesting phenomenon, the stress around a structural discontinuity is several times higher than the nominal stress at other spots. Normal strain/stress distribution patterns can be altered by a newly developed structural discontinuity, such as a damage or crack. Furthermore, fatigue cracking for brittle material and plastic deformation for ductile material are more likely to occur at these stress concentration area. Strain measured on structural surfaces can serve as a first-hand indicator of structural health condition for civil infrastructures, mechanical systems and aerospace structures. In many years, researchers have devoted much effort in analyzing stress concentration in structures and materials. Strain/stress analysis of the critical structural components under various loading conditions is carried out by researchers and engineers in different realms, such as structural design, fracture mechanics, fatigue and non-destructive evaluation.

Strain and stress has been intensively analyzed by analytical methods, numerical methods and experimental methods throughout the decades. The analytical methods, such as theory of elasticity [49–53], linear elastic fracture mechanics(LEFM) [54–57] and elasto-plastic fracture mechanics (EPFM) [58] have been used to study

strain/stress condition around discontinuities. Boundary value problems (BVP) can be solved analytically by using constitutive equations based on the elastic or plastic behavior of the material with specific load. Closed-form solutions can be obtained for simple geometries, constitutive relations and boundary conditions. Fracture is defined as the separation or the fragmentation of a solid body into two or more parts under the actions of stresses. Linear elastic fracture mechanics (LEFM) applies the theory of linear elasticity to the phenomenon of fracture and investigates mainly the propagation of crack [59]. The strain condition near normal structural discontinuity such as a hole or a crack can be calculated by using elasticity theory and LEFM. The basic hypotheses of LEFM are: (1) cracks are inherently present in a material; (2) a crack is a free, internal, plane surface in a linear elastic stress field;(3) the growth of the crack leading to the failure of the structural member is then predicted in terms of the tensile stress acting at the crack tip [59]. Numerical methods including finite difference method (FDM) [60,61], boundary element method (BEM) [62,63] and finite element method (FEM) [64–66] haven been used to investigate the strain condition around holes and crack-tips in many studies. Finite difference treatment use direct difference approximations to the partial differential equations governing the physical process and FDM has been used to study the dynamic stress intensity factors [60] and the dynamics of a fluid-filled crack [61]. In boundary element treatment, the primary results are the distributions of the variables on the boundary of the solution domain, which is defined in terms of values at a finite number of points [63]. BEM has been used in solving linear elastic crack problems [62], stress analysis and fracture mechanics problems [63]. FEM has been applied in the realm of fracture mechanics, fatigue analysis, experimental validation and structural design. FEM has been used to study stress concentration [64–66], optimal design [67] and remediation of stress

concentration [68] near circular holes on bar structures under static/dynamic loading. Two dimensional and three dimensional FEA have been adopted in analyzing strain/stress fields [52, 69], three dimension effect [70, 71] and plastic zone [72] around stationary notches and crack tips (in mode I and mode II elastic/plastic problems). ANSYS® and ABAQUS® are the two commercial FEM software which are commonly used to simulate the complex strain/stress condition near structrual discontinuities including crack-tips. [59] Failure in material is usually associated with the presence of high local stresses and strains in the vicinity of defects or structural discontinuities. Thus measuring the magnitude and distribution of these stresses and strains around these defects is very crucial for detecting them and understanding them. Full-field measurement methods for experimental studies on strain field around structural discontinuities/cracks include electronic speckle photography [73], grid method [74], digital image correlation (DIC) [75, 76], photoelasticity [77, 78]. Strain condition can be measured experimentally, while stress is usually referred by firstly obtaining the strain value at one specific spot and knowing the material property like Young's modulus. Strain sensing techniques are the paths to determine the stress condition experimentally of a structure in real practice.

In this Chapter, strain distributions near structural discontinuities, such as circular hole and rectangular notched crack in rectangular bars will be studied in detail. Firstly, Strain Sensing Smart Skin (S^4) sensor is used to measure the residual strain contours on aluminum specimens after large axial loading (beyond yield) and unloading process. In the following, elasticity theory and LEFM will be used to derive the closed-form solutions of strain field around discontinuities in a bar. Later finite element analysis (FEA) is performed using different material parameters to validate the strain distributions around the structural discontinuities from experiments.

5.2 Strain-Sensing Smart Skin (S^4) technique

SWCNTs are a family of high aspect ratio tubular structures containing only carbon atoms covalently bonded into specific ordered forms [29]. Each such form has a well-defined tube diameter and roll-up angle, and is uniquely labeled by a pair of integers (n, m) defining its chiral vector. Most SWCNT structural species are semiconducting ones and can show characteristic photoluminescence (fluorescence emission) at distinct near-IR wavelengths that correspond to their specific semiconducting band gaps [30,31]. It has been shown by theory and experiment that axial strains in SWCNTs cause predictable changes in electronic structure that systematically shift their spectral peak positions [1, 32]. These shifts in SWCNT fluorescence spectra reveal axial strains in each nanotube, suggesting that it is possible to devise a practical non-contact optical method to measure strains at macroscale using embedded SWCNTs as distributed sensors.

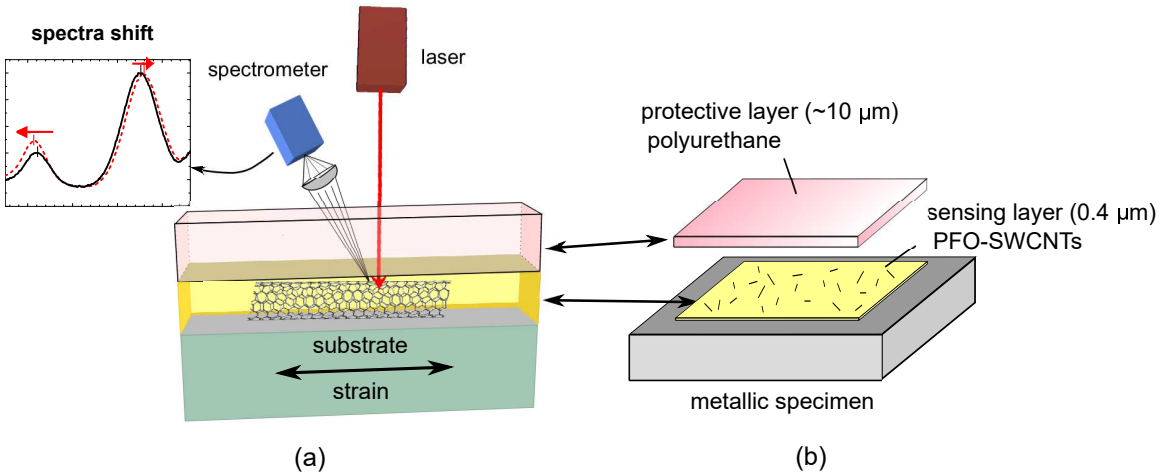

Figure 5.1 : Schematic of (a) S^4 film sensor (not to scale) and (b) the layered film structure.

In recent years, the authors and team of researchers [39, 40, 46, 47, 79] have developed Strain Sensing Smart Skin (S^4), which is a polymer coating containing diluted, well dispersed single-walled carbon nanotubes (SWCNTs) as sensors. The nanotubes are coated with the organic polymer PFO(Poly(9,9-di-n-octylfluorenyl-2,7-diyl)). As shown in Figure 5.1 the sensing layer of the dual-layer S^4 design is very thin polymer film, approximately 0.4 μm thick, adhering to the surface to be monitored. A top layer of polyurethane (PU) is applied over this to protect the sensing layer from environmental degradation. The top PU layer (with a thickness of about 10 μm) is selected to be transparent enough at red (excitation) and short-wave infrared (photoluminescence) wavelengths to permit spectral strain measurements on the sensing layer below.

In Figure 5.1, only a single SWCNT is shown to illustrate the concept, but S^4 films actually contain a very large numbers of randomly oriented SWCNTs. As demonstrated in Figure 5.1, when the metallic substrate undergoes mechanical strain the PFO polymer-SWCNTs is also strained, causing the emission peaks of SWCNTs excited by a laser to shift in wavelength. Using these spectral changes, we can deduce the strain field on structural surfaces. By adjusting the polarization direction of the linearly polarized excitation beam, we can preferentially monitor SWCNTs oriented parallel to that axis and determine strain in that direction. The recently characterized dual-layer S^4 film structure [79] is applied to metallic specimens in this study. Based on results to date, we expect that the S^4 method can reveal strain maps for large or complex structural surfaces, such as building facades airframe components (see Figure 5.2), without physical contact and at practical data acquisition speeds.

Figure 5.3 shows an example of strain measurement using an S^4 film coated on one side of the specimen. Spectra from SWCNTs (shown in Figure 5.3) in the film

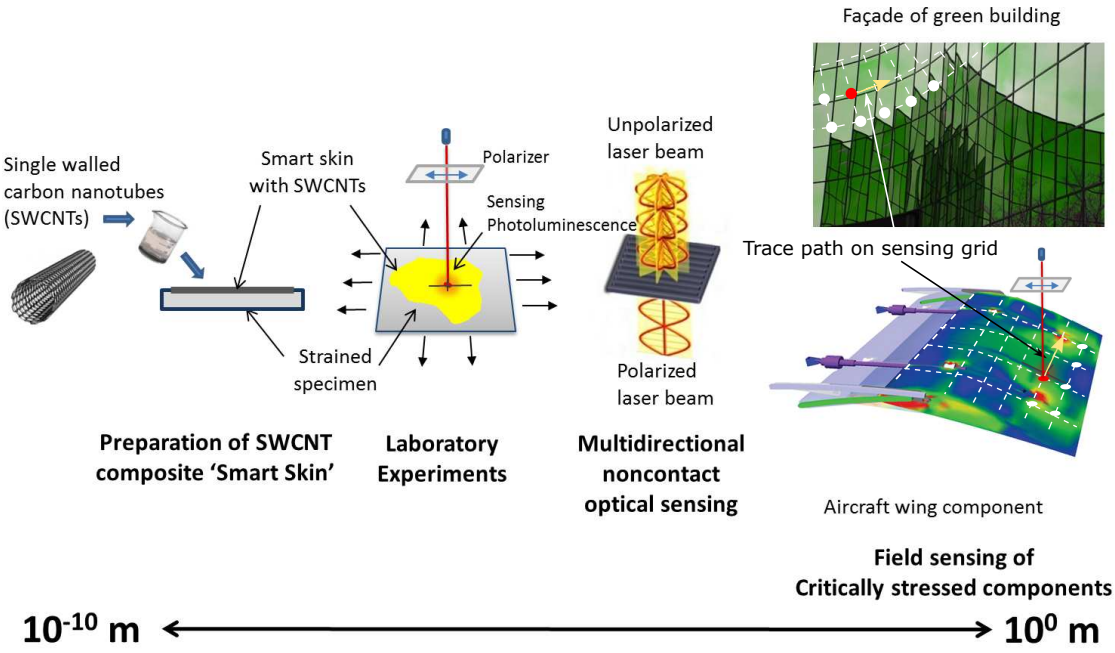

Figure 5.2 : Application of S^4 film sensor on buildings and aircraft wings. The white grid on the building and the aircraft wing represent the laser scanning grid for 2D strain map reconstruction, the red/white spots show the current/completed optical interrogation, and the light yellow arrows show the scanning path for 2D strain mapping.

are measured using the compact, portable readout apparatus while the specimen is subjected to cyclic loading in tension. Spectral shifts in the S^4 film emission are then compared with reference measurements from a conventional resistive foil gage.

The results in Figure 5.3 show an example of the correlation found between spectral response of the S^4 film and the independently measured deformation of a test specimen that was strained between 0 and 2000 $\mu\epsilon$ during five cycles of loading and unloading. The response is highly linear in this range. The separation between (7,6) and (7,5) nanotube emission peaks is found to be a reliable monitor of strain [46, 47, 79].

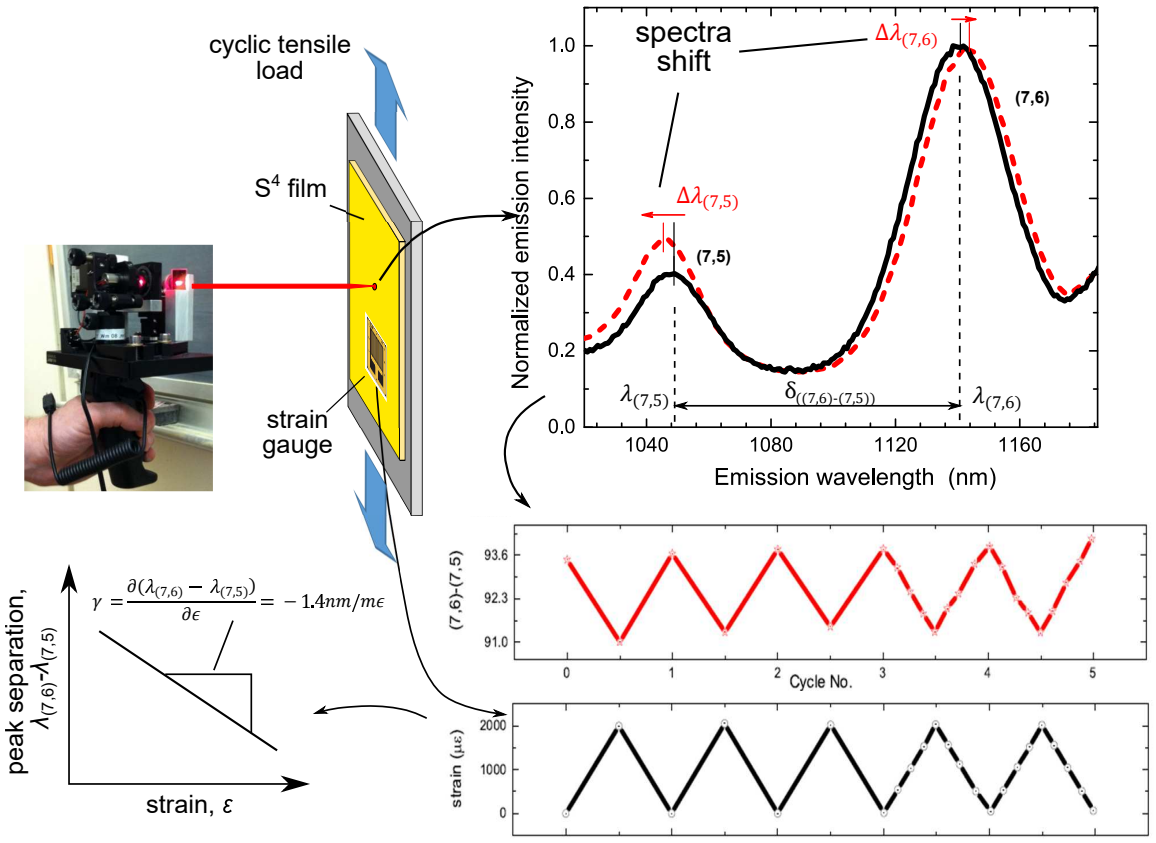

Figure 5.3 : An example of strain measurement using S^4 film sensor, with calibration using conventional foil strain gages. Measured spectra are shown as a solid line before loading and as a dashed line after loading.

5.2.1 S^4 Calibration, Measurement and Strain Map Computation

In our study, we use the separation between the two dominant emission peaks corresponding to the (7,5) (a so-called *mod* 2 structure) and (7,6) (a *mod* 1 structure) species of SWCNTs, as shown in Figures 5.1, 5.2 and 5.3. These peaks shift in opposite directions with nanotube axial strain, so their difference gives an improved sensitivity factor and also tends to cancel out effects from environmental changes that shift both peaks in the same direction. Hence, the peak separation (7,6) - (7,5) $\delta_{((7,6)-(7,5))}$ as

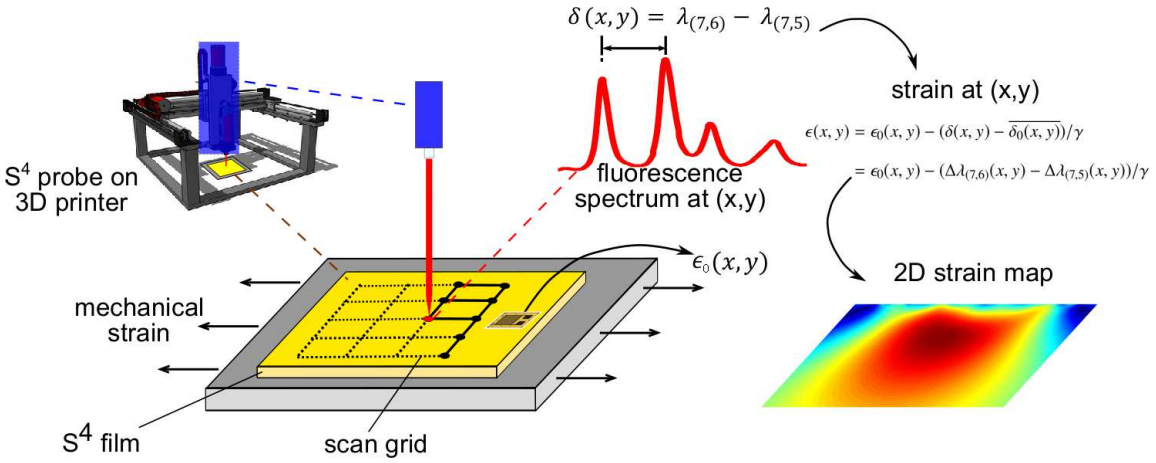

Figure 5.4 : Protocol for 2D strain mapping using S^4 film sensor.

shown in equation (5.1), is a good parameter for strain measurement [39, 46].

$$\delta_{((7,6)-(7,5))} = \lambda_{(7,6)} - \lambda_{(7,5)} \tag{5.1}$$

where $\lambda_{(7,5)}$ and $\lambda_{(7,6)}$ are the wavelengths at the characteristic peaks of (7,5) and (7,6) SWCNT species, respectively, as shown in Figure 5.3.

Calibration of the S^4 film is performed by using a single reference strain gage on the specimen as shown in Figure 5.3. According to the finding in the reports [46, 47], the strain sensitivity factor, $\gamma_{((7,6)-(7,5))}$ as shown in equation (5.2), has a consistent value of -1.4 $nm/m\epsilon$ when S^4 is prepared using the standard protocol [46]. For simplicity, we will use $\delta(x, y)$ (at location (x, y)) and γ to represent $\delta_{((7,6)-(7,5))}$ and $\gamma_{((7,6)-(7,5))}$, respectively, in the rest of the paper.

$$\gamma = \gamma_{((7,6)-(7,5))} = \frac{\partial \delta_{((7,6)-(7,5))}}{\partial \epsilon} \tag{5.2}$$

We performed 2D S^4 strain scans over a square area of 40 mm by 40 mm around the hole, before and after the mechanical test, with the laser polarization set along the

x direction. Distributions of (7,6)-(7,5) peak separation ($\delta(x,y)$) were reconstructed from a series of measured strain data on a 41 x 41 point grid with 1 mm spacing. In total, 1681 fluorescence spectra were obtained by sequentially interrogating the SWCNTs at the grid points. We deduced strain values from the spectral peak separations and the strain sensitivity value γ= -1.4 $nm/m\epsilon$. Since the strain is measured from the peak separation, we construct a baseline (initial) strain map ϵ_{xx} by subtracting from each point the mean value, $\overline{\delta_0(x,y)} = \frac{1}{N}\sum_x\sum_y \delta_0(x,y)$ (N is the total number of measurements), of the original peak separation $\delta_0(x,y)$ at location (x,y). The strain at location (x,y) can be obtained by equation (5.3). The strain map is further reconstructed from the set of discrete grid point measurements by a bilinear interpolation algorithm.

$$\begin{aligned}\epsilon(x,y) &= \epsilon_0(x,y) - (\delta(x,y) - \overline{\delta_0(x,y)})/\gamma \\ &= \epsilon_0(x,y) - (\Delta\lambda_{(7,6)}(x,y) - \Delta\lambda_{(7,5)}(x,y))/\gamma\end{aligned} \tag{5.3}$$

Here $\epsilon_0(x,y)$ is the initial strain before loading measured at a calibration reference strain gage, $\delta(x,y)$ is the peak separation after each increment of loading, $\overline{\delta_0(x,y)}$ is the mean value of the original peak separation $\delta_0(x,y)$, γ is the strain sensitivity, $\Delta\lambda_{(7,5)}(x,y)$ and $\Delta\lambda_{(7,5)}(x,y)$ are the peak position changes for (7,5) and (7,6) SWCNTs (see Figure 5.3), respectively. A calibration strain gage is chosen in advance to represent the strain at a reference point away from the stress/strain concentration region, where the strain variation is minimal.

5.2.2 Case Studies

An S^4 reader head incorporating a small diode laser is mounted on a 3D printer. The tracking and control system enables accurate positioning and measurement. Com-

puter program moves the read head to the desired x,y-coordinates and z-coordinate (for proper optical distance from the specimen surface) with a spatial resolution of less than 0.1 mm. This S^4 automation system can be used to move the optical read head to any position or orientation on test specimens precisely in order to measure strain maps. In this study, the wavelength of the exciting laser is set at about 660 nm. Optical components, such as filters, half-wave plate and lenses are firstly used to filter, polarize and focus the laser. The SWCNT fluorescence emissions are then collected and transmitted to a spectrometer for measuring the NIR spectra. 2D strain sensing is performed by obtaining the fluorescence spectrum at a series of positions and by interpolating the measured strain data knowing the geometric information of the interrogated spots. Six study cases are investigated in this research: the first two is a pre-holed aluminum bar and a pre-notched aluminum bar and the other two is a pre-holed copper bar and a pre-notched copper bar. The details are shown in Table 5.1.

5.3 Case Study 1: Strain Analysis on Pre-holed Aluminum Specimen 1

5.3.1 Experiment

The dimension of the pre-holed aluminum bar is 2 in x 12 in x 0.25 in and the diameter of the central hole of 6.35 mm (0.25 inch). The newly designed S^4 film is applied on the front side of the bar and 4 channels of strain gages are attached to the back side of the bars as shown in Figure 5.5 (right). If the center of the hole is set as the origin of a cartesian coordinate system with x axis along the length of the bar and y axis along the width, the coordinates of the strain gages are (0, 10 mm) for gage 1, (0,

Table 5.1 : Pre-damaged metallic specimens.

Case Study	S^4 film composition	Pre-designed damage	Load-unload cycles
1. Al Hole 1	SWCNTs-PFO + PU[1]	central circular hole, $d = 6.35\,mm$	4 cycles, 10,12,16,18 kip
2. Al Notch 1	SWCNTs-PFO + PU[2]	edged rectangular notch, $l = 15.4mm, w = 1.3\,mm$	2 cycles, 8,12 kip
3. Al Hole 2	SWCNTs-PFO + PU[2]	central circular hole, $d = 6.35\,mm$	1 cycle, 19 kip
4. Cu Hole 1	SWCNTs-PFO + PU[1]	central circular hole, $d = 6.35\,mm$	3 cycle, 8, 12, 16 kip
5. Cu Hole 2	SWCNTs-PFO + PU[2]	central circular hole, $d = 6.35\,mm$	1 cycle, 15.2 kip
6. Cu Notch 1	SWCNTs-PFO + PU[2]	edged rectangular notch, $l = 15.4mm, w = 1.3\,mm$	1 cycle, 9.5 kip

[1] AkzoNobel® polyurethane;

[2] Minwax® fast-drying polyurethane.

-10 mm) for gage 2, (-10 mm, 0) for gages 3 and 4. Strain gages 1-3 are along the x direction, while strain gage 4 is along the y direction. The purposes of attaching the strain gauges are: (1) to monitor the strain condition during the mechanical loading; (2) to compare to the S^4 measurements; (3) to update the finite element models, which are used to validate S^4 film sensor.

The specimen coated with S^4 film is stretched by MTS hydraulic testing system as shown in Figure 5.6a. An axial load is applied on the specimen along its length and is increased/decreased gradually at a fixed rate. After each loading or unloading process, the grip is set to hold for several minutes to allow the redistribution of strain

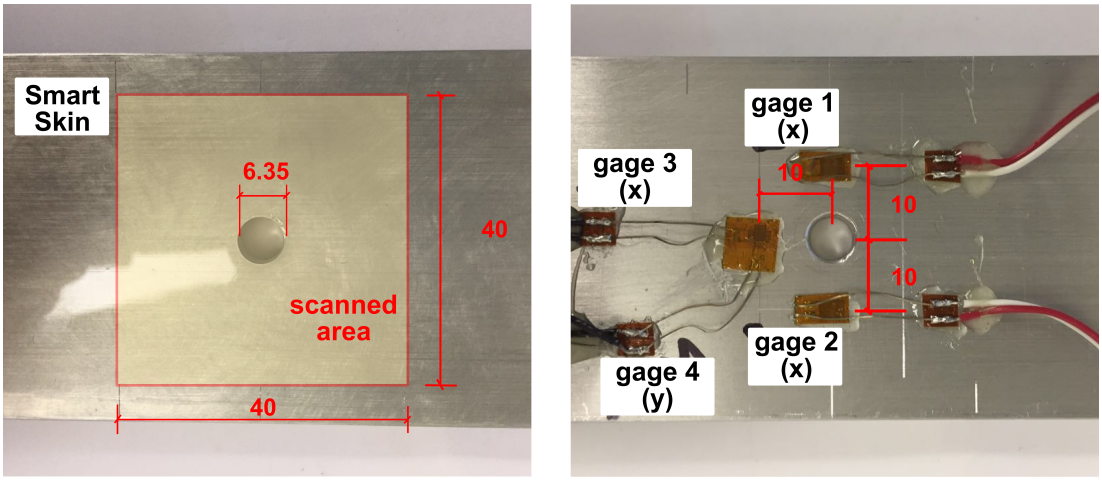

Figure 5.5 : Photos of (left) smart skin on the front and (right) strain gauges on the back of an aluminum bar (unit: mm).

on the specimens. The axial force is applied in 4 load-unload cycles with peak values of 10 kip, 12 kip, 16 kip and 18 kip, respectively. In the process, strain histories measured by strain gauges are monitored to capture the residual strain that occurred in the bar. As shown in Figure 5.7, in the first two load/unload cycles, most of the material is still within the linear elastic range. While after the third unloading process of 16 kip, the material near strain gage 1-3 begins generating residual strain. During the fourth loading process of 18 kip, the yielding condition near strain gage 1 and strain gage 2 becomes more observable with nonlinear features of the strain history curve (Figure 5.7). Since the locations of strain gage 1 and 2 are symmetric with the center, the measured strain are almost the same.

Before and after the mechanical test, 2D S^4 strain scans are performed within a square area of 40 mm by 40 mm (shown in Figure 5.8) around the hole and the polarization of laser excitation is set along x direction. Distributions of (7,6)-(7,5) peak separation are reconstructed by using a series of measured strain data on a

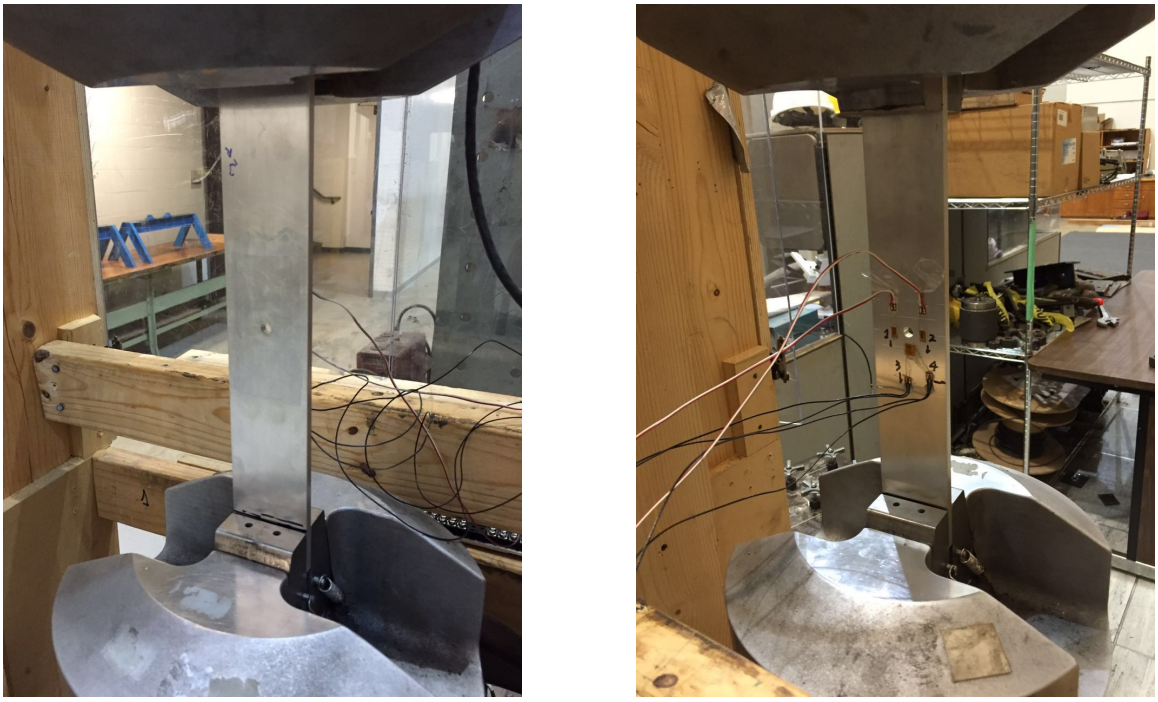

(a) Front (b) Back

Figure 5.6 : Photos of a pre-holed aluminum bar mounted on a MTS machine.

rectangular grid of 41 x 41. In total, 1681 fluorescence spectrum are obtained by sequentially interrogating the SWCNTs at each spot of the grid intersections. By using the peak separation distribution, strain distribution is calculated. The mapped strain contour ϵ_{xx} before the mechanical test is shown in Figure 5.9. The variation in strain measurement is due to the strain condition different of the SWCNTs embedded in polymers during the material fabrication process of S^4 film.

The residual strain distribution ϵ_{xx} measured by S^4 sensor on pre-holed specimen after load-unload cycle 16 kip and 18 kip are shown in Figure 5.10a and Figure 5.10b, respectively. We can observe interesting patterns in the strain contours caused by the structural discontinuity (the hole). Both the maximum strain and the size of

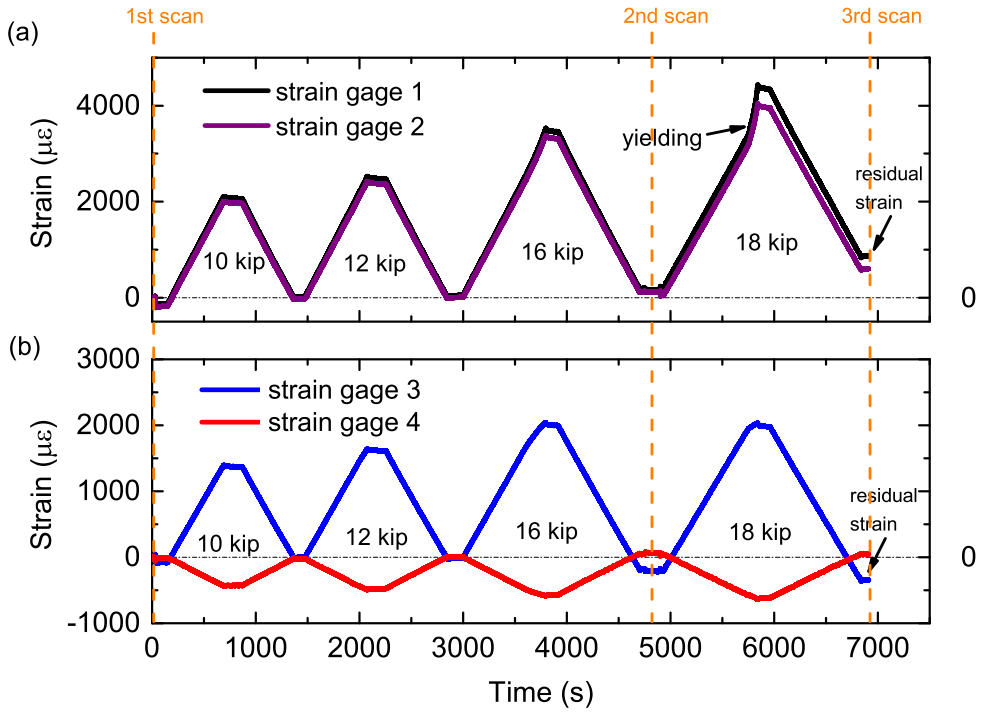

Figure 5.7 : Time history of measured strain by strain gages under load/unload cycles of 10 kip, 12 kip, 16 kip and 18 kip. The 1st S^4 scan is performed at the beginning of the experiment, the 2nd S^4 scan is performed after the specimen is unloaded completely from 16 kip to 0, and the 3rd S^4 scan is performed after the specimen is unloaded completely from 18 kip to 0.

the lobes (near the hole) increases with the increase of the load from 16 kip to 18 kip. The specimen is released completely from the MTS hydraulic machine before the specimen is subjected to strain scanning. The residual strain created on the specimen after releasing the load completely includes the residual plastic deformation of the material near the hole. This will be presented along with the FEA validation in a later section in this Chapter.

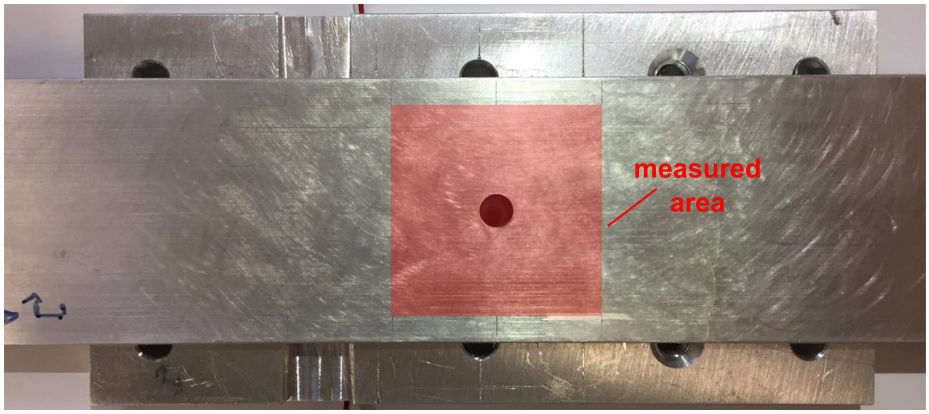

Figure 5.8 : Aluminum pre-holed bar after loading (Note the elongated hole along the x direction).

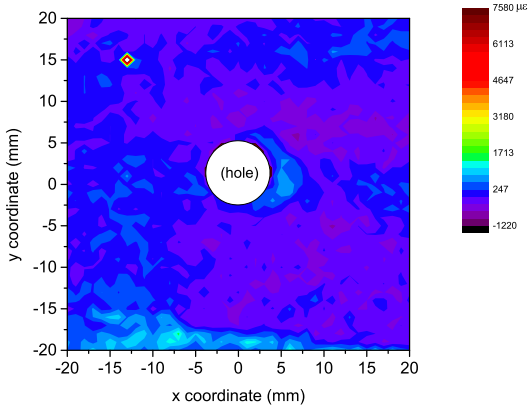

Figure 5.9 : Strain distribution ϵ_{xx} measured by S^4 sensor under intact condition.

5.3.2 Theoretical Study

Figure 5.11 shows the sketch of a rectangular bar with central hole with radius a. The governing equations of elasticity can be derived and the closed-form solution of the stress field in cylindrical- polar coordinate system is given by equations (5.4) [49].

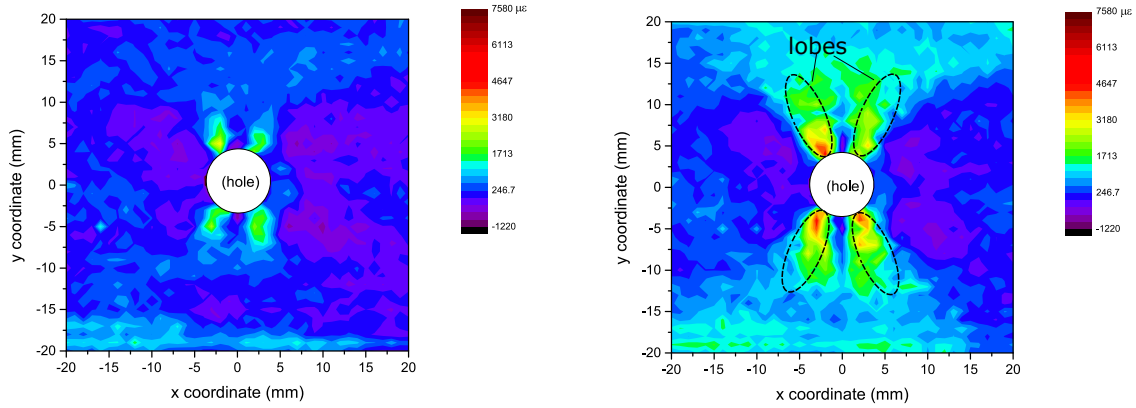

(a) after 16 kip (b) after 18 kip

Figure 5.10 : Residual strain distribution ϵ_{xx} measured by S^4 sensor on a pre-holed specimen after load-unload cycles.

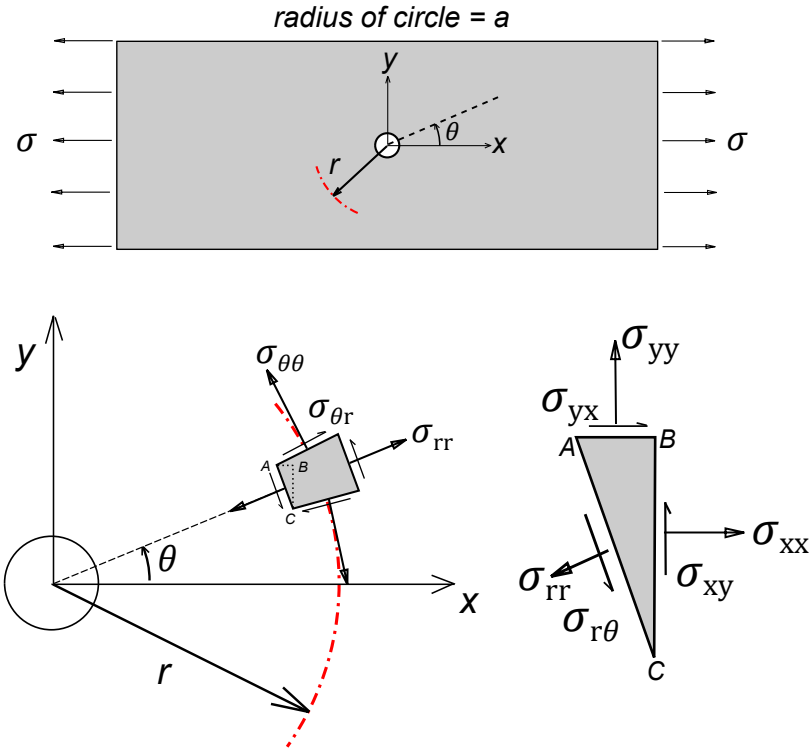

Figure 5.11 : Bar with central circular hole with radius = a.

$$\begin{aligned}
\sigma_{rr} &= \frac{\sigma}{2}\left[(1-{a_r}^2)+(1-4{a_r}^2+3{a_r}^4)\cos 2\theta\right] \\
\sigma_{\theta\theta} &= \frac{\sigma}{2}\left[(1+{a_r}^2)-(1+3{a_r}^4)\cos 2\theta\right] \\
\sigma_{\theta r} &= -\frac{\sigma}{2}\left[(1+2{a_r}^2-3{a_r}^4)\sin 2\theta\right] \\
\sigma_{zz} &= \sigma_{zr} = \sigma_{z\theta} = 0
\end{aligned} \tag{5.4}$$

where σ is the applied stress and a_r is the ratio of a to r, $a_r = a/r$.

Using the stress field in equation (5.4), the strain field can be obtained in equation (5.5)

$$\begin{aligned}
\epsilon_{rr} &= \frac{1}{E}(\sigma_{rr} - \nu\sigma_{\theta\theta}) \\
\epsilon_{\theta\theta} &= \frac{1}{E}(\sigma_{\theta\theta} - \nu\sigma_{rr}) \\
\epsilon_{\theta r} &= \frac{1}{2G}\sigma_{\theta r} = \frac{1+\nu}{E}\sigma_{\theta r} \\
\epsilon_{zz} &= -\frac{\nu}{E}(\sigma_{\theta\theta} + \sigma_{rr}) \\
\epsilon_{zr} &= \epsilon_{z\theta} = 0
\end{aligned} \tag{5.5}$$

Hence, the strain field can be represented by the equations (5.6)

$$\begin{aligned}
\epsilon_{rr} &= \frac{\sigma}{2E}\{\left[(1-\nu)-(1+\nu){a_r}^2\right]+\left[(1+\nu)-4{a_r}^2+3(1+\nu){a_r}^4\right]\cos 2\theta\} \\
\epsilon_{\theta\theta} &= \frac{\sigma}{2E}\{\left[(1-\nu)-(1+\nu){a_r}^2\right]+\left[-(1+\nu)+4\nu{a_r}^2-3(1+\nu){a_r}^4\right]\cos 2\theta\} \\
\epsilon_{\theta r} &= -\frac{(1+\nu)\sigma}{2E}\left(1+2{a_r}^2-3{a_r}^4\right)\sin 2\theta \\
\epsilon_{zr} &= \epsilon_{z\theta} = 0
\end{aligned} \tag{5.6}$$

Stress and strain are both tensors and can be transformed from one coordinate system to another. In Figure 5.11 the connection between the stresses in cylindrical-

polar coordinate system and Cartesian coordinate system is presented. Let S be a tensor, with components in the two different coordinate systems as shown below

$$S_{xyz} = \begin{bmatrix} S_{xx} & S_{xy} & S_{xz} \\ S_{yx} & S_{yy} & S_{yz} \\ S_{zx} & S_{zy} & S_{zz} \end{bmatrix} \tag{5.7}$$

$$S_{r\theta z} = \begin{bmatrix} S_{rr} & S_{r\theta} & S_{rz} \\ S_{\theta x} & S_{\theta y} & S_{\theta z} \\ S_{zr} & S_{z\theta} & S_{zz} \end{bmatrix} \tag{5.8}$$

In the cylindrical-polar basis $\{e_r, e, e_z\}$ and in the Cartesian basis $\{e_i, e_j, e_k\}$, respectively, the two are related by equation (5.9).

$$S_{xyz} = Q^T S_{r\theta z} Q \tag{5.9}$$

where $Q = \begin{bmatrix} \cos\theta & \sin\theta & 0 \\ -\sin\theta & \cos\theta & 0 \\ 0 & 0 & 1 \end{bmatrix}$ for a two dimensional plain stress problem.

Hence, we can get the stress in Cartesian basis as shown in equation (5.10):

$$\begin{aligned} \sigma_{xx} &= \cos^2\theta\sigma_{rr} + \sin^2\theta\sigma_{\theta\theta} - \sin 2\theta\sigma_{r\theta} \\ \sigma_{yy} &= \sin^2\theta\sigma_{rr} + \cos^2\theta\sigma_{\theta\theta} + \sin 2\theta\sigma_{r\theta} \\ \sigma_{xy} &= \frac{1}{2}\sin 2\theta\sigma_{rr} - \frac{1}{2}\sin 2\theta\sigma_{\theta\theta} + \cos 2\theta\sigma_{r\theta} \\ \sigma_{zz} &= \sigma_{zx} = \sigma_{zy} = 0 \end{aligned} \tag{5.10}$$

Further, the closed-form solution of strain fields can be obtained in equation (5.11) for plain stress condition.

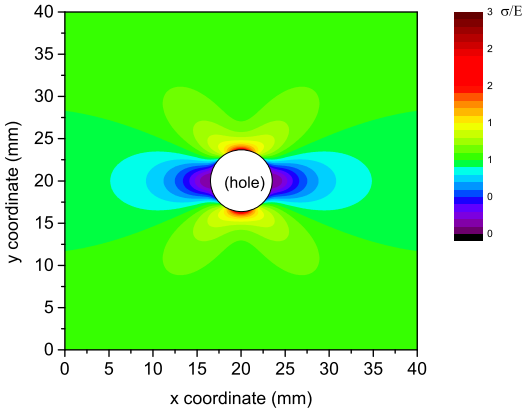

Figure 5.12 : ϵ_{xx} distribution calculated using elasticity (unit: $\frac{\sigma}{E}$).

$$
\begin{aligned}
\epsilon_{xx} &= \frac{1}{E}(\sigma_{xx} - \nu\sigma_{yy}) \\
\epsilon_{yy} &= \frac{1}{E}(\sigma_{yy} - \nu\sigma_{xx}) \\
\epsilon_{\theta r} &= \frac{1}{2G}\sigma_{xy} = \frac{1+\nu}{E}\sigma_{xy} \\
\epsilon_{zz} &= -\frac{\nu}{E}(\sigma_{xx} + \sigma_{yy}) \\
\epsilon_{zx} &= \epsilon_{zy} = 0
\end{aligned}
\tag{5.11}
$$

If the radius of the hole is set as 6.35 mm (0.25 in) and the width of the bar is 50.8 mm (2 in), the ϵ_{xx} distribution calculated using LEFM elasticity solution on the center square area of 40 mm x 40 mm is shown in Figure 5.12. The maximum value of ϵ_{xx} is 2.94 σ/E, in which 2.94 is the strain/stress concentration factor. By comparing the analytical strain field calculated by LEFM (in Figure 5.12) with the experimental plastic strain field measured by smart skin (in Figure 5.10b), we can find that the two do not match due to the strong assumptions adopted in the elasticity/LEFM calculation. The strong assumptions includes (1) plain stress problem and (2) the material is linear elastic during the testing. Hence, there is a need to perform FEM simulation

using elasto-plastic material to understand the complex strain/stress condition near the hole.

5.3.3 Finite Element Analysis

Table 5.2 : Material properties of aluminum alloy 6061. [3]

Parameters	Metric	English
Density, ρ	2700 kg/m^3	0.0975 lb/in^3
Modulus of Elasticity, E	68.9 GPa	10000 ksi
Poisson's Ratio(elastic), ν	0.33	0.33
Poisson's Ratio(plastic), ν'	0.50	0.50
Tensile Yield Strength, σ_y	276 MPa	40000 psi
Tensile Ultimate Strength, σ_u	310 MPa	45000 psi

Note: the material parameter above are for reference only.

FEA Models

The material model is set as isotropic hardening model in FEA performed using ANSYS [80]. As shown in Table 5.3, 8 models are built with different modal parameters. While linear property of stress-strain can be used for small-strain analyses, nonlinear stress-strain must be used for plasticity, as it is more representative measures of the state of the material. Model 1 is a 2D model with element type SHELL181 (ANSYS) and bilinear isotropic hardening material model. Model 2 and model 3 are 3D model built with element type SOLID185 (ANSYS) and isotropic hardening material model. While the rest of the models are 3D SOLID185 (ANSYS) and multilinear isotropic hardening material model using Ramberg-Osgood equation [81] (as shown

in equation(5.12)) as the stress-stress curve. n is the parameter to determine the degree of nonlinearity, larger n causes higher nonlinearity.

$$\epsilon = \frac{\sigma}{E} + 0.002(\frac{\sigma}{\sigma_y})^n \tag{5.12}$$

where ϵ is strain, σ is stress, E is Young's modulus, σ_y is yield stress. [81]

Table 5.3 : FEA models for pre-holed aluminum specimen.

Model No.	Element type	Material Model	Model parameter
1	2D SHELL181	Bilinear Isotropic Hardening	E_0, σ_{y0}, E_t
2	3D SOLID185	Bilinear Isotropic Hardening	E_0, σ_{y0}, E_t
3	3D SOLID185	Bilinear Isotropic Hardening	E_1, σ_{y1}, E_t
4	3D SOLID185	Multilinear Isotropic Hardening	$E_0, \sigma_{y0}, n = 20$
5	3D SOLID185	Multilinear Isotropic Hardening	$E_1, \sigma_{y0}, n = 20$
6	3D SOLID185	Multilinear Isotropic Hardening	$E_1, \sigma_{y1}, n = 20$
7	3D SOLID185	Multilinear Isotropic Hardening	$E_1, \sigma_{y1}, n = 10$
8	3D SOLID185	Multilinear Isotropic Hardening	$E_1, \sigma_{y1}, n = 30$

Note: $E_0 = 68.9\,GPa,\ \sigma_{y0} = 276\,MPa,\ E_t = 0.5\,GPa,\ E_1 = 75\,GPa,\ \sigma_{y1} = 300\,MPa$

The mechanical properties of aluminum alloy 6061 [3] is shown in Table 5.2. The material report states that the ultimate tensile strength is from 42.5 ksi to 46.2 ksi, and the yield strength is from 39.40 ksi to 43.60 ksi. Other source [82] shows the modulus of elasticity for aluminum alloy 6061 can vary from 70 GPa to 80 GPa. For the FEA simulations, we choose the material properties shown in Table 5.3 for different models.

The 2D and 3D FEM models and the geometry is exactly same as the one in

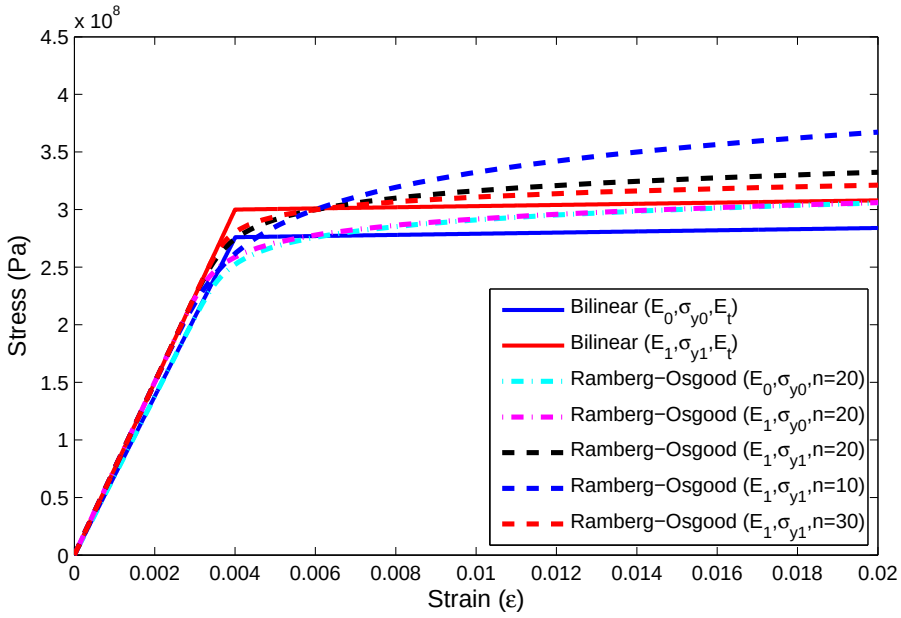

Figure 5.13 : Stress-strain curve models used in FEA.

the experiment. Mapped meshing technique is preferred over free mesh in our study, because: (1) Mapped mesh can control mesh pattern, good to mesh model with complex geometry, like hole or crack; can avoid irregular elements which would cause trouble in computational convergence; can make model symmetric. (2) To ensure the same accuracy of nonlinear mechanical simulation, mapped meshing method requires more elements than free meshing method for the aluminum bar with small hole in middle, saving half of the simulation time.

$$I_2 = \frac{1}{2}(\sigma_{ii}\sigma_{jj} - \sigma_{ij}\sigma_{ji}) \tag{5.13}$$

where I_2 is the second deviatoric stress invariant, σ_{ij} is the stress component.

In the FEA setting of this study, von Mises yield criterion is adopted to decide when the material yields. The von Mises yield criterion suggests that the yielding

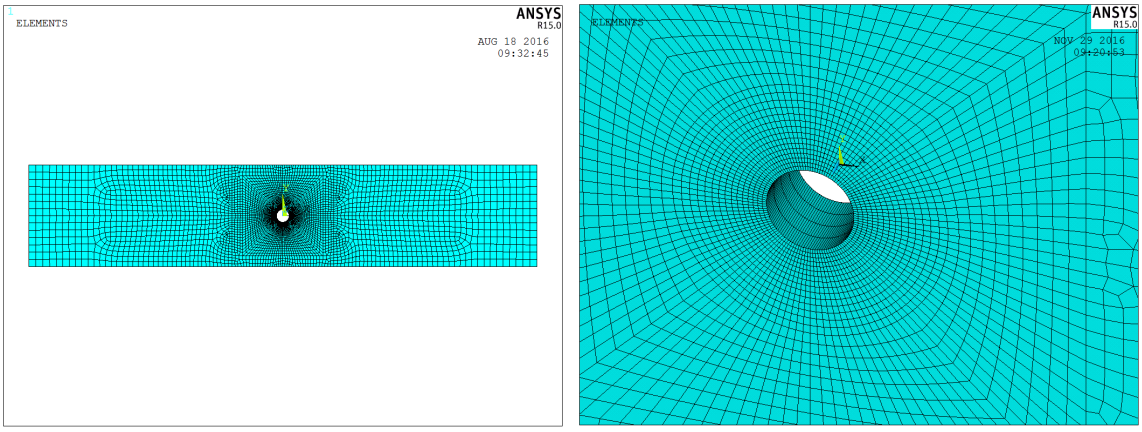

(a) 2D(4984 elements) (b) 3D(19936 elements)

Figure 5.14 : FEA models with mapped mesh grid.

of materials begins when the second deviatoric stress invariant I_2 (as shown in equation 5.13) reaches a critical value $\sigma_y^2/3$ — a plasticity theory that applies best to ductile materials, such as metals. Prior to yield, material response is assumed to be elastic. ν is the effective Poisson's ratio. In ANSYS software setting [80], during elastic region, we use $\nu = 0.33$, during plastic region, we use $\nu = 0.50$. In reality, as the deformation regime changes from elastic to plastic, Poisson's ratio changes gradually depending on the true stress condition [59].

Strain Time History

Only during the 16 kip and 18 kip load-unload cycles in the experiment, the residual strain is detected by using strain gages. Hence, only 16 kip and 18 kip cycles (the last two cyles) of load-unload processes is simulated on the FEA models to save time and effort. Since strain gage 1(g1) strain gage 2(g2) are in the symmetric positions with the center of the bar, the averaged value of the measured strain in Figure 5.7 is

used and compared to the simulated results from model 1-3. For the first 3 models, $E = E_0 = 68.9\,GPa$, $\sigma_y = \sigma_{y0} = 276\,MPa$.

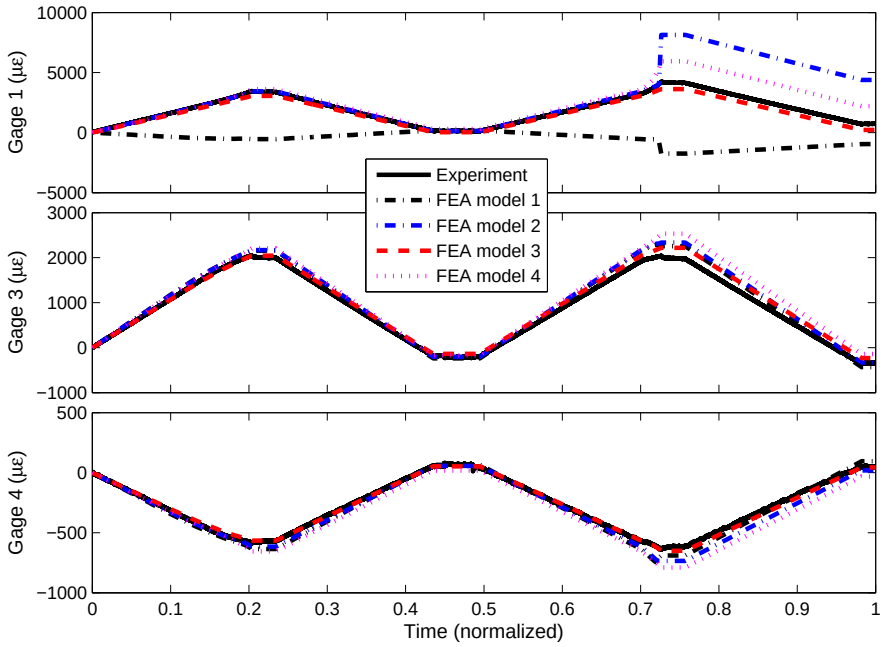

Figure 5.15 : Strain history of experiment and FEA models 1-3.

As shown in Figure 5.15, the model 1 with 2D element does not match the experimental results. This is due to the complex strain conditions near the edge of the hole, near the edge of the hole the plain-stress assumption is not valid any more. Hence, 2D element is not suitable for our study. Once the 3D element is used in model 2, the strain history curves are closer to the experimental ones. Compared to model 2, model 3 adopts Ramberg-Osgood equation (n=20) for creating the multi-linear isotropic hardening material model rather than bilinear model. Model 3 shows a closer match with reduced plastic strain at g1. However, the strain history at g1 for model 3 is still larger than the experimental one during 18 kip load-unload cycle. Parameters such as E, σ_y and n need to be updated in the models to match the real

situation of the experiment.

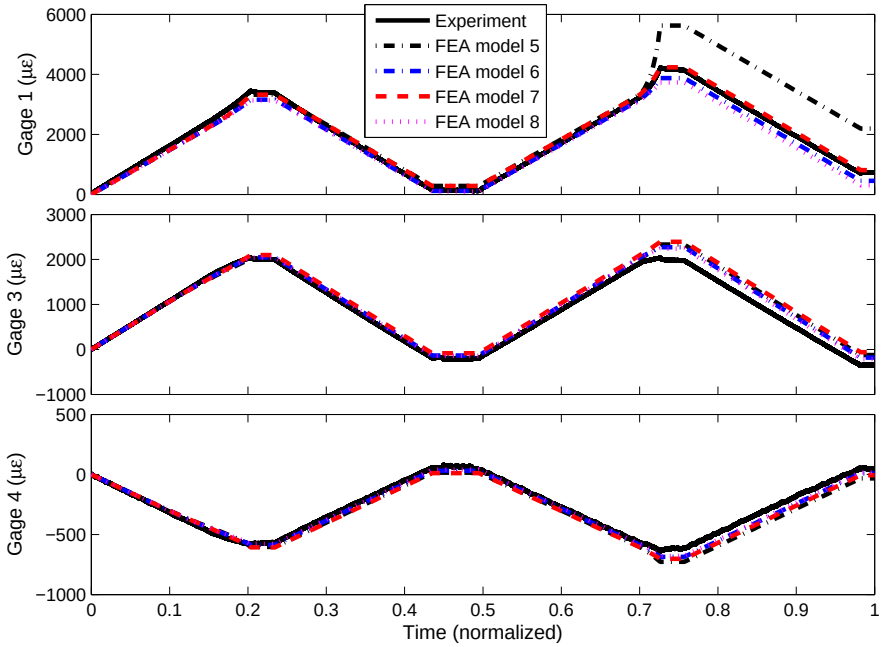

Figure 5.16 : Strain history of experiment and FEA models 5-8.

Figure 5.16 shows the FEA models with updated parameters. Among the models 5-8, the strain history pattern of model 7 matches that of strain gage measurements the best. In model 7, $E = E_1 = 75\,GPa$, $\sigma_y = \sigma_{y1} = 300\,MPa$ and $n = 10$.

2D Strain Contour

The residual strain field ϵ_{xx} from model 1-4 are shown in Figure 5.17. Considerable difference can be observed between 2D model and 3D models. The strain distribution patterns from 3D models look similar with "butterfly" shape in strain contours ϵ_{xx} as shown in Figure 5.18.

With the same Young's modulus and yielding stress in FEA program setting, the "butterfly wing" tips of the strain maps are becoming rounder, when the stress-

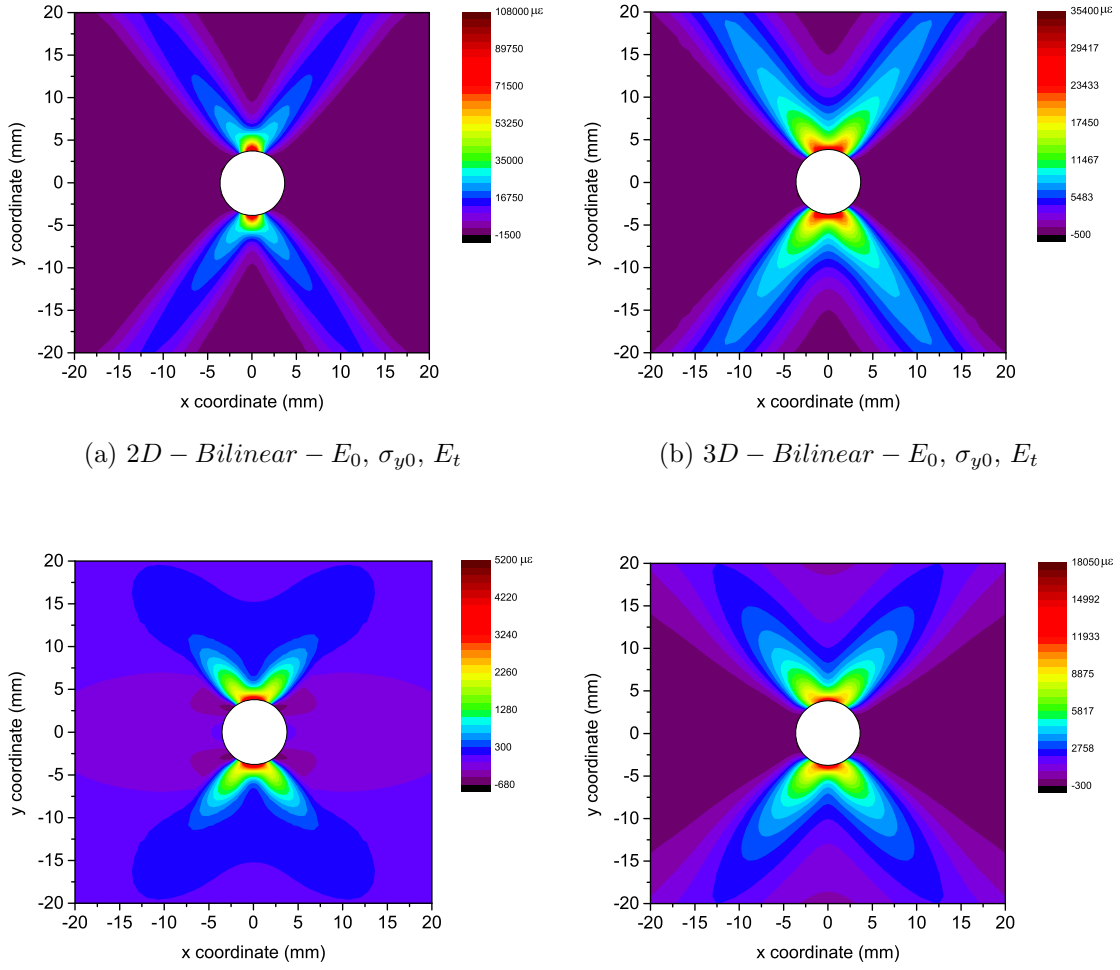

(a) $2D - Bilinear - E_0$, σ_{y0}, E_t

(b) $3D - Bilinear - E_0$, σ_{y0}, E_t

(c) $3D - Bilinear - E_1$, σ_{y1}, E_t

(d) $3D - Multilinear - E_0$, σ_{y0}, $n = 20$

Figure 5.17 : Residual strain distribution ϵ_{xx} of FEA models (a) model 1 (b) model 2 (c) model 3 (d) model 4 after load-unload process.

strain curve is changing from bilinear model to multilinear one using Ramberg-Osgood equation. The maximum value of residual strain ϵ_{xx} decreases with the increasing Young's modulus and yielding stress.

As shown in Figure 5.18, the details of the strain contours also change with the different Ramberg-Osgood parameter n. Since the FEA in this study is elasto-plastic,

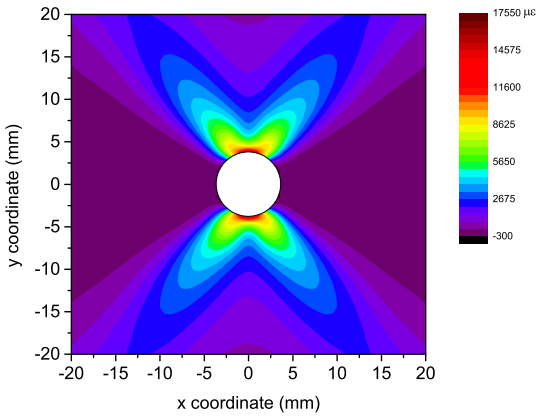

(a) $3D - Multilinear - E_1$, σ_{y0}, $n = 20$

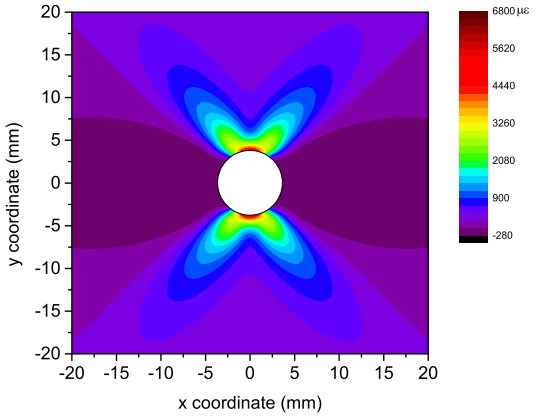

(b) $3D - Multilinear - E_1$, σ_{y1}, $n = 20$

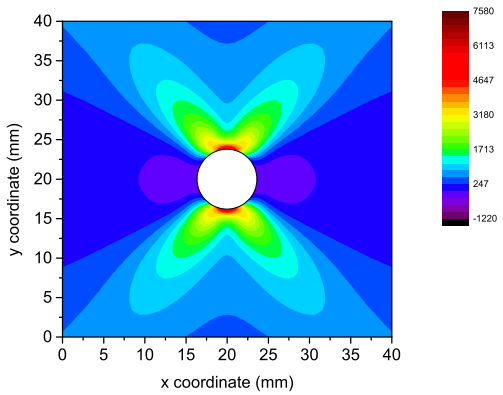

(c) $3D - Multilinear - E_1$, σ_{y1}, $n = 10$

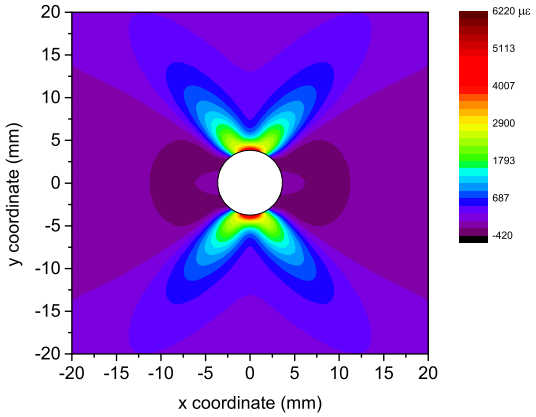

(d) $3D - Multilinear - E_1$, σ_{y1}, $n = 30$

Figure 5.18 : Residual strain distribution ϵ_{xx} of FEA models (a) model 5 (b) model 6 (c) model 7 (d) model 8 after load-unload process.

the strain patterns/results are complicated and sensitive to many parameters, such as load history, material nonlinearity, Poisson's ratio and so on. The further investigation of the optimization of these parameters is beyond the scope of this study.

5.3.4 Discussion

The detailed comparison of residual strain map ϵ_{xx} measured by S^4 and the one simulated by FEA model 7 is shown in Figure 5.19; the scale bars have been tuned to the same (from -1220 $\mu\epsilon$ to 7580 $\mu\epsilon$). Some strain near the edge of the hole is shown as while color in Figure 5.19 (right), because the strain in the FEA exceeds the maximum limit of the scale bar.

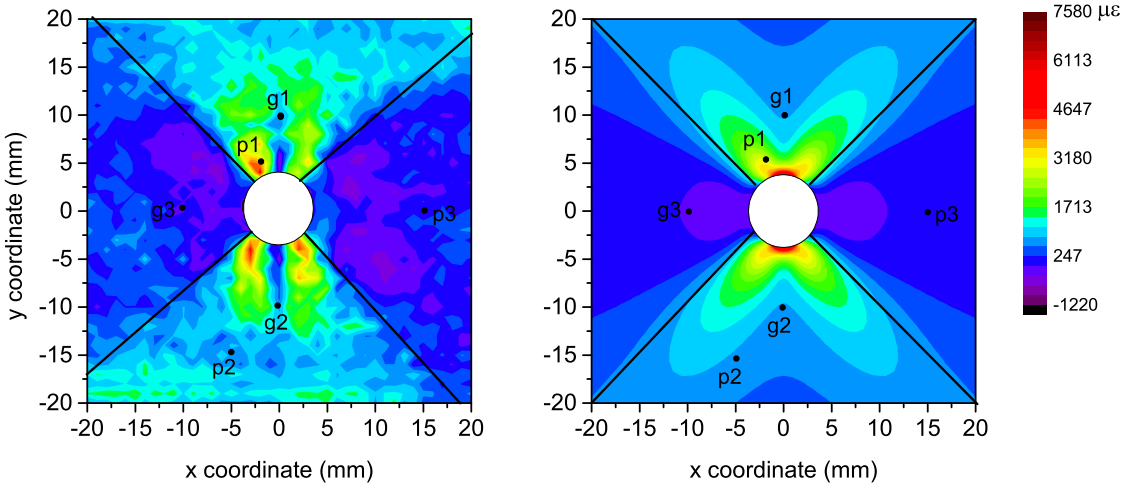

Figure 5.19 : S^4 experimental (left) and FEA simulated (right) residual strain maps of ϵ_{xx}. The simulation used model 7. Both maps are plotted with the same color scale for strain levels.

Solid lines are plotted on the two contours to separate the area under tension and compression. The patterns in the strain distributions of S^4 measurement match well with the FEA simulation. 6 different locations on the strain maps are compared quantitatively and the location and the results are shown in Table 5.4. At g1 and g2, the three sets of data from strain gages, S^4 film and FEA match well. At p1 and P2, the S^4 measurements are close to the FEA results. It should be noted that this is a

Table 5.4 : Residual strain ϵ_{xx} measured on the pre-holed bar by strain gages, S^4 and FEA model 7.

Point	Location (mm)	Strain gage ($\mu\epsilon$)	S^4 ($\mu\epsilon$)	FEA ($\mu\epsilon$)
g1	(0, 10)	782	716	802
g2	(0, -10)	777	687	804
g3	(-10, 0)	-340	-67	-60
p1	(-2, 5)	-	3994	3118
p2	(-5, -15)	-	745	711
p3	(15, 0)	-	3	58

elasto-plastic study, and the accuracy of measurements and FEA simulation depends on many parameters.

5.4 Case Study 2: Strain Analysis on Pre-notched Aluminum Specimen 1

5.4.1 Experiment

The dimensions of the pre-notched aluminum bar are 2 in x 12 in x 0.25 in and the size of the edged notch is set that length=15.4 mm, width=1.3 mm. The newly designed S^4 film is applied on the front side of the bar and 4 channels of strain gages are attached to the back side of the bars as shown in Figure 5.20.

If the center of the bar is set as the origin of a cartesian coordinate system with x axis along the length of the bar and y axis along the width, the coordinates of the strain gages are (-40 mm, 0) for gage 1, (0, 0) for gage 2-4. Strain gages 1-2 are along the x direction, while strain gage 4 is along the y direction and strain gage 3 is along

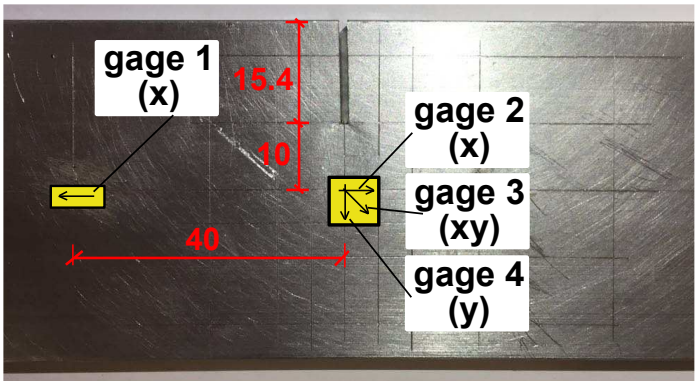

Figure 5.20 : Photo of strain gauges on the back of the pre-cracked aluminum bar (unit: mm).

the 45^o between x and y axis. The purpose of attaching the strain gauges are: (1) to monitor the strain condition during the mechanical test; (2) to compare to the S^4 measurements; (3) to update the finite element models used to validate S^4 film sensor.

The specimen coated with S^4 film is stretched by MTS hydraulic testing machine as shown in Figure 5.21b. An axial load is applied along the length of the bar (x direction) and is increased/decreased gradually at a fixed rate. After each loading or unloading process, the grip is set to hold for several minutes to allow the strain to redistribute on the specimen. The axial force is applied in 2 load-unload cycles with peak values of 8 kip and 12 kip, respectively, as shown in Figure 5.22. In the process, strain histories measured by strain gauges are monitored to capture the residual strain that occurs in the bar.

As shown in Figure 5.22, in the first 8 kip load/unload cycle, most of the material is still within the linear elastic range. While during 12 kip load process, the material near the strain rosette begins generating residual strain with observable nonlinear features as indicated in Figure 5.22.

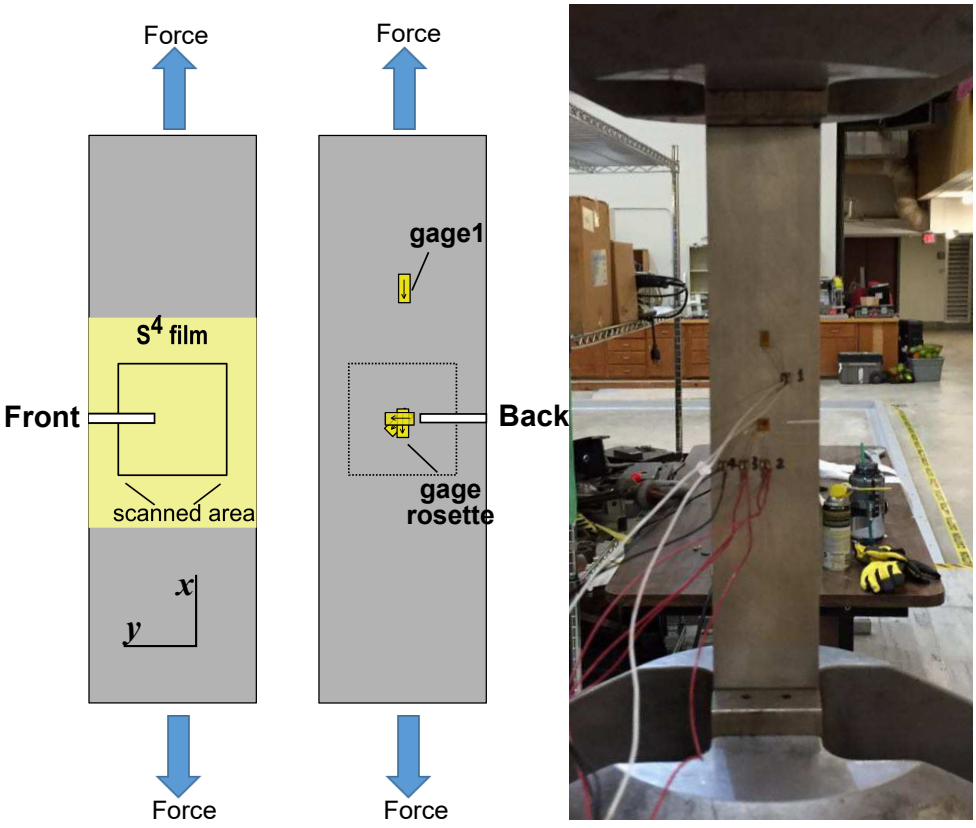

(a) Sketch (b) Photo

Figure 5.21 : An aluminum pre-cracked specimen mounted on a MTS machine.

Before and after the mechanical test, 2D S^4 strain scans are performed within a square area of 40 mm by 40 mm near the crack with the polarization of laser excitation along x direction (stretching direction). Distribution of (7,6)-(7,5) peak separation are reconstructed by using a series of measured strain data on a rectangular grid of 41 x 41. In total, 1681 fluorescence spectrum are obtain by sequentially interrogating the SWCNTs at each spot of the grid intersections. By using the peak separation distribution, strain distribution is computed. The mapped strain contour ϵ_{xx} before the mechanical test is shown in Figure 5.24a. The variation in strain measurement is

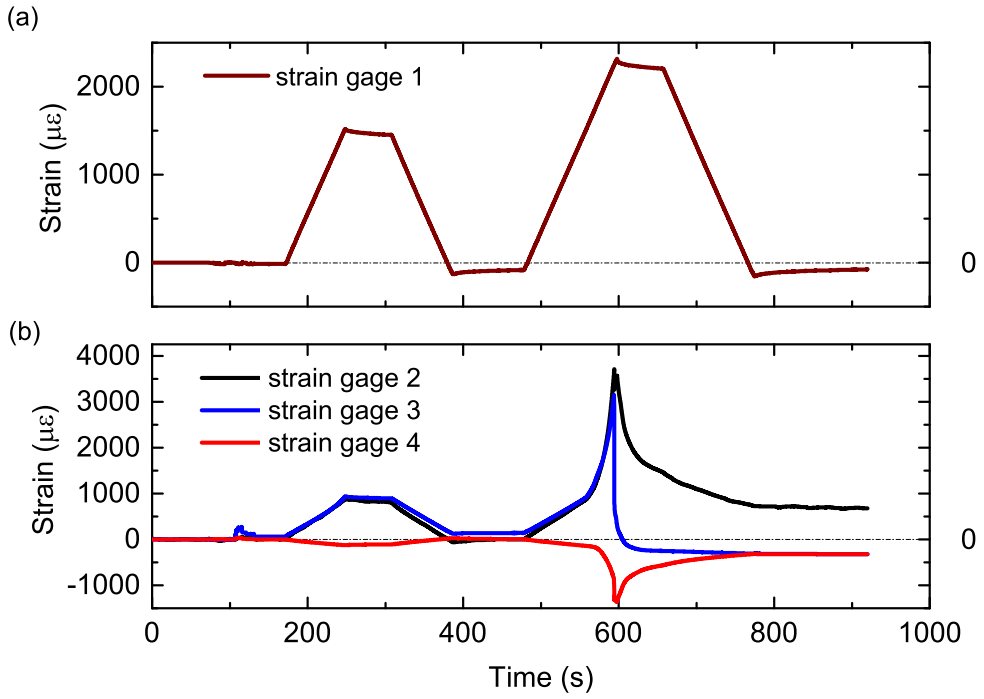

Figure 5.22 : Time history of measured strain on aluminum specimen 1 under load cycles of 8 kip, 12 kip.

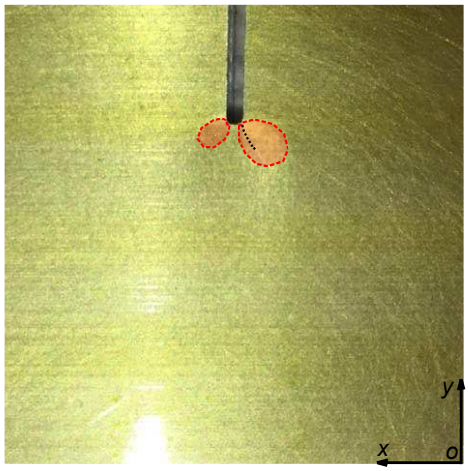

Figure 5.23 : Close view of S^4 film on aluminum specimen after load-unload process.

due to the strain condition different of the SWCNTs embedded in polymers during the material fabrication process of S^4 film.

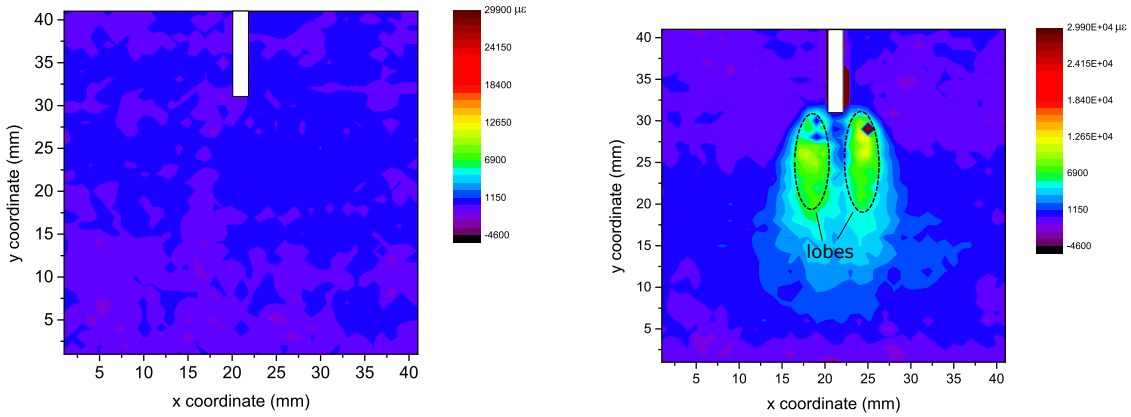

(a) unstressed (b) stressed

Figure 5.24 : Residual strain distribution ϵ_{xx} measured by S^4 sensor on pre-notched specimen.

The residual strain distribution ϵ_{xx} measured by S^4 sensor on pre-notched specimen after load-unload cycle 8 kip and 12 kip is shown in Figure 5.24b. We can observe interesting patterns in the strain contours caused by the structural discontinuity (the notch). The specimen has been released completely from the MTS hydraulic machine before the specimen is subjected to strain scanning.

5.4.2 Theoretical Study

Stress concentration is the localization of high stresses which is mainly due to discontinuities in continuum, abrupt changes in cross section and due to contact stresses. To study the effect of stress concentration and magnitude of localized stresses, a dimensionless factor called stress concentration factor K_t is defined by the equation

(5.14):

$$K_t = \sigma_{max}/\sigma \tag{5.14}$$

where σ is the uniform stress applied at the ends of the bar, and σ_{max} is the maximum stress at the tip of the discontinuities. Although the exact formulas vary according to the form of the crack (or the size of hole), in all cases K_t increases with an increase in the crack length a and a decrease in the root radius ρ at the crack tip [59]. Stress in a solid body is a tensor field. In addition to producing a stress concentration, a notch produces a local situation of biaxial or triaxial stress. For example, in the case of a bar containing a circular hole and subject to an axial force, there exist radial as well as tangential stresses [59]. Numerous brittle fractures have occurred in service, and there are abundant examples of them in great variety of structural and mechanical engineering fields involving ships, bridges, pressure vessels, oil ducts, turbines, and so on. In view of the great importance of brittle fracture in real life, the discipline called linear elastic fracture mechanics (LEFM) has emerged, enabling one to obtain a quantitative measure of the resistance of a brittle material to crack propagation. Extension of these efforts into nonlinear elastic and plastic regimes has led to the development of elasto-plastic fracture mechanics (EPFM) [59] EPFM is more close to the practical situations we normally encounter, because LEFM has many strong assumptions. However, in this study EPFM is beyond the scope of the study and LEFM will be used to provide an explicit closed-form solution for elastic cases.

There are three modes of loading cases in fractures [59]: (I) opening mode, (II) sliding mode, (III) tearing mode. To investigate the influence of notch on strain distribution, we are studying the Mode I crack load condition: the opening mode under axial load of the three modes of fracture. In spite of ignorance of the exact nature

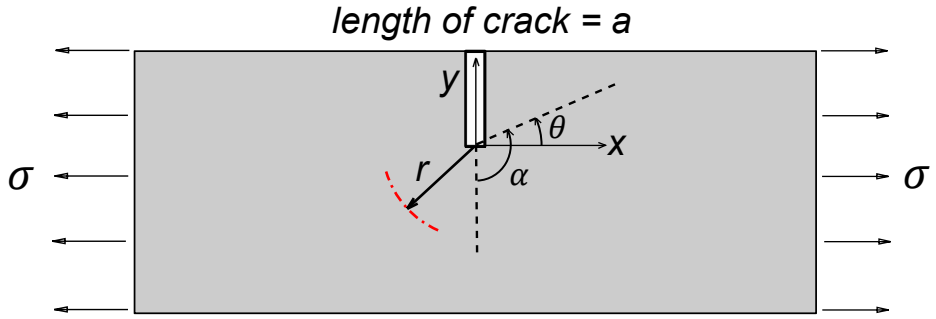

Figure 5.25 : Bar with edged crack, length = a

of the plastic zone, the LEFM treatment is valid for low stresses such that the size of the plastic zone at the crack tip is small with respect to the crack length and the dimensions of the sample. In this study, obtaining the strain field and plastic zone shape is of greater interest than the plastic stress around crack-tip area, a correction term for the presence of a plastic zone at the crack tip is not incorporated. In materials under loading conditions, there is a competition between flow (driven by shear stresses) and cleavage (driven by normal stresses), the outcome of which influences the stress intensity at the crack tip and the strain/stress distribution around the key spots [83].

In the Cartesian basis $\{e_i, e_j, e_k\}$, we can get the strain in Cartesian basis as shown in equation 5.15.

$$\begin{aligned}
\sigma_{xx} &= \frac{K}{\sqrt{2\pi r}} \cos\frac{\alpha}{2}(1 + \sin\frac{\alpha}{2}\sin\frac{3\alpha}{2}) \\
\sigma_{yy} &= \frac{K}{\sqrt{2\pi r}} \cos\frac{\alpha}{2}(1 + \sin\frac{\alpha}{2}\sin\frac{3\alpha}{2}) \\
\sigma_{xy} &= \frac{1}{2}\sin 2\theta\sigma_{rr} - \frac{1}{2}\sin 2\theta\sigma_{\theta\theta} + \cos 2\theta\sigma_{r\theta} \\
\sigma_{zz} &= \sigma_{zx} = \sigma_{zy} = 0
\end{aligned} \tag{5.15}$$

where $\alpha = \frac{\pi}{2} + \theta$.

Figure 5.25 shows the sketch of a rectangular bar with edge crack with length a. Using equation (5.15), we can derive the strain solution as shown in equation (5.16). And the strain field of ϵ_{xx} is plotted in Figure 5.26.

$$\begin{aligned}
\epsilon_{xx} &= \frac{1}{E}(\sigma_{xx} - \nu\sigma_{yy} - \nu\sigma_{zz}) \\
\epsilon_{yy} &= \frac{1}{E}(\sigma_{yy} - \nu\sigma_{xx} - \nu\sigma_{zz}) \\
\epsilon_{xy} &= \frac{1}{2G}\sigma_{xy} = \frac{1+\nu}{E}\sigma_{xy} \\
\epsilon_{zz} &= -\frac{\nu}{E}(\sigma_{xx} + \sigma_{yy}) \\
\epsilon_{zx} &= \epsilon_{zy} = 0
\end{aligned} \tag{5.16}$$

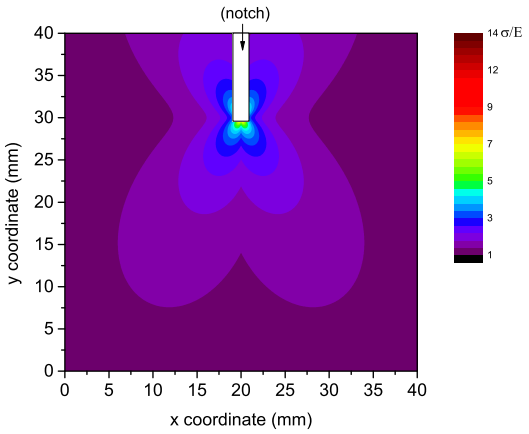

Figure 5.26 : ϵ_{xx} distribution calculated using LEFM (unit: $\frac{\sigma}{E}$).

5.4.3 Finite Element Analysis

In total, 8 FEA models are built using parameters as shown in Table 5.2 and Table 5.3. The 2D and 3D FEM models and the geometry is exactly same as the one in the experiment. The 2D and 3D meshed FEA model are shown in Figure 5.27a and Figure 5.27b, respectively.

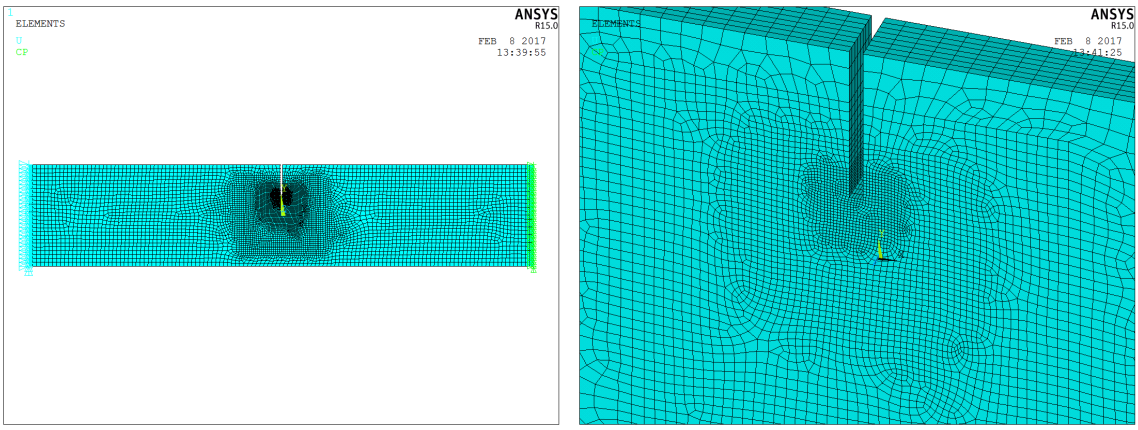

(a) 2D(7175 elements) (b) 3D(57400 elements)

Figure 5.27 : FEA models with mapped mesh grid.

Strain Time History

In the FE analysis, the two load-unload cycles of 8 kip and 12 kip is simulated using ANSYS. In Figure 5.28, the simulated strain results from models 1-4 at g1, g2 and g4 are compared to the experimental strain data obtained by using strain gages. For the No. 1, 2 and 4 models, $E = E_0 = 68.9\,GPa$, $\sigma_y = \sigma_{y0} = 276\,MPa$.

As shown in Figure 5.28, the strain data at g1 from the model 1 with 2D element does not match the experiment data. This is due to the strong assumption of the ANSYS 2D SHELL181 element [80] on plain stress condition. While in the real situation, the stress/strain condition are very complex especially near the notch tip. 3D effect plays a very important role in the stress/strain distribution.

The complex strain conditions near the edge of the notch makes the plain-stress assumption not valid any more. Hence, 2D element is not suitable for this FEA simulation. Once the 3D element is adopted in models 2-4, the strain history curves at g1 are closer to the experimental ones. Since the material at g1 is still within

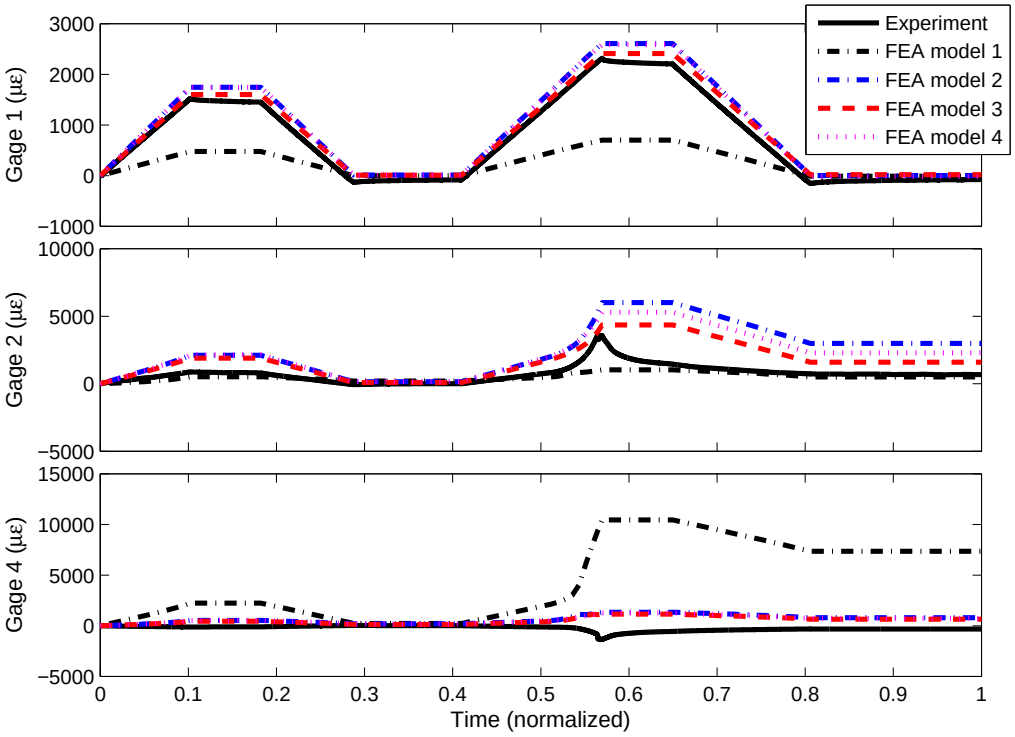

Figure 5.28 : Strain history of experiment and FEA models 1-4.

the linear region, the strain obtained from simulation depends linearly on Young's modulus.

As shown in Figure 5.29, the models 5-8 with increased young's modulus of $E_1 = 75\,GPa$ match the experimental data very well at g1. Because the discontinuity in a straight edge is more abrupt than that in circular edge, the strain condition near the notch is much more complicated to simulate. For example, the Poisson's ratio setting in the FEA is one of the barriers to get a perfect simulation. In ANSYS, once material is judged as "yield", ν is set to 0.5 from original value. While in reality, the change of ν is a $C1$ function of stress condition [59]. Hence, in the pre-notched case study, the strain histories at g2-g4 will not be quantitatively compared between experiment and simulations.

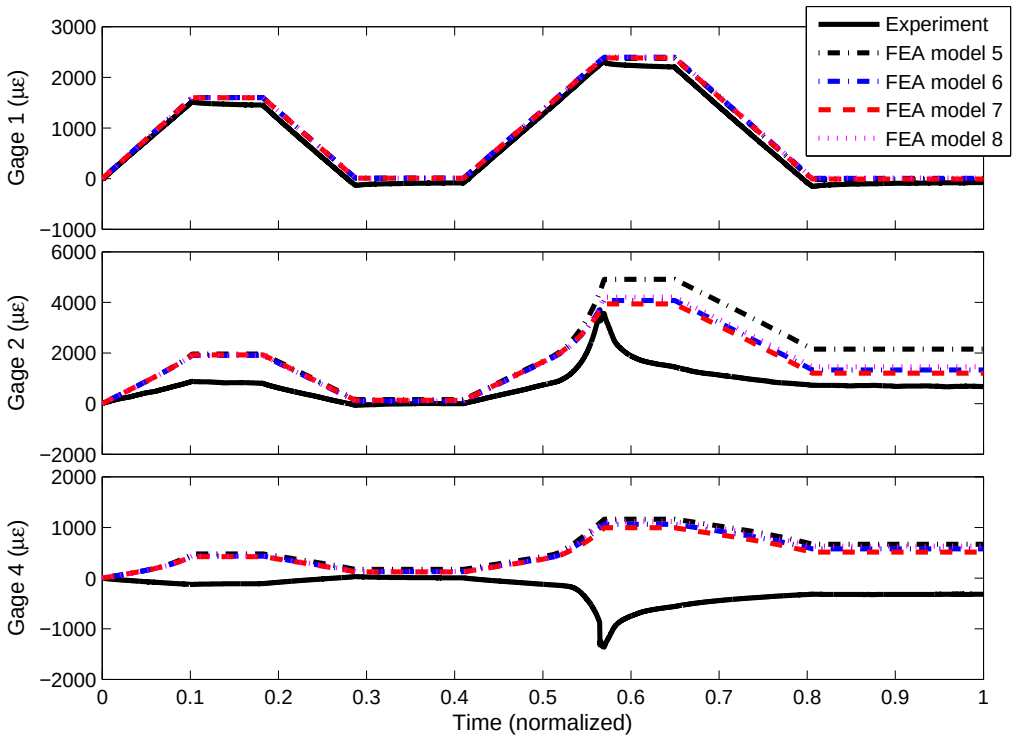

Figure 5.29 : Strain history of experiment and FEA models 5-8.

2D Strain Contour

The residual strain field ϵ_{xx} from model 1-4 are shown in Figure 5.30. Considerable difference can be observed between the 2D model (model 1) and 3D models (model 2-8). The strain distribution pattern form 2D FEA model only has one lobe underneath the notch, while the strain distribution patterns from 3D models look similar with two-lope shape in strain contours as shown in Figure 5.30 and Figure 5.31.

The maximum value of residual strain ϵ_{xx} decrease with the increasing Young's modulus and yielding stress. The detailed shape of the strain contour ϵ_{xx} also change with Ramberg-Osgood parameter n.

Since the FEA in this study is elasto-plastic, the strain patterns/results near

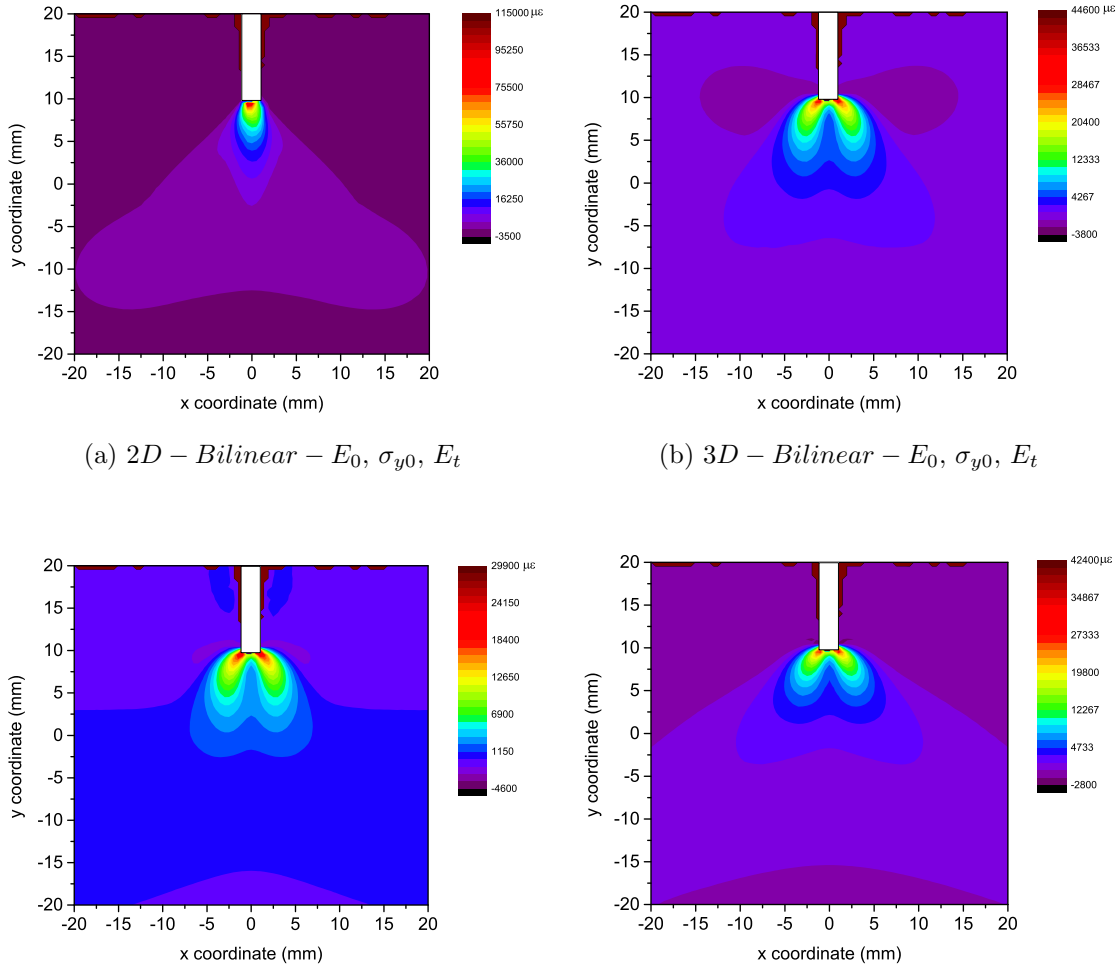

(a) $2D - Bilinear - E_0$, σ_{y0}, E_t

(b) $3D - Bilinear - E_0$, σ_{y0}, E_t

(c) $3D - Bilinear - E_1$, σ_{y1}, E_t

(d) $3D - Multilinear - E_0$, σ_{y0}, $n = 20$

Figure 5.30 : Strain distribution of residual ϵ_{xx} of pre-notched FEA models (a) model 1 (b) model 2 (c) model 3 (d) model 4 after load-unload process.

notches are very complicated and sensitive to many parameters, such as load history, material nonlinearity, Poisson's ratio and so on. The further investigation of the optimization of these parameters is the scope of this study.

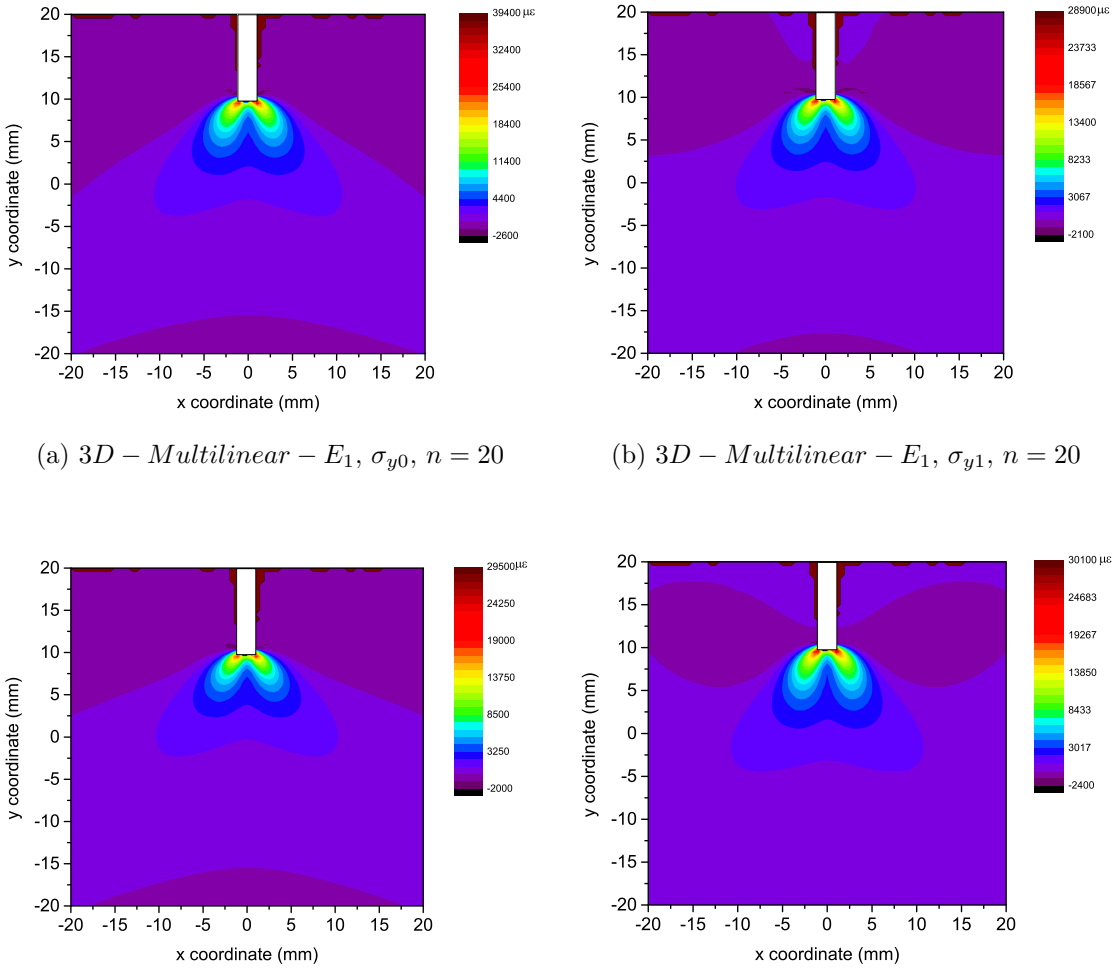

(a) $3D - Multilinear - E_1$, σ_{y0}, $n = 20$

(b) $3D - Multilinear - E_1$, σ_{y1}, $n = 20$

(c) $3D - Multilinear - E_1$, σ_{y1}, $n = 10$

(d) $3D - Multilinear - E_1$, σ_{y1}, $n = 30$

Figure 5.31 : Strain distribution of residual ϵ_{xx} of pre-notched FEA models (a) model 5 (b) model 6 (c) model 7 (d) model 8 after load-unload process.

5.4.4 Discussion

The detailed comparison of residual strain map ϵ_{xx} measured by S^4 and the one simulated by FEA model 3 is shown in Figure 5.32. The scale bars have been tuned to the same (from -4600 $\mu\epsilon$ to 29900 $\mu\epsilon$). Some strain near the edge of the notch is

shown as white color in Figure 5.32 (right), because the strain in the FEA exceeds the maximum limit of the scale bar.

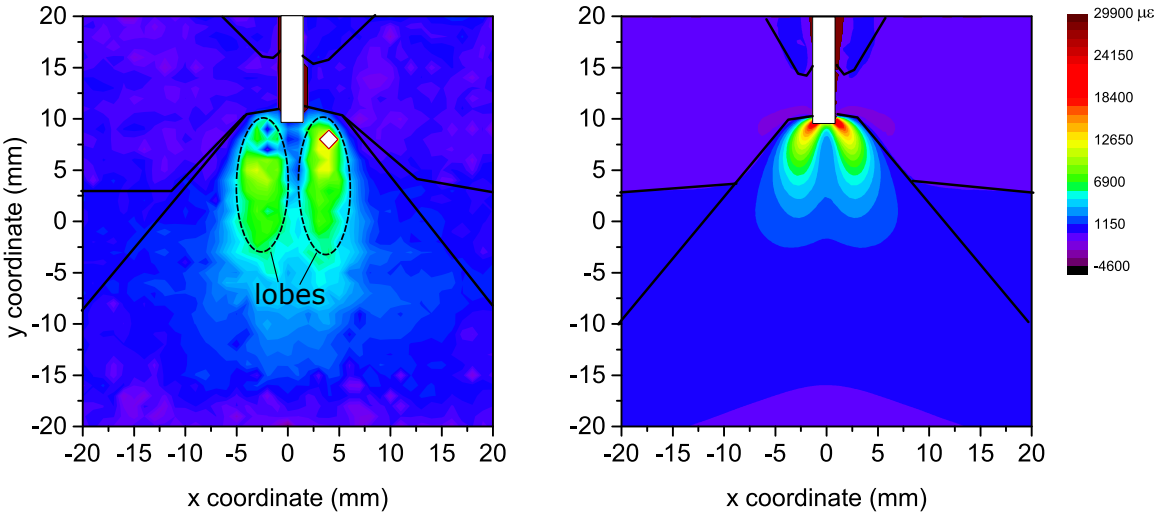

Figure 5.32 : Residual strain map ϵ_{xx} measured by (a) S^4 and (b) FEA model 3 with the same scale bar.

Solid lines are plotted on the two contours to separate the area under tension and compression. Globally, the patterns in the strain distributions of S^4 measurement match well with the FEA simulation. It should be noted that this is a elasto-plastic study, and the accuracy of measurements and FEA simulation depends on many parameters.

5.5 Case Study 3: Strain Analysis on Pre-holed Aluminum Specimen 2

The dimensions of the pre-holed aluminum specimen is the same as case study 1. The newly designed S^4 film is applied on the front side of the bar and 3 channels of strain gages are attached to the back side of the bars as shown in Figure 5.33.

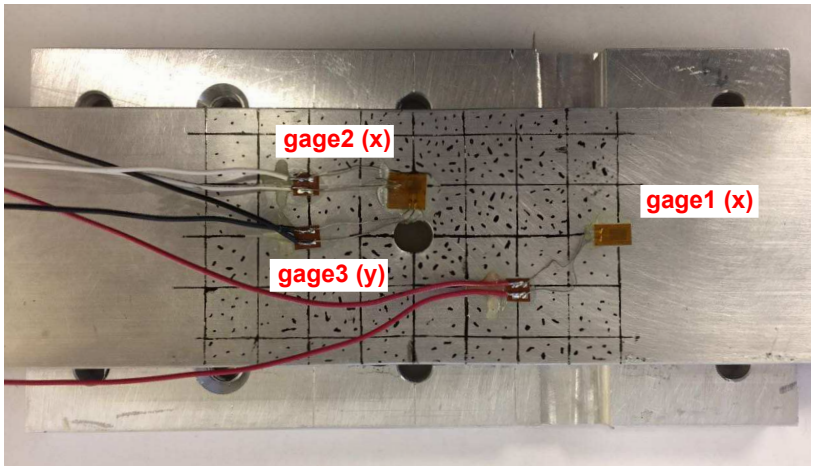

Figure 5.33 : Photo of the back of the pre-holed aluminum specimen 2 with strain gages attached.

If the center of the bar is set as the origin of a cartesian coordinate system with x axis along the length of the bar and y axis along the width, the coordinates of the gages are (-40 mm, 0) for gage 1, (0, 10 mm) for gage 2-3. Strain gages 1-2 are along the x direction, while strain gage 3 is along the y direction. The specimen coated with S^4 film is stretched by MTS hydraulic testing system as shown in Figure 5.6a. An axial load is applied on the specimen along the length or x direction and is increased/decreased gradually at a fixed rate. After each loading or unloading process, the grip is set to hold for several minutes to allow the redistribution of strain on the specimens. The axial force is applied in 1 load-unload cycle with peak value of 19 kip.

As shown in Figure 5.34, during the loading process at 19 kip, the material near strain gage 2-3 begin generating large residual strain. The residual deformation can be seen in Figure 5.35, the circular shape of the hole become elliptical shape in x direction. Because of the large non-linear deformation on the specimen, the polyurethane

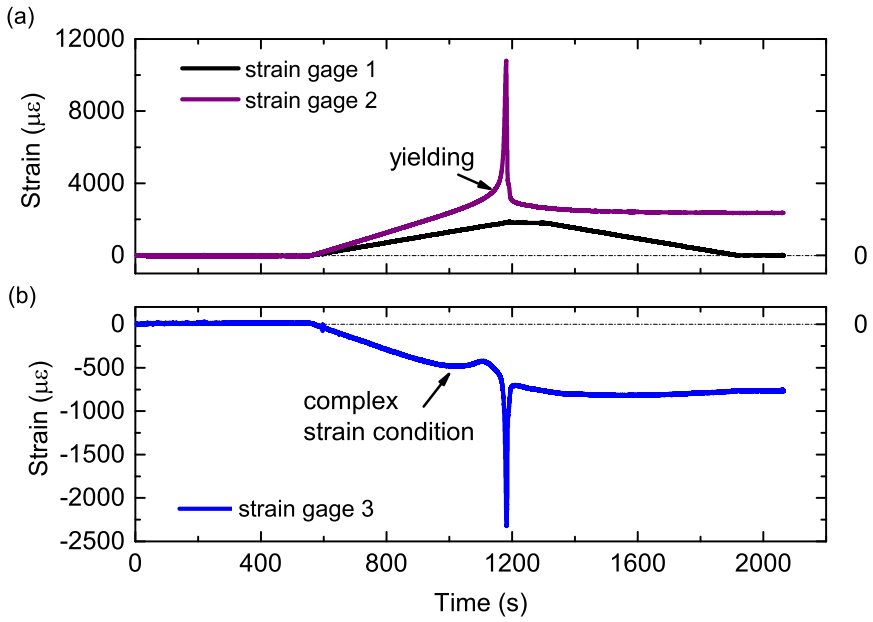

Figure 5.34 : Strain histories measured by the strain gages on pre-holed aluminum specimen 2.

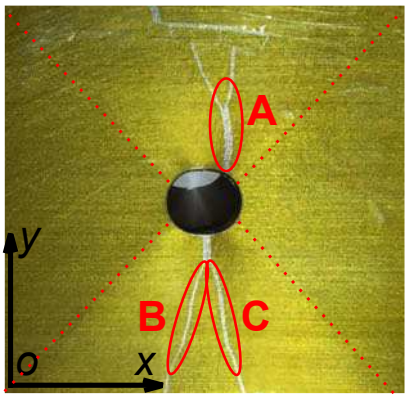

Figure 5.35 : Flipped photo of S^4 film on the front of the aluminum pre-holed specimen 2 after load-unload process.

of the S^4 film coated on top cracks, at the locations A, B, and C but not the PFO-SWCNT layer.

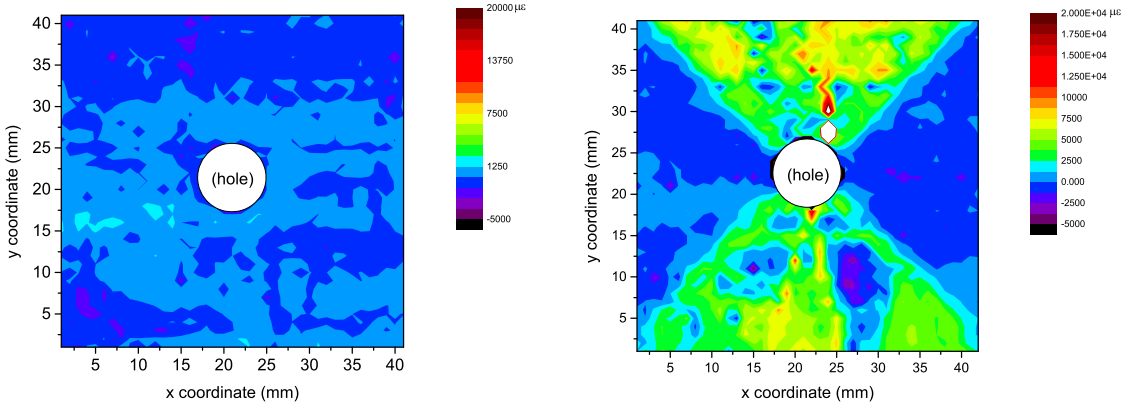

(a) Intact (b) Stretched

Figure 5.36 : Residual strain distribution ϵ_{xx} measured by S^4 sensor on pre-holed aluminum specimen 2.

Figure 5.36b shows the strain reading from S^4 measurement. Although the S^4 cracks due to large deformation on the specimen, the S^4 sensor still is capable of capturing the residual strain pattern. At the crack location A, B and C on film (see Figure 5.35), the strain value of ϵ_{xx} is as large as 20,000 $\mu\epsilon$ in Figure 5.36b.

5.6 Case Study 4: Strain Analysis on Pre-holed Copper Specimen 1

The dimensions of the pre-holed copper specimen (as shown in Figure 4.20 is the same as case study 1 and case study 3. The measure strain data from strain gages are shown in Figure 4.21. The reconstructed strain maps before and after the load-unload process are shown in Chapter 4. There are two cracks on the polyurethane film after the mechanical test, but majority of the PFO-SWCNT film is attached to the copper specimen. The study in this Chapter is focused on the influence of S^4 film damage

to strain measurements.

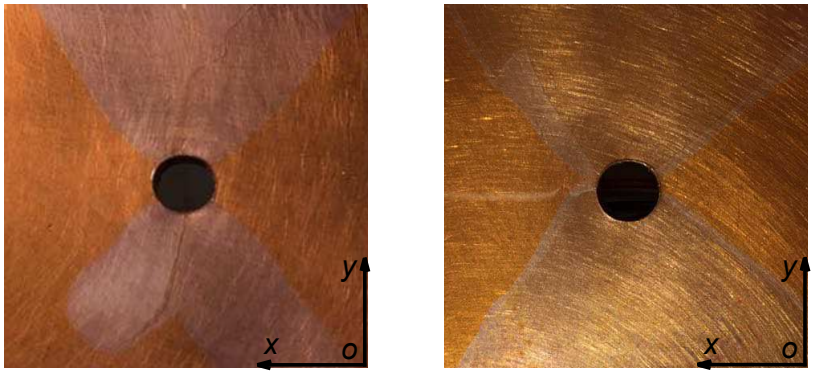

Figure 5.37 : Flipped photo of S^4 film on the front of the pre-holed copper specimen 1 after load-unload process.

Figure 5.37 shows the photos of the copper specimen after detaching the PU film and after peeling off the PU film using a pair of thin tweezers. Figure 5.38a shows the residual strain distribution ϵ_{xx} after the top PU film is detached. While Figure 5.38b shows the residual strain distribution ϵ_{xx} after the top PU film is peeled off at the area of interest.

By comparing Figure 5.38a and Figure 5.38b, we can find that the damage on the S^4 is mainly on the top layer of PU and the sensing layer of PFO-SWCNTs is not affected even the detached polymer film is peeled completed.

5.7 Case Study 5: Strain Analysis on Pre-holed Copper Specimen 2

The dimensions of the pre-holed copper specimen 2 is the same as case study 1, 3 and 4. The newly designed S^4 film is applied on the front side of the bar and 3 channels of strain gages are attached to the back side of the bars as shown in Figure 5.39.

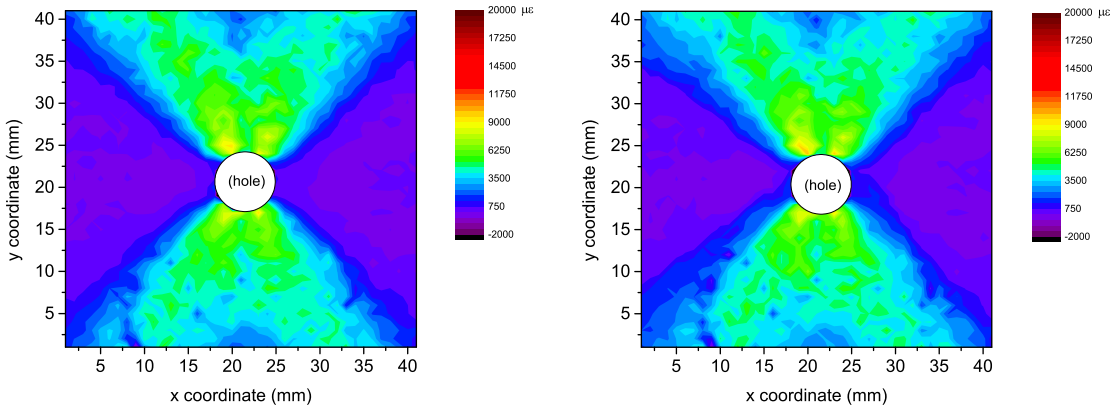

(a) Detached (b) Peeled

Figure 5.38 : Film detached and peeled ϵ_{xx} measured by S^4 sensor.

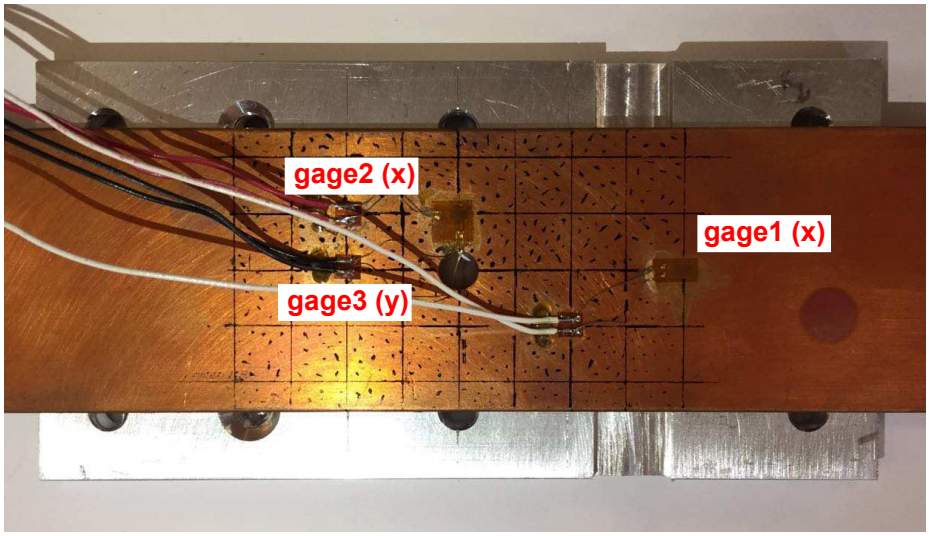

Figure 5.39 : Photo of S^4 film on the back of the pre-holed copper specimen 2.

The specimen coated with S^4 film is stretched by MTS hydraulic testing system. An axial load is applied on the specimen along the length (x direction) and is increased/decreased gradually at a fixed rate. After each loading or unloading process, the grip is set to hold for several minutes to allow the redistribution of strain on the

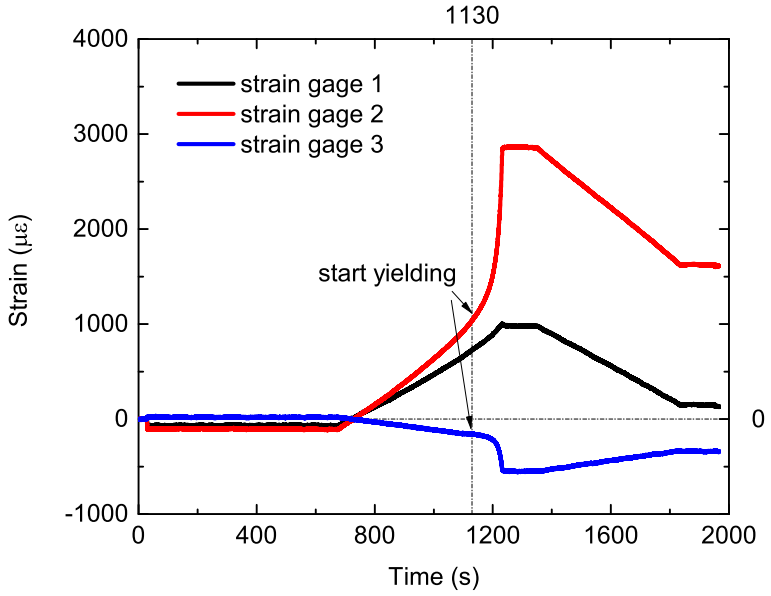

Figure 5.40 : Time history of measured strain by strain gages under load/unload cycles of 15.2 kip.

specimens. The axial force is applied in 1 load-unload cycle with peak values of 15.2 kip. As shown in Figure 5.40, severe nonlinear deformation occurs at position of the strain rosette.

Before and after the mechanical test, 2D S^4 strain in a square area of 30 mm by 30 mm are shown in Figure 5.41a and Figure 5.41b.

5.8 Case Study 6: Strain Analysis on Pre-notched Copper Specimen 1

The dimensions of the pre-notched copper bar are the same as those in case study 2. The newly designed S^4 film is applied on the front side of the bar. The specimen coated with S^4 film is stretched by MTS hydraulic testing system as shown in

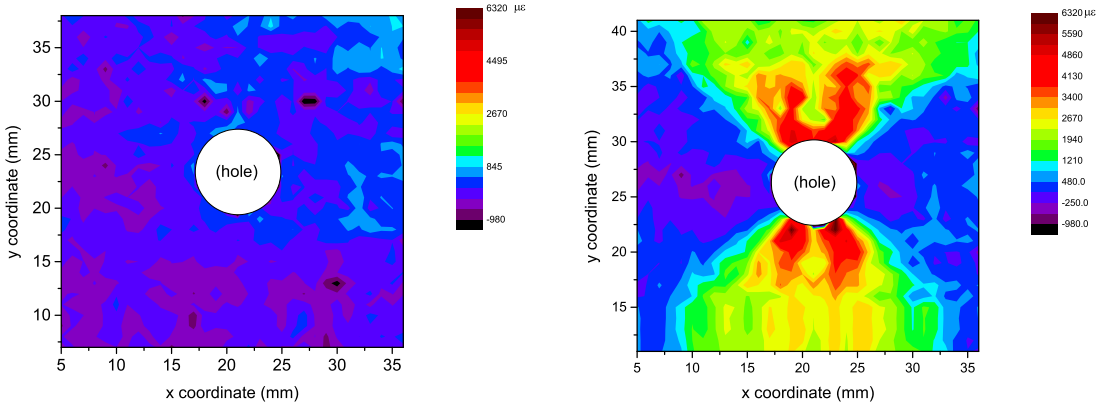

(a) Intact (b) Stretched

Figure 5.41 : Residual strain distribution ϵ_{xx} measured by S^4 sensor on pre-holed copper specimen 2.

Figure 5.21b. An axial load is applied on the specimen along its length and is increased/decreased gradually at a fixed rate. After each loading or unloading process, the grip is set to hold for several minutes to allow the strain to redistribute on the specimen. The axial force is applied in 1 load-unload cycle with peak values of 9.5 kip.

After the mechanical test, two small cracks on the top layer of PU form near the corners of the rectangular notch. However, the cracks on PU layer do not affect the strain reading using the bottom sensing layer of PFO-SWCNTs.

Before and after the mechanical test, 2D S^4 strain scans are performed within a square area of 40 mm by 40 mm near the crack with the polarization of laser excitation along x direction. The mapped strain contour ϵ_{xx} before the mechanical test is shown in Figure 5.43a. The residual strain distribution ϵ_{xx} measured by S^4 sensor on pre-notched copper specimen after load-unload cycle 9.5 kip is shown in

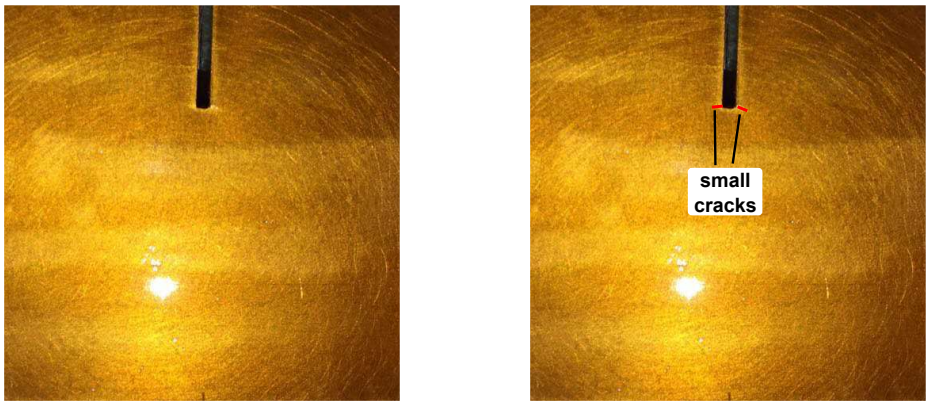

Figure 5.42 : Photo of S^4 film on the front of the pre-notched copper specimen 1 after load-unload process.

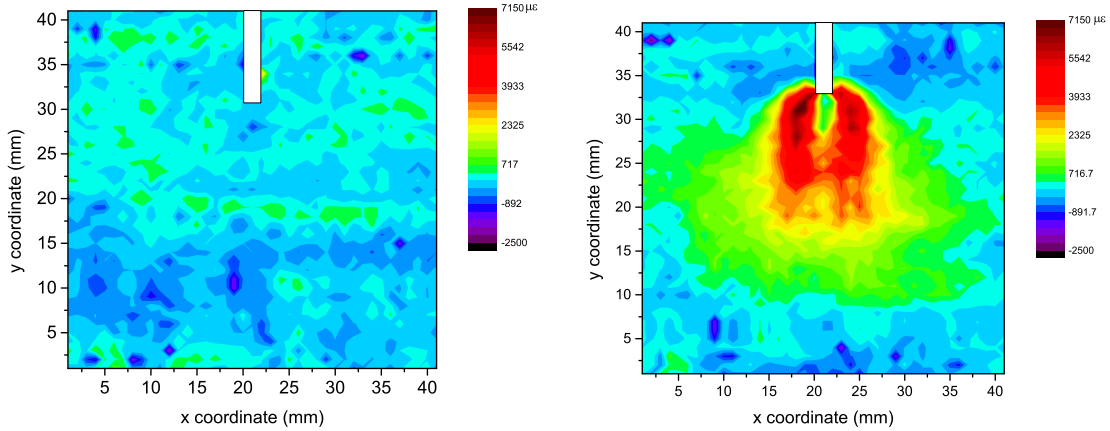

(a) Intact (b) Stretched

Figure 5.43 : Residual strain distribution ϵ_{xx} measured by S^4 sensor on pre-notched copper specimen 1.

Figure 5.43b. We can observe interesting patterns in the strain contours caused by the notch. The result is similar to the case study 2.

5.9 Concluding Remarks

We have demonstrated the first use of a recently developed non-contact, full-field strain measurement technology (S^4) to obtain strain maps near structural discontinuities, such as holes and notches. The S^4 technology uses single-walled carbon nanotube strain sensors embedded in a very thin ($< 0.5\ \mu m$) polymer film with an overcoat of protective polyurethane. Stain in the underlying structure is transmitted to the embedded nanotubes, causing systematic wavelength shifts in their emission spectra. These shifts are quickly measured at arbitrary locations using a portable optical read-out unit that locally excites nanotubes with a laser while capturing the spectrum of the resulting short-wave infrared emission. Spectra from the set of probed points are analyzed to deduce stain and the results are compiled into a 2D strain map with sub-millimeter spatial resolution.

Case studies have been performed on two modified aluminum bars, one with a drilled central hole and the other with a notch, subjected to axial load-unload plastic cycles. We measured ϵ_{xx} strain distributions by comparing S^4 strain maps acquired before and after the loading processes. We observe distinct patterns in the strain contours near the structural discontinuities: four lobes around the hole and two lobes at the notch tip. Clear boundaries between regions of tensile and compressive strain are also seen in the strain maps.

To simulate these findings, we built FEA models using different material parameters and model types. Because nonlinear simulation of large deformations is challenging to perform and depends on many parameters, we used data from foil strain gages attached to the back side of the specimens to guide the selection of suitable models. Our results clearly show that 3D models are needed to simulate the experimental data. With proper adjustment of material parameters in 3D finite element

simulations, we find good agreement with the experimental data from discrete foil strain gages and from S^4 strain maps. We also observe that residual strains can be optically read from S^4 films more than six months after a loading event, indicating the stability of the strain information encoded by the embedded nanotubes.

This study demonstrates the potential for future applications of the S^4 approach for measuring fatigue strain developed by cyclic loads near structural discontinuities. The authors are also optimistic that the S^4 method can become a practical industrial technology for advanced full-field, non-contact strain sensing in a range of important applications, including structural health monitoring, non-destructive evaluation, and experimental mechanics.

Chapter 6

Conclusion

6.1 Concluding Remarks

The main focus of this thesis is to present the design, characterization, development and application of non-contact strain-sensing smart skin(S^4) film sensor for structural health monitoring. Unlike traditional strain gage method using electric wires to transmit electric signal from the sensors, this novel method obtains the change in fluorescence emission wirelessly from the SWCNTs. In this method, well dispersed SWCNTs are embedded within a thin PFO polymeric film. Strain transferred from substrate to the film will change the fluorescence properties of the embedded SWCNTs. A spectrometer is used to analyze the change in the spectrum so that strain can be inferred by using the spectral shifts.

In Chapter 1, Structural Health Monitoring and existing strain sensing based damage identification techniques have been introduced and the motivations of inventing a non-contact strain sensing technique have been described.

Chapter 2 and Chapter 3 have described the progress toward the practical implementation of a novel non-contact optical strain measurement method that uses carbon nanotubes in polymeric films as nano-scale sensors. Strain can be measured anywhere on the surface by irradiating that point with an interrogating laser beam and collecting and analyzing the resulting nanotube fluorescence spectrum. The strain axis can also be found by rotating the polarization plane of the laser beam to selectively inter-

rogate SWCNTs oriented in different directions. Our first-generation smart skin composite ("S^4") is prepared by dispersing raw SWCNTs into commercial polyurethane varnish. Promising results obtained with this material led to the development of a second-generation composite in which the SWCNTs are pre-processed by structural selection and purification. Generation-II S^4 films display strong, well structured fluorescence spectra that allow improved optical strain determinations. Test results show promising repeatability for the S^4 method.

In Chapter 4, a new protocol for S^4 film design and fabrication, has been proposed to achieve a better strain sensing performance. A layer-by-layer "Sandwich" structure for Generation-III S^4 films consists of base coat (usually a polymeric coating in aerospace industry to prevent corrosion), sensing coat (PFO-SWCNTs) and top protective coat (A+B polyurethane). A special heat treatment on the sensing coat (PFO-SWCNTs) should be performed before applying the top protective coat. By far, mechanical tests of the Generation-III S^4 films show good performance in strain sensing.

In Chapter 5, the application of S^4 films in mapping the residual strain field around structural singularities has been performed on pre-holed and pre-cracked metallic specimens. Both analytical studies using LEFM and numerical studies using FEM have been used to validate the experimental results. The chapter also demonstrates the possibilities of S^4 technologies in further investigation of the damage identification and structural health monitoring.

6.2 Unique Contribution

This thesis has developed a novel non-contact strain-sensing smart skin (S^4) film sensor for the application in structural health monitoring. The research involves

nanocomposites design, thin film fabrication, materials characterizations and modelling, strain sensing using short-wave infrared analysis and experimental validation. The unique contributions of this thesis is shown as follows.

(i) Build the numerical model of the SWCNTs randomized system within S^4 to understand the schematics of smart sensing theory by using the fluorescence features from embedded SWCNTs, and to simulate the spectrum behavior due to applied strain.

(ii) Fabricate the prototype (Generation-I) S^4 film sensor and validate it by applying it on PMMA bar which is subjected to four-point bending test.

(iii) Investigate fabrication process in characterizing S^4 film by using different material (polymers, SWCNTs, organic solvent) , different treatment methods on carbon-composite suspension and different film application methods.

(iv) Develop the Generation-II S^4 film with the adoption the PFO . The SWCNTs are pre-processed by structural selection and purification using PFO. Generation-II S^4 films display strong, well structured fluorescence spectra that allow improved optical strain determinations.

(v) Propose a new protocol for S^4 film design and fabrication to achieve a better strain sensing performance. A layer-by-layer "Sandwich" structure for Generation-III S^4 films consists of base coat (usually a polymeric coating in aerospace industry to prevent corrosion), sensing coat (PFO-SWCNTs) and top protective coat (A+B polyurethane). A special heat treatment on the sensing coat (PFO-SWCNTs) should be performed before applying the top protective coat. Mechanical tests of the Generation-III S^4 films shows a good performance in

2D strain sensing.

(vi) Successfully apply S^4 in sensing 2D residual strain on structures near structural discontinuities. The application of S^4 films in mapping the residual strain field on pre-holed and pre-cracked metallic specimens. The experimental results promise a wider application of S^4 on damage identification and structural health monitoring.

6.3 Future Work

In the future, further investigation and research will be carried out in the following aspects:

(i) The efficiency of 2D strain sensing capacity of Generation-III S^4 film sensor will be validated further by using cyclic mechanical tests on specimens.

(ii) Functionalization groups, such as -COOH, can be introduced to the SWCNTs to increase the sensitivity of the sensor without quenching the fluorescence emission.

(iii) The effect of environmental parameters (change), including temperature, humidity and UV exposure will be investigate to ensure the proper function of the S^4 film sensors in an outdoor condition prior to practical application.

(iv) The fabrication process could be further investigated to guarantee the film application in scalable areas with uniform properties (SWCNTs concentration, polymer concentration, SWCNTs orientations etc.)

Bibliography

[1] T. K. Leeuw, D. a. Tsyboulski, P. N. Nikolaev, S. M. Bachilo, S. Arepalli, and R. B. Weisman, "Strain measurements on individual single-walled carbon nanotubes in a polymer host: structure-dependent spectral shifts and load transfer.," *Nano letters*, vol. 8, pp. 826–831, mar 2008.

[2] Wikipedia, "Polyurethane — wikipedia, the free encyclopedia," 2017. [Online; accessed 31-January-2017].

[3] *Aluminum 6061-T6*, Accessed: 2017-02-02. `http://www.matweb.com/search/datasheet_print.aspx?matguid=1b8c06d0ca7c456694c7777d9e10be5b`.

[4] J. P. Lynch and K. J. Loh, "A summary review of wireless sensors and sensor networks for structural health monitoring," *Shock and Vibration Digest*, vol. 38, no. 2, pp. 91–130, 2006.

[5] S. W. S. Doebling, C. R. C. Farrar, M. B. M. Prime, and D. W. D. Shevitz, "Damage identification and health monitoring of structural and mechanical systems from changes in their vibration characteristics: a literature review," tech. rep., 1996.

[6] H. Sohn, C. R. Farrar, F. M. Hemez, D. D. Shunk, D. W. Stinemates, B. R. Nadler, and J. J. Czarnecki, *A review of structural health monitoring literature: 1996-2001.* Los Alamos National Laboratory Los Alamos, NM, 2004.

[7] K. Diamanti and C. Soutis, "Structural health monitoring techniques for aircraft composite structures," *Progress in Aerospace Sciences*, vol. 46, no. 8, pp. 342–352, 2010.

[8] K. J. Loh, J. Kim, J. P. Lynch, N. W. S. Kam, and N. A. Kotov, "Multifunctional layer-by-layer carbon nanotubepolyelectrolyte thin films for strain and corrosion sensing," *Smart Materials and Structures*, vol. 16, no. 2, pp. 429–438, 2007.

[9] W. Obitayo and T. Liu, "A Review: Carbon Nanotube-Based Piezoresistive Strain Sensors," *Journal of Sensors*, vol. 2012, pp. 1–15, 2012.

[10] K. Hill and G. Meltz, "Fiber Bragg grating technology fundamentals and overview," *Journal of lightwave technology*, vol. 15, no. 8, pp. 1263–1276, 1997.

[11] M. Benedetti, V. Fontanari, and D. Zonta, "Structural health monitoring of wind towers: remote damage detection using strain sensors," *Smart Materials and Structures*, vol. 20, no. 5, p. 055009, 2011.

[12] S. Peng and K. Cho, "Chemical control of nanotube electronics," *Nanotechnology*, vol. 11, no. 2, p. 57, 2000.

[13] P. Dharap, Z. Li, S. Nagarajaiah, and E. V. Barrera, "Nanotube film based on single-wall carbon nanotubes for strain sensing," *Nanotechnology*, vol. 15, pp. 379–382, mar 2004.

[14] Y. Yong, "A novel piezoelectric strain sensor for simultaneous damping and tracking control of a high-speed nanopositioner," *IEEE/ASME Transactions*, vol. 18, no. 3, pp. 1113–1121, 2013.

[15] D. Myers, *MEMS Resonant Strain Sensor Integration.* PhD thesis, University of California, Berkeley, 2010.

[16] D. Ryu and K. J. Loh, "Multi-modal sensing using photoactive thin films," *Smart Materials and Structures*, vol. 23, no. 8, p. 085011, 2014.

[17] B. Pan, K. Qian, H. Xie, and A. Asundi, "Two-dimensional digital image correlation for in-plane displacement and strain measurement: a review," *Measurement Science and Technology*, vol. 20, p. 062001, jun 2009.

[18] H. Goldrein, S. Palmer, and J. Huntley, "Automated fine grid technique for measurement of large-strain deformation maps," *Optics and Lasers in Engineering*, vol. 23, no. 195, pp. 305–318, 1995.

[19] B. Pan, "Full-field strain measurement using a two-dimensional Savitzky-Golay digital differentiator in digital image correlation," *Optical Engineering*, vol. 46, p. 033601, mar 2007.

[20] S. Hamada, T. Fujisawa, M. Koyama, N. Koga, N. Nakada, T. Tsuchiyama, M. Ueda, and H. Noguchi, "Strain mapping with high spatial resolution across a wide observation range by digital image correlation on plastic replicas," *Materials Characterization*, vol. 98, pp. 140–146, dec 2014.

[21] A. Germaneau, P. Doumalin, and J.-C. Dupré, "Comparison between X-ray micro-computed tomography and optical scanning tomography for full 3D strain measurement by digital volume correlation," *NDT & E International*, vol. 41, pp. 407–415, sep 2008.

[22] A. Ajovalasit, G. Petrucci, and M. Scafidi, "RGB photoelasticity: review and improvements," *Strain*, vol. 46, no. 2, pp. 137–147, 2010.

[23] Q. Zhao, M. D. Frogley, and H. Wagner, "Direction-sensitive strain-mapping with carbon nanotube sensors," *Composites Science and Technology*, vol. 62, pp. 147–150, jan 2002.

[24] L.-J. Li, R. J. Nicholas, R. S. Deacon, and P. a. Shields, "Chirality Assignment of Single-Walled Carbon Nanotubes with Strain," *Physical Review Letters*, vol. 93, no. October, pp. 6–9, 2004.

[25] M. Mu, S. Osswald, Y. Gogotsi, and K. I. Winey, "An in situ Raman spectroscopy study of stress transfer between carbon nanotubes and polymer.," *Nanotechnology*, vol. 20, p. 335703, aug 2009.

[26] A. de la Vega, I. Kinloch, R. Young, W. Bauhofer, and K. Schulte, "Simultaneous global and local strain sensing in SWCNTepoxy composites by Raman and impedance spectroscopy," *Composites Science and Technology*, vol. 71, pp. 160–166, jan 2011.

[27] Z. Li, P. Dharap, S. Nagarajaiah, E. Barrera, and J. Kim, "Carbon Nanotube Film Sensors," *Advanced Materials*, vol. 16, pp. 640–643, apr 2004.

[28] A. P. A. Raju, A. Lewis, B. Derby, R. J. Young, I. a. Kinloch, R. Zan, and K. S. Novoselov, "Wide-Area Strain Sensors based upon Graphene-Polymer Composite Coatings Probed by Raman Spectroscopy," *Advanced Functional Materials*, vol. 24, pp. 2865–2874, may 2014.

[29] S. Reich, C. Thomsen, and J. Maultzsch, *Carbon nanotubes: basic concepts and physical properties*. John Wiley & Sons, 2008.

[30] M. J. O'Connell, S. M. Bachilo, C. B. Huffman, V. C. Moore, M. S. Strano, E. H. Haroz, K. L. Rialon, P. J. Boul, W. H. Noon, C. Kittrell, J. Ma, R. H. Hauge,

R. B. Weisman, and R. E. Smalley, "Band gap fluorescence from individual single-walled carbon nanotubes.," *Science*, vol. 297, no. 5581, pp. 593–596, 2002.

[31] R. Weisman and S. Bachilo, "Dependence of optical transition energies on structure for single-walled carbon nanotubes in aqueous suspension: an empirical Kataura plot," *Nano Letters*, vol. 3, no. 9, pp. 1235–1238, 2003.

[32] L. Yang and J. Han, "Electronic structure of deformed carbon nanotubes," *Physical Review Letters*, vol. 85, no. 1, pp. 154–157, 2000.

[33] E. D. Minot, Y. Yaish, V. Sazonova, J.-Y. Park, M. Brink, and P. L. McEuen, "Tuning carbon nanotube band gaps with strain.," *Physical review letters*, vol. 90, no. April, p. 156401, 2003.

[34] H. Maki, T. Sato, and K. Ishibashi, "Direct observation of the deformation and the band gap change from an individual single-walled carbon nanotube under uniaxial strain," *Nano Letters*, vol. 7, pp. 890–895, 2007.

[35] M. Huang, Y. Wu, B. Chandra, H. Yan, Y. Shan, T. F. Heinz, and J. Hone, "Direct measurement of strain-induced changes in the band structure of carbon nanotubes," *Physical Review Letters*, vol. 100, no. April, pp. 1–4, 2008.

[36] P. K. Valavala, D. Banyai, M. Seel, and R. Pati, "Self-consistent calculations of strain-induced band gap changes in semiconducting (n,0) carbon nanotubes," *Physical Review B - Condensed Matter and Materials Physics*, vol. 78, pp. 1–6, 2008.

[37] S. M. Vemuru, R. Wahi, S. Nagarajaiah, and P. M. Ajayan, "Strain sensing using a multiwalled carbon nanotube film," *The Journal of Strain Analysis for Engineering Design*, vol. 44, pp. 555–562, 2009.

[38] R. K. Srivastava, V. S. M. Vemuru, Y. Zeng, R. Vajtai, S. Nagarajaiah, P. M. Ajayan, and A. Srivastava, "The strain sensing and thermal-mechanical behavior of flexible multi-walled carbon nanotube/polystyrene composite films," *Carbon*, vol. 49, no. 12, pp. 3928–3936, 2011.

[39] P. A. Withey, V. S. M. Vemuru, S. M. Bachilo, S. Nagarajaiah, and R. B. Weisman, "Strain paint: noncontact strain measurement using single-walled carbon nanotube composite coatings," *Nano letters*, vol. 12, pp. 3497–3500, jul 2012.

[40] P. Sun, J.-H. Kim, S. M. Bachilo, R. B. Weisman, and S. Nagarajaiah, ""Smart Skin" optical strain sensor using single wall carbon nanotubes," in *SPIE Smart Structures and Materials+ Nondestructive Evaluation and Health Monitoring*, vol. 9061, p. 906120, 2014.

[41] S. M. Bachilo, L. Balzano, J. E. Herrera, F. Pompeo, D. E. Resasco, and R. B. Weisman, "Narrow (n , m)-Distribution of Single-Walled Carbon Nanotubes Grown Using a Solid Supported Catalyst," *Journal of the American Chemical Society*, vol. 125, no. 37, pp. 11186–11187, 2003.

[42] E. Sharmin and F. Zafar, "Polyurethane : An Introduction," in *Polyurethane*, pp. 3–16, 2012.

[43] A. Nish, J.-y. Hwang, J. Doig, and R. J. Nicholas, "Highly selective dispersion of single- walled carbon nanotubes using aromatic polymers," *Nature nanotechnology*, vol. 2, no. October, pp. 640–646, 2007.

[44] J. K. Streit, S. M. Bachilo, S. Ghosh, C.-w. Lin, and R. B. Weisman, "Directly Measured Optical Absorption Cross Sections for Structure-Selected Single-Walled Carbon Nanotubes," *Nano letters*, vol. 14, no. 3, pp. 1530–1536, 2014.

[45] C. B. Walsh and E. I. Franses, "Ultrathin PMMA films spin-coated from toluene solutions," *Thin Solid Films*, vol. 429, no. 1-2, pp. 71–76, 2003.

[46] P. Sun, S. M. Bachilo, R. B. Weisman, and S. Nagarajaiah, "Carbon nanotubes as non-contact optical strain sensors in smart skins," *The Journal of Strain Analysis for Engineering Design*, vol. 50, no. 7, pp. 505–512, 2015.

[47] P. Sun, S. M. Bachilo, S. Nagarajaiah, and R. B. Weisman, "Toward Practical Non-Contact Optical Strain Sensing Using Single-Walled Carbon Nanotubes," *ECS Journal of Solid State Science and Technology*, vol. 5, no. 8, pp. M3012–M3017, 2016.

[48] T. Yasuda, K. Fujita, T. Tsutsui, Y. Geng, S. W. Culligan, S. H. Chen, R. V. August, V. Re, M. Recei, and V. October, "Carrier Transport Properties of Monodisperse Glassy-Nematic Oligofluorenes in Organic Field-Effect Transistors," *Chemistry of Materials*, vol. 17, no. 2, pp. 264–268, 2005.

[49] E. Z. Stowell, "Stress and strain concentration at a circular hole in an infinite plate," 1950.

[50] M. Mohammadi, J. R. Dryden, and L. Jiang, "Stress concentration around a hole in a radially inhomogeneous plate," *International Journal of Solids and Structures*, vol. 48, no. 3-4, pp. 483–491, 2011.

[51] P. Lazzarin, M. Zappalorto, and F. Berto, "Recent developments in multiparametric three-dimensional stress field representation in plates weakened by cracks and notches," *Frattura ed Integrita Strutturale*, vol. 7, no. 25, pp. 61–68, 2013.

[52] M. Zappalorto and P. Lazzarin, "Three-dimensional elastic stress fields ahead of notches in thick plates under various loading conditions," *Engineering Fracture Mechanics*, vol. 108, pp. 75–88, 2013.

[53] P. Lazzarin and M. Zappalorto, "A three-dimensional stress field solution for pointed and sharply radiused V-notches in plates of finite thickness," *Fatigue and Fracture of Engineering Materials and Structures*, vol. 35, no. 12, pp. 1105–1119, 2012.

[54] D. Radaj, "Stress singularity, notch stress and structural stress at spot-welded joints," *Engineering Fracture Mechanics*, vol. 34, no. 2, pp. 495–506, 1989.

[55] M. Gupta, R. C. Alderliesten, and R. Benedictus, "A review of T-stress and its effects in fracture mechanics," *Engineering Fracture Mechanics*, vol. 134, pp. 218–241, 2015.

[56] R. A. Sousa and F. P. Figueiredo, "The principle of similitude analysed from plastic zones estimates ahead crack tips," *International Journal of Mechanical Sciences*, vol. 89, pp. 403–412, 2014.

[57] Y. Matvienko, "The Effect of the Non-singular T-stress Components on Crack Tip Plastic Zone under Mode I Loading," *Procedia Materials Science*, vol. 3, pp. 141–146, 2014.

[58] M. Hammouda, R. Smith, and K. Miller, "Elastic-plastic fracture mechanics for initiation and propagation of notch fatigue cracks," *Fatigue & Fracture of Engineering Materials & Structures*, vol. 2, no. 2, pp. 139–154, 1979.

[59] M. A. Meyers and K. K. Chawla, *Mechanical behavior of materials*, vol. 2. Cambridge university press Cambridge, 2009.

[60] Y. Chen, "Numerical computation of dynamic stress intensity factors by a Lagrangian finite-difference method (the HEMP code)," *Engineering Fracture Mechanics*, vol. 7, no. 4, pp. 653—-660, 1975.

[61] B. Chouet, "Dynamics of a fluid-driven crack in three dimensions by the finite difference method," *Journal of Geophysical Research*, vol. 91, no. B14, p. 13967, 1986.

[62] A. Portela, M. H. Aliabadi, and D. Rooke, "THE DUAL BOUNDARY ELEMENT METHOD:EFFECTIVE IMPLEMENTATION FOR CRACK PROBLEMS," *International Journal for Numerical Methods in Engineering*, vol. 33, no. December 1990, pp. 1269–1287, 1992.

[63] R. T. Fenner, "The Boundary Integral Equation(Boundary Element) Method In Engineering Stress Analysis," *Journal of Strain Analysis*, vol. 18, no. 4, pp. 199–205, 1983.

[64] N. K. Jain and N. D. Mittal, "Finite element analysis for stress concentration and deflection in isotropic, orthotropic and laminated composite plates with central circular hole under transverse static loading," *Materials Science and Engineering A*, vol. 498, no. 1-2, pp. 115–124, 2008.

[65] Z. Yang, C. B. Kim, C. Cho, and H. G. Beom, "The concentration of stress and strain in finite thickness elastic plate containing a circular hole," *International Journal of Solids and Structures*, vol. 45, no. 3-4, pp. 713–731, 2008.

[66] N. Troyani, C. Gomes, and G. Sterlacci, "Theoretical Stress Concentration Factors for Short Rectangular Plates With Centered Circular Holes," *Journal of Mechanical Design*, vol. 124, no. 1, p. 126, 2002.

[67] Z. Wu, "Optimal hole shape for minimum stress concentration using parameterized geometry models," *Structural and Multidisciplinary Optimization*, vol. 37, no. 6, pp. 625–634, 2009.

[68] S. Meguid, "Finite element analysis of defence hole systems for the reduction of stress concentration in a uniaxially-loaded plate with two coaxial holes," *Engineering fracture mechanics*, vol. 25, no. 4, pp. 403–413, 1986.

[69] P. Lazzarin, M. Zappalorto, and F. Berto, "Three-dimensional stress fields due to notches in plates under linear elastic and elastic-plastic conditions," *Fatigue and Fracture of Engineering Materials and Structures*, vol. 38, no. 2, pp. 140–153, 2015.

[70] R. C. De Oliveira Góes, J. T. P. De Castro, and L. F. Martha, "3D effects around notch and crack tips," *International Journal of Fatigue*, vol. 62, pp. 159–170, 2014.

[71] R. C. O. Góes, J. T. P. Castro, and M. A. Meggiolaro, "3D thickness effects around notch and crack tip stress/strain fields," *Frattura ed Integrita Strutturale*, vol. 9, no. 33, pp. 89–96, 2015.

[72] T. Baxevanis, Y. Chemisky, and D. C. Lagoudas, "Finite element analysis of the plane strain crack-tip mechanical fields in pseudoelastic shape memory alloys," *Smart Materials and Structures*, vol. 21, no. 9, p. 094012, 2012.

[73] M. Sjödahl, "Electronic speckle photography: measurement of in-plane strain fields through the use of defocused laser speckle.," *Applied optics*, vol. 34, no. 25, pp. 5799–5808, 1995.

[74] R. Moutou Pitti, C. Badulescu, and M. Grediac, "Characterization of a cracked specimen with full-field measurements: direct determination of the crack tip and energy release rate calculation," *International Journal of Fracture*, vol. 187, no. 1, pp. 1–13, 2014.

[75] Y. Hos, J. L. F. Freire, and M. Vormwald, "Measurements of strain fields around crack tips under proportional and non-proportional mixed-mode fatigue loading," *International Journal of Fatigue*, vol. 89, pp. 87–98, 2015.

[76] W. Wang, J. E. Mottershead, C. M. Sebastian, and E. a. Patterson, "Shape features and finite element model updating from full-field strain data," *International Journal of Solids and Structures*, vol. 48, pp. 1644–1657, jun 2011.

[77] J. Hutchinson, "Plastic stress and strain fields at a crack tip," *Journal of the Mechanics and Physics of Solids*, vol. 16, no. 5, pp. 337–342, 1968.

[78] C. J. Christopher, M. N. James, E. A. Patterson, and K. F. Tee, "A quantitative evaluation of fatigue crack shielding forces using photoelasticity," *Engineering Fracture Mechanics*, vol. 75, no. 14, pp. 4190–4199, 2008.

[79] P. Sun, S. M. Bachilo, C.-W. Lin, S. Nagarajaiah, and R. B. Weisman, "Full-field non-contact strain sensing using a nano-composite film," *Smart Materials and Structures*, 2017. , submitted.

[80] *Chapter 8: Nonlinear Structural Analysis*, Accessed: 2017-02-02. `http://www.ansys.stuba.sk/html/guide_55/g-str/GSTR8.htm`.

[81] W. Ramberg and W. R. Osgood, "Description of stress-strain curves by three parameters," 1943.

[82] *Aluminium Alloy 6061 - Composition, Properties, Temper and Applications of 6061 Aluminium*, Accessed: 2017-02-02. http://www.azom.com/article.aspx?ArticleID=3328.

[83] T. C. Hufnage, U. K. Vempati, and J. D. Almer, "Crack-tip strain field mapping and the toughness of metallic glasses," *PLoS ONE*, vol. 8, no. 12, 2013.